COO-2250-37
MITNE-226

INTERFACIAL EFFECTS IN FAST REACTORS

by

M. S. Saidi
and
M. J. Driscoll

May 1979

Massachusetts Institute of Technology
Department of Nuclear Engineering
Cambridge, Massachusetts

U.S. Department of Energy
Contract EY-76-S-02-2250

Massachusetts Institute of Technology
Department of Nuclear Engineering
Cambridge, Massachusetts

INTERFACIAL EFFECTS IN FAST REACTORS

by

M. S. Saidi

and

M. J. Driscoll

May 1979

COO-2250-37

MITNE-226

U.S. Department of Energy

Contract EY-76-S-02-2250

COO-2250-37

Distribution

Department of Energy Research and Development
Contract EY-76-S-02-2250
UC-79P LMFBR-Physics

1-3 U.S. Department of Energy
Division of Reactor Development and Technology
Reactor Physics Branch
Washington, D.C. 20545

4-9 Harold N. Miller, Director
Contract Management Office
U.S. Department of Energy
9800 South Cass Avenue
Argonne, Illinois 60439

10 Director, Nuclear Power
Electric Power Research Institute
Post Office Box 10412
Palo Alto, California 94303

11 c/o Ms. G. L. Ehrman
School of Nuclear Engineering
Purdue University
West Lafayette, Indiana 47907

ABSTRACT

The problem of increased resonance capture rates near zone interfaces in fast reactor media has been examined both theoretically and experimentally.

An interface traversing assembly was designed, constructed and employed to measure U-238 capture rates near the blanket-reflector interface in the MIT Blanket Test Facility. Prior MIT experiments on a thorium-uranium interface in a blanket assembly were also reanalyzed. Extremely localized fertile capture rate increases of on the order of 50% were measured immediately at the interfaces relative to extrapolation of asymptotic interior traverses, and relative to state-of-the-art (LIB-IV, SPHINX, ANISN/2DB) calculations which employ infinite-medium self-shileding throughout a given zone.

A method was developed to compute a spatially varying background scattering cross section per absorber nucleus, σ_o, which takes into account both homogeneous and heterogeneous effects on the interface flux transient. This permitted use of the standard self-shielding factor method (Bondarenko f-factors) to generate modified cross sections for thin layers near the interfaces. Calculations of the MIT experiments using this approach yielded good agreement with the measured data.

ACKNOWLEDGEMENTS

The work described in this report has been performed primarily by the principal author, M. Saidi, who has submitted substantially the same report in partial fulfillment of the requirements for the Ph.D. degree at M.I.T..

The help of Professor David D. Lanning, who served as thesis reader, is gratefully acknowledged.

Thanks are offered to Mr. Albert T. Supple and the M.I.T. Reactor Machine Shop and Radiation Protection Office personnel for their assistance on the experimental work.

Computer calculations were performed at the M.I.T. Information Processing Center. Ms. Rachel Morton provided assistance and advice on computational problems.

Typing of this manuscript has been very ably handled by Ms. Cynthia Mitaras.

TABLE OF CONTENTS

LIST OF FIGURES

LIST OF TABLES

CHAPTER 1

INTRODUCTION

1.1 FOREWORD

Many state-of-the-art neutronic computations for fast reactor core and blanket designs are based upon the Bondarenko or self-shielding factor method of cross section generation (B1, K1). This method relies upon the use of self-shielding factors developed from an infinite-medium treatment of resonance absorption (and scattering). As such it is not appropriate for the treatment of cross sections near interfaces between dissimilar media, such as occur between the core and blanket or blanket and reflector. To resolve this problem, use of appropriately weighted space-dependent broad group constants has been recommended for accurate prediction of neutron transport in the blanket region (G1, S1). But even with the use of the space-dependent broad group constants, theoretical prediction of the detailed reaction-rate mappings near large heterogeneities such as core-blanket interfaces and blanket-reflector interfaces is currently not satisfactory. One of the main causes of discrepancy can be attributed to the mismatch in cross section energy structure due to the dissimilitude in compositions near the zone interfaces. Systematic methods for handling the mismatch remain to be worked out: a central goal to which the present research is a contribution. Due to the softer spectrum and the greater dissimilitude in compositions, the problem at the blanket reflector interface is considerably more difficult than that at the core-blanket interface, where the dominant fertile resonant isotope, U-238, is generally present in both regions.

For calculation of global parameters such as the Doppler coefficient and the total core conversion ratio, which are generally insensitive to local perturbations in the spatial capture rate distributions, the more elaborate calculational techniques needed to treat spatial variations in resonant flux near region boundaries have not generally been needed in FBR nuclear design and analyses to date. Thus, proper prediction of the local Pu-239 production rate and net accumulation, the power distribution, and temperatures reached in peripheral subchannels and fuel pins of U-238 blanket assemblies represents a problem in the calculation of spatial resonant reaction rate distributions not fully addressed in the course of FBR nuclear design. At these interfaces, the reflected neutron current from the axial or radial reflectors can cause a significant local increase in the capture rate.

The recent interest in heterogeneous core designs, in which blanket assemblies are interspersed throughout the core, has intensified the interest in resolving this difficulty. Mixed progeny designs, in which thorium internal blankets are used in uranium-plutonium cores are particularly susceptible to interface problems of the type under examination here. Finally, fuel test facilities such as the FTR and PEC reactors, in which a variety of assemblies of dissimilar designs and compositions must co-exist, have a special need for attention to detail in this area (R1). Accordingly, it is the objective of this work to develop and evaluate the means for accounting for interfacial effects in LMFBR calculations.

1.2 PREVIOUS WORK

Limited work has been done on the study of the interfacial effect. The review of some of the literature in this area will help provide a better appreciation of the nature and status of understanding of the interfacial problem.

In work reported by German investigators (K2), the core-blanket and blanket exterior interfaces have been studied. For the case of two adjacent half spaces, assuming the NR approximation, a solution for the neutron flux from the integral Boltzmann-equation for isotropic scattering can be given within a resonance. This solution is used as a weighting function for the effective space dependent group cross sections.

It is found that the space dependent resonance self shielding is only important within two mean free paths on both sides of an interface. Also it is noticed that in the blanket the absorption rate will be higher by several percent than predicted with space independent group cross sections. This means that the plutonium production is underestimated. For power reactors this can cause local changes of the power distribution at the interface of several percent, because more Pu-239 is produced. It is found that the U-238 capture rate distributions using the correct cross section for the core-blanket interface (core side), core-blanket interface (blanket side) and blanket-vacuum interface differ from the uncorrected results by 5.5%, 5.3% and 1.4% respectively.

In work done by another group of German investigators the problem of strong space-dependent neutron spectra appearing at boundaries has been studied at a sodium-iron interface in slab geometry (K3). The spatial neutron spectra from a 14 mev neutron source were measured in the energy

range from 100 ev to 4.5 Mev. The comparison of measured and calculated spectra, both functions of space and energy, showed that the spectrum around the sodium resonance is well described by 208 energy groups. A relationship is developed that is a function of the resonance parameters and the properties of the material concerned, from which it is possible to estimate the depth to which the flux depression at a resonance energy propagates into an adjacent material. The flux depression is approximated by an exponential function with the exponential constant λ a function of resonance width Γ_r, resonance energy E_R and slowing down density $\xi\Sigma_s$, i.e. $\lambda = \frac{\Gamma_r}{2E_R\xi\Sigma_s}$.

In work related to FTR experiments local spatial variations in the U-238 capture rate near the blanket/reflector interface for the resonance energy range are calculated separately using a one-dimensional, hyper fine-group, integral transport capture program (R1). Three regions were employed, representing the homogenized blanket experiment, homogeneous axial or radial reflector; and a UO_2 region with a mean chord length equal to that of the experimental blanket pellets. These detailed calculations for the resonant reaction rate distribution and effective broad group cross sections were made for various locations of the UO_2 region with respect to the experiment/reflector interface, obtaining sets of broad group cross sections averaged over the UO_2 region which represent blanket pins at various locations within the experimental assembly. These sets of cross sections for the resolved resonance range were then combined with cross sections prepared by the shielding factor method for the remaining energy groups, to create sets of spatially dependent U-238 capture cross sections, each set appropriate to a different location

of the UO_2 pellet with respect to the blanket/reflector interface. The overall result shows a rise of about 40% in the U-238 capture rates near the interface.

The above brief review shows that only one of the self shielding factor components (there are two kinds of self shielding effects which contribute to self-shielding factors: energy or homogeneous self shielding and spatial or heterogeneous self shielding; for more detail consult Refs. H1, D1, S2) is corrected for the interfacial effect and also that the problems have not been solved in a systematic way, so that the results can be easily applied to other cases. Hence, there remains a need for continued study of this phenomenon.

1.3 OUTLINE OF CURRENT WORK

In working out the rationale for the approach to the interface problem it was recognized that sufficient subtleties were involved to make it essential that some experimental base for testing analytic results would be highly desirable. Thus a series of realistic experiments were planned and carried out using the Blanket Test Facility at the MIT research reactor.

The Blanket Test Facility is described briefly in the first section of Chapter 2. In the following sections, the design and construction of an Interface Traversing Subassembly (ITS) are discussed.

The experiments performed on the ITS using U-235, U-238 and Au-197 traversing foils and the experimental results are described in Chapter 3. Chapter 4 summarizes the analysis of the ITS experimental results. The ITS experimental results are compared with other experimental data and state of the art calculations in this chapter and the dominant

parameters that affect the interfacial effect are deduced and discussed.

Derivations of space-dependent homogeneous and heterogeneous self-shielding factors are described in Chapter 5. The generation of corrected space-dependent cross sections and the corresponding ANISN results are included in the following sections. Finally, a summary, conclusions and recommendations for future work are discussed in Chapter 6.

In Appendix A the transient flux near the interface is derived and in Appendix B the Dancoff factor for the case when the neutron slowing down source is non-zero in the fuel region is derived. Other appendices include tabulations of data acquired in the experiments and calculations, and the references.

CHAPTER 2

DESIGN AND CONSTRUCTION OF THE INTERFACE TRANSVERSING SUBASSEMBLY (ITS)

2.1 INTRODUCTION

To permit experimental investigations of typical LMFBR breeding blankets, a facility (the Blanket Test Facility - BTF) was designed and constructed at the MIT Reactor in the Fall of 1969 (Ref. F1). The facility consists of a converter, blanket mockup, and a reflector. The converter assembly, consisting of a 20-cm thick layer of graphite followed by a 17.5-cm thick UO_2 fuel region is used to convert thermal neutrons, provided by the reactor, into fast neutrons to drive the blanket mockup. Operating at 18 watts (55 watts prior to the MITR redesign) the converter generates blanket fluxes at an equivalent LMFBR core power of about 116 watts, with as little as one tenth of the blanket material required for a critical assembly. Calculations and subsequent measurements showed that the converter leakage spectrum was a close approximation to the core leakage spectrum from reference LMFBR designs. The effective height and width of the blanket mockup assembly were correctly chosen (Ref. F1) so that the axial distribution of the neutron flux in the blanket assembly simulated that in the radial blanket of a large LMFBR.

Since the MIT Blanket Test Facility first became operational, a total of six different blanket assemblies have been tested. The first five blanket assemblies have been described in detail by M. Macher (Ref. M1). In the present research, blanket mockup no. 6 was used as the host assembly, as described in Section 2.2. To carry out the planned experiments, design and construction of an Interface Traversing Subassembly (ITS) was

necessary, as covered in Sections 2.3 and 2.4. This chapter concludes with a summary, in Section 2.5.

2.2 THE BLANKET TEST FACILITY AND MOCKUP NO. 6

In performing the experiments on blanket-reflector interfacial effects, Blanket Test Facility (BTF) Mockup No. 6 was used. The BTF is located at the rear of the MITR (MIT Reactor) graphite-lined hohlraum in an irradiation cave approximately 6 ft. by 6 ft. (see Figures 2.1 and 2.2). Access to the cavity is gained by removing two 15 ton magnetite concrete shield doors using the reactor building's overhead crane. The converter plate and simulated blanket assembly are mounted on separate carts which run on rails extending from the front of the irradiation cave out to the containment wall, allowing the carts to be rolled into, or removed from, their operating position. Mounting them on separate carts reduces radiation exposure by permitting work on the blanket to be performed on the reactor floor at a safe distance from the converter.

Blanket Mockup No. 6 is similar to No. 5, except that it consists of three rows of blanket subassemblies rather than one row. The inner reflector zone is again made up of solid carbon steel subassemblies. (The outer reflector is composed of a stack of steel sheets.) This has the advantage that the reflector region adjacent to the blanket has a uniform density. The three row blanket is sufficiently thick to insulate the outer blanket row from converter-blanket interface effects, and thus the assembly is suitable for clean experiments at the blanket-reflector interface. The physical specifications and the atomic number densities of Mockup No. 6 are given in Tables 2.1 and 2.2. These tables were prepared using BTF No. 5 specifications given in

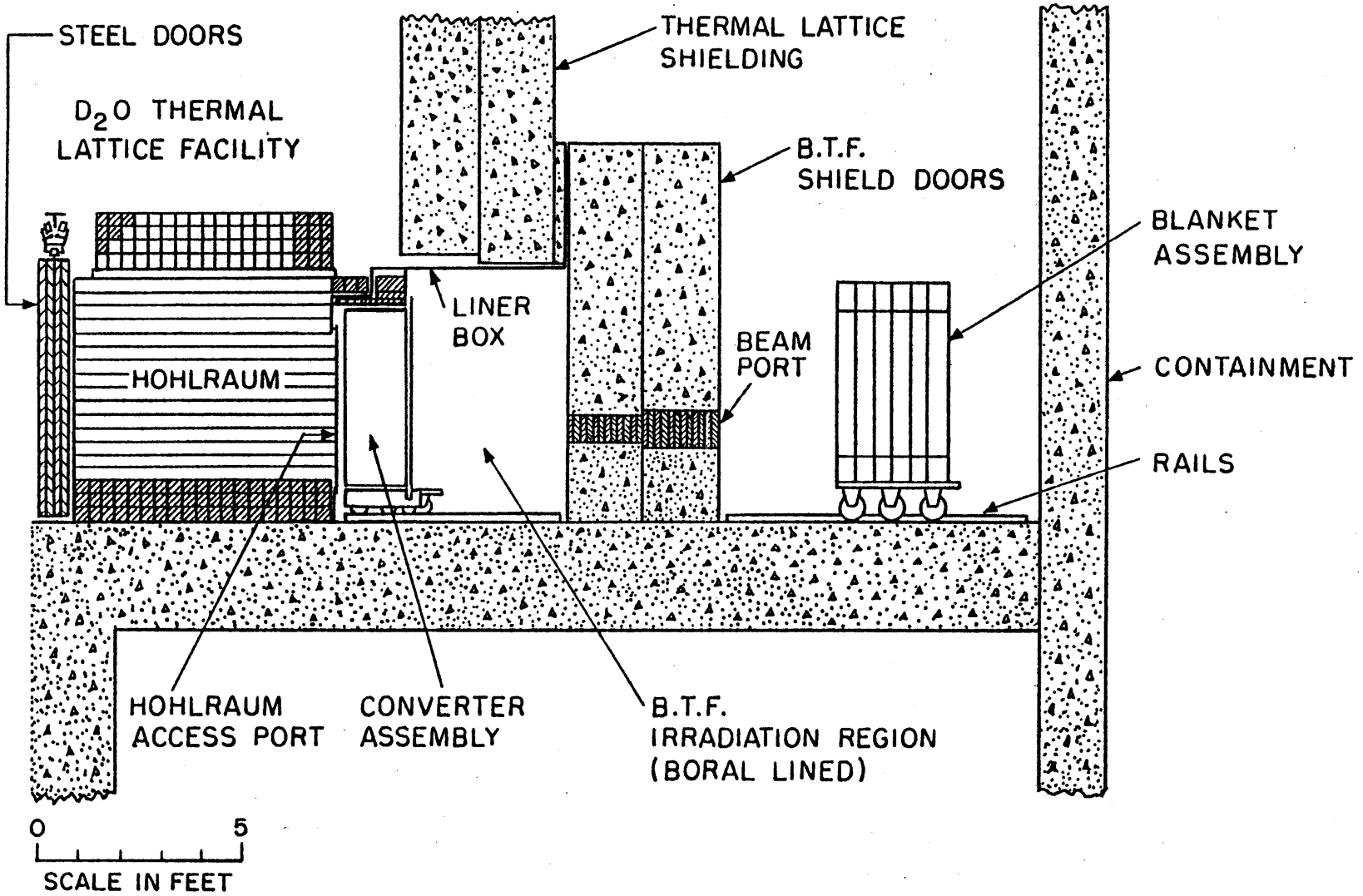

FIG. 2.1 SCHEMATIC CROSS SECTION VIEW OF HOHLRAUM AND BLANKET TEST FACILITY

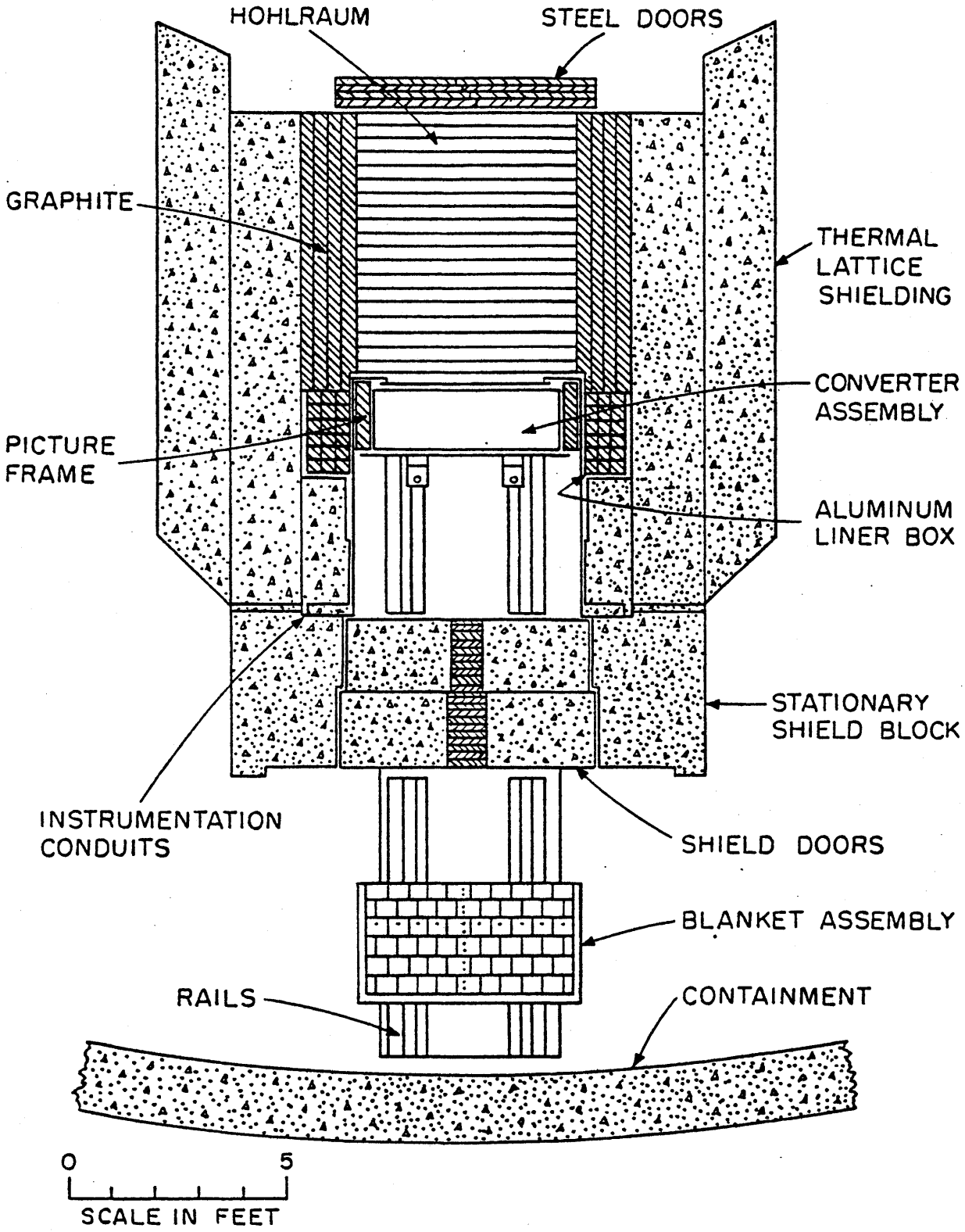

FIG. 2.2 SCHEMATIC PLAN VIEW OF THE HOHLRAUM AND BLANKET TEST FACILITY

TABLE 2.1

Blanket Mockup No. 6 Physical Specifications (Ref. M1)

Region/Thickness	Component	Material	Dimensions	Material Density (g/cm^3)	Homogenized Density (g/cm^3)
Converter, Graphite 5 cm (nominal) 4.924 cm (actual)	Graphite Blocks	Graphite	4.924 cm thick	1.65 (approx.)	1.65
Converter, First Fuel Zone 0.9126 in. (approx.)	Fuel	UO_2 1.99 w/o U-235 (2 rows)	0.430 in. diameter 0.510 in triangular pitch	10.20	6.365
	Cladding	Aluminum Type 1100 99 w/o Al	0.500 in. O.D. 0.032 in. thick	2.71	0.5479
Converter Second Fuel Zone 3.715 in.	Fuel	UO_2 1.099 w/o U-235 (8 rows)	0.430 in. diameter 0.510 in. triangular pitch	10.20	6.254

TABLE 2.1 (continued)

Region/ Thickness	Component	Material	Dimensions	Material Density (g/cm^3)	Homogenized Density (g/cm^3)
Al Backing & Boral Sheet 0.250 in.	Aluminum Sheet	Aluminum 6061-T6	0.125 in. thick	2.71 (approx.)	1.355
	Boral Sheet 0.125 in. thick total	Aluminum Clad	0.020 in. thick	2.71 (approx.)	0.4336
		Boral (no clad) = 65.0 w/o Al & 35.0 w/o B_4C	0.085 in. thick	2.53	0.8602
Blanket Midplane area = (5.92 in. x 5.92 in.) Thickness = 17.76 in.	Subassembly Box (25 boxes)	Low-carbon steel, 0.15 w/o C	5-13/16 in. by 5-13/16 in. outside diameter 3/32 in. wall thickness 60 in. long	7.86 (approx.)	0.7705
	Foil Traversing Tube (26 tubes)	Low-carbon steel, 0.15 w/o C	7/16 in. O.D., 0.028 in. wall thickness 58 in. long	7.86 (approx.)	8.402 E-3
	Fuel Clad (3025 tubes)	Low-carbon steel 0.15 w/o C	5/16 in. O.D. 0.018 in. wall thickness 50 in. long	7.86 (approx.)	0.4527

TABLE 2.1 (continued)

Region/ Thickness	Component	Material	Dimensions	Material Density (g/cm^3)	Homogenized Density (g/cm^3)
	Grid support tubes (100 tubes)	Low-carbon steel 0.15 w/o C	7/16 in. O.D. 0.028 wall thickness 48 in. length	7.86 (approx.)	3.301 E-2
	Sodium Chromate	Anhydrous sodium chromate powder Na_2CrO_4 0.10 w/o water	49.5 in. long	-	1.094
	Uranium Fuel Rod (3025 rods)	Uranium metal: 60 rods/assem. 1.016 w/o en. 61 rods/assem. 1.143 w/o en.	0.250 in. dia. 48 in. long	1.016 w/o enrichment: 18.898 1.143 w/o enrichment: 18.92	1.016 w/o enrichment: 1.588 1.143 w/o enrichment: 1.617
	First Reflector Zone 18 in.	Steel Assemblies	Type C-1018 steel Cold rolled 0.18 w/o C 0.75 w/o Mn 99.07 w/o Fe	18 in. thick, 47-3/4 in. high ~ 60 in. wide	7.86
	Second Reflector Zone 12 in. (nominal) 14.00 in.(actual)	Steel Plate (12 plates)	Hot rolled, mild steel 0.15 w/o C	1 in. by 60 in. by 58-1/4 in.	7.86 (approx.)
Concrete 4 ft.	Concrete	Magnetite Concrete	4 ft. thick	3.84	3.84

TABLE 2.2

Number Densities for Blanket Mockup No. 6 (Ref. M1)

Region	Isotope or Element	Number Density (nuclei/cc)
Converter, graphite	C	8.275 E22
Converter, First Fuel Zone 1.99 w/o enrichment	U^{238}	1.391 E22
	U^{235}	2.862 E20
	O	2.840 E22
	Al	1.223 E22
Converter, Second Fuel Zone 1.099 w/o enrichment	U^{238}	1.379 E22
	U^{235}	1.555 E20
	O	2.789 E22
	Al	1.202 E22
Al Backing and Boral Sheet	Al	5.241 E22
	B	1.313 E22
	C	3.282 E21
Blanket	U^{235}	8.872 E19
	U^{238}	8.020 E19
	O	1.629 E22
	Na	8.127 E21
	Cr	4.063 E21
	Fe	1.372 E22
	C	9.585 E19
	H	7.313 E19
First Reflector Region	C	7.095 E20
	Mn	6.463 E20
	Fe	8.398 E22
Second Reflector Region	C	5.913 E20
	Fe	8.464 E22
Concrete	Fe	2.229 E22
	Si	2.309 E21
	Mg	1.721 E20
	Al	5.442 E20
	Ca	3.835 E21
	H	2.208 E22
	O	5.052 E22

Ref. M1. The converter specifications are identical to those documented in Ref. M1, since the same converter configuration has been used for all recent mockups.

2.3 DESIGN OF THE INTERFACE TRAVERSING SUBASSEMBLY (ITS)

2.3.1 The Purpose of the ITS Design

Blanket neutronics are studied experimentally by measuring the reaction rates of specific foils inserted in fuel rods in blanket subassemblies. Figure 2.3 shows the position of the experimental fuel rods in previous blanket subassemblies. The information provided by this type of subassembly would be one data point every 3 inches. For studying interfacial effects, one needs to have more detailed information near the interface. Also, it would be useful to have a special subassembly that can provide the capability of studying interfacial effects at all of its boundaries. Therefore a decision was made to design a new blanket subassembly having the utmost capability in providing data, that is to say any or all of its fuel rods can be transformed into an experimental fuel rod. It was decided that aluminum-clad UO_2 fuel rods would be used in a hexagonal lattice, rather than the carbon-steel-clad uranium metal fuel rods used in conventional blanket mockup subassemblies (see Figure 2.4). This provided greater similarity to an actual LMFBR blanket, and furthermore, aluminum-clad UO_2 fuel rods were available in the project's fuel inventory.

2.3.2 Calculations

The design optimization was accomplished using one- and two-dimensional state-of-the-art analyses of BTF No. 6; calculations were made for the case when the central subassembly of the blanket is replaced by the test

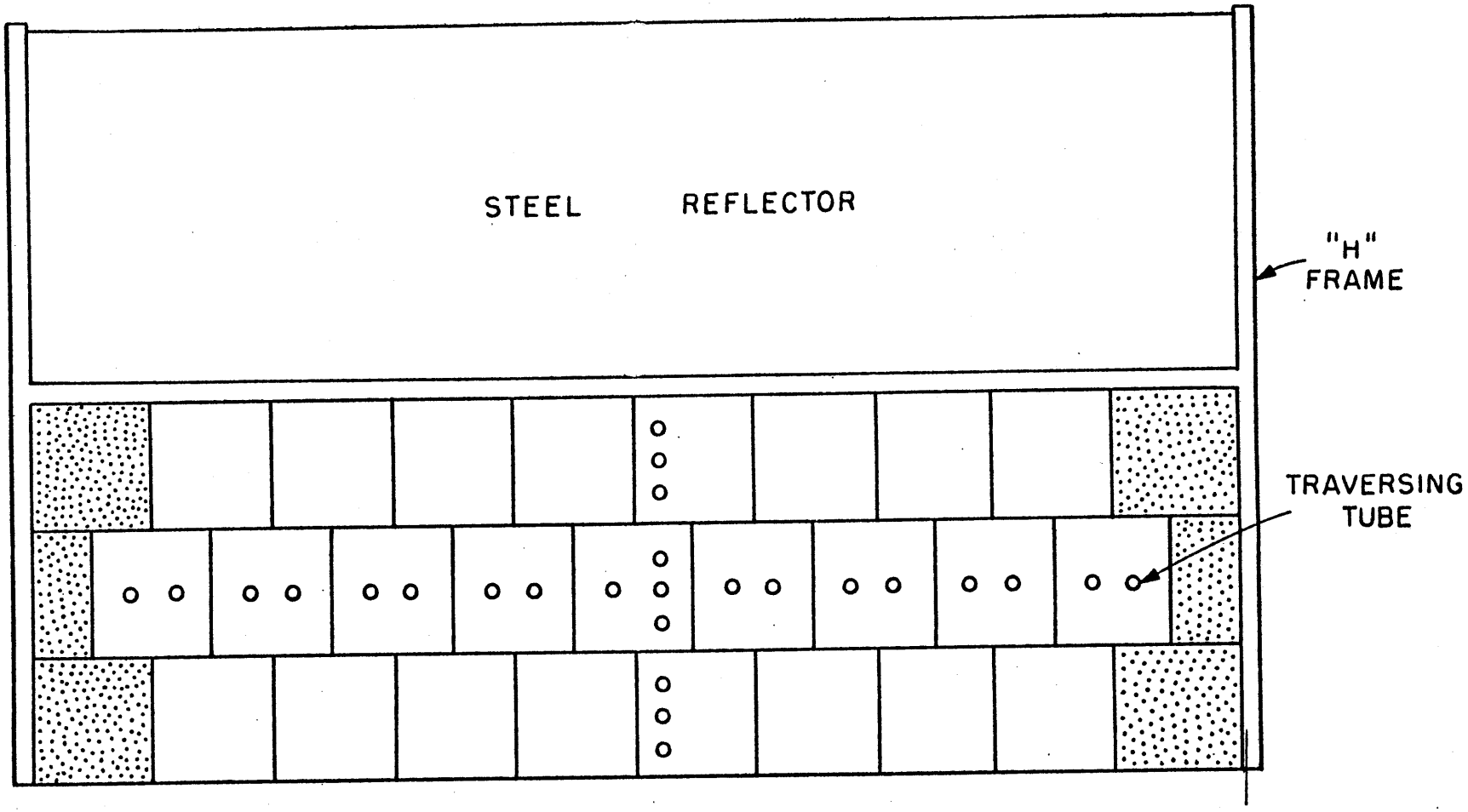

FIG. 2.3 PLAN VIEW OF BLANKET ASSEMBLY SHOWING THE TRAVERSING TUBE POSITIONS

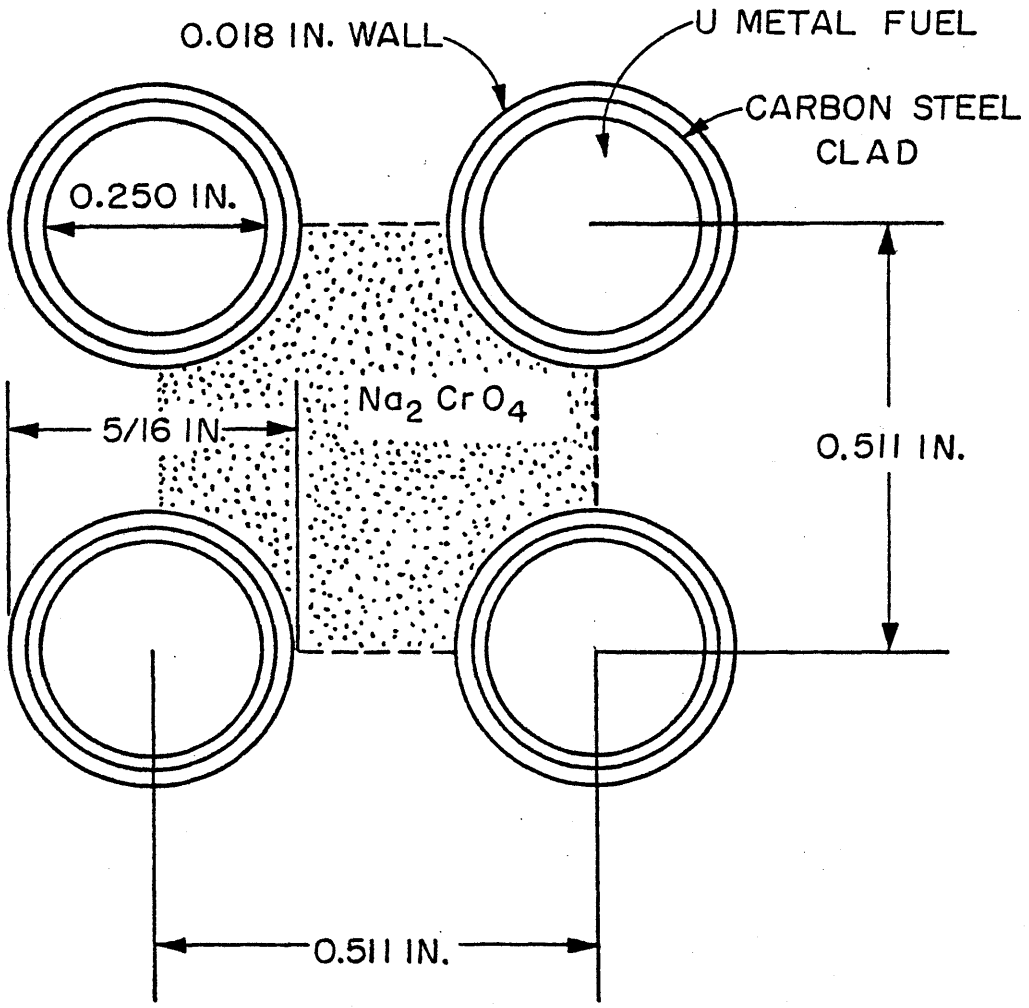

Fig. 2.4 STANDARD BLANKET ASSEMBLY UNIT CELL

subassembly. Even though the test subassembly will be placed adjacent to the reflector for interfacial effect studies, in the optimization process, it was placed in the center of the blanket assembly surrounded by other blanket subassemblies in order not to obscure the comparison by difficult-to-calculate interfacial effects.

ANISN CALCULATIONS One dimensional calculations were performed with the ANISN (Ref. A1) multigroup transport code using a 26-group self shielded cross section set generated by self-shielding the 50-group LIB-IV cross section set (Ref. K1, M1) and collapsing it into a 26-group set. The energy group structure of the 26-group set (and a 4-group cross section sub-set) are given in Table 2.3. The one dimensional model of Blanket Mockup No. 6 used in the ANISN calculations is shown in Figure 2.5. In these calculations, the entire central row of the blanket (shown cross-hatched in Figure 2.5) has the same atomic number densities as the test assembly being designed; exaggerating the effect of the test assembly in this manner accentuates the sensitivity of the comparison.

2DB CALCULATIONS Two-dimensional calculations were performed with the 2DB (Ref. L1) few-group diffusion theory code using a 4-group cross-section set generated by collapsing the 26-group cross-sections into 4-groups using the ANISN code. This code provides collapsed cross section sets of the specified materials over all zones specified in the BTF one-dimensional model. Figure 2.6 shows the two-dimensional model of BTF Mockup No. 6 used in the 2DB calculations.

TABLE 2.3

Group Structure of Cross Section Sets

26 Group			4 Group		
Group #	Upper Energy (Ev)		Group #	Upper Energy (Ev)	
1	1.99711	E + 07	1	1.99711	E + 07
2	6.06531	E + 06	2	1.35335	E + 06
3	3.67879	E + 06	3	4.08667	E + 04
4	2.23130	E + 06	4	2.03468	E + 03
5	1.35335	E + 06	Lower Bound	1.00000	E - 05
6	8.20850	E + 05			
7	3.87742	E + 05			
8	1.83156	E + 05			
9	1.11090	E + 05			
10	4.08677	E + 04			
11	1.93045	E + 04			
12	9.11882	E + 03			
13	4.30743	E + 03			
14	2.03468	E + 03			
15	1.23410	E + 03			
16	4.53888	E + 02			
17	1.67017	E + 02			
18	1.01301	E + 02			
19	3.72665	E + 01			
20	2.26033	E + 01			
21	1.37096	E + 01			
22	5.04348	E + 00			
23	3.05902	E + 00			
24	1.85538	E + 00			
25	1.12535	E + 00			
26	6.82560	E - 01			
Lower Bound	1.00000	E - 05			

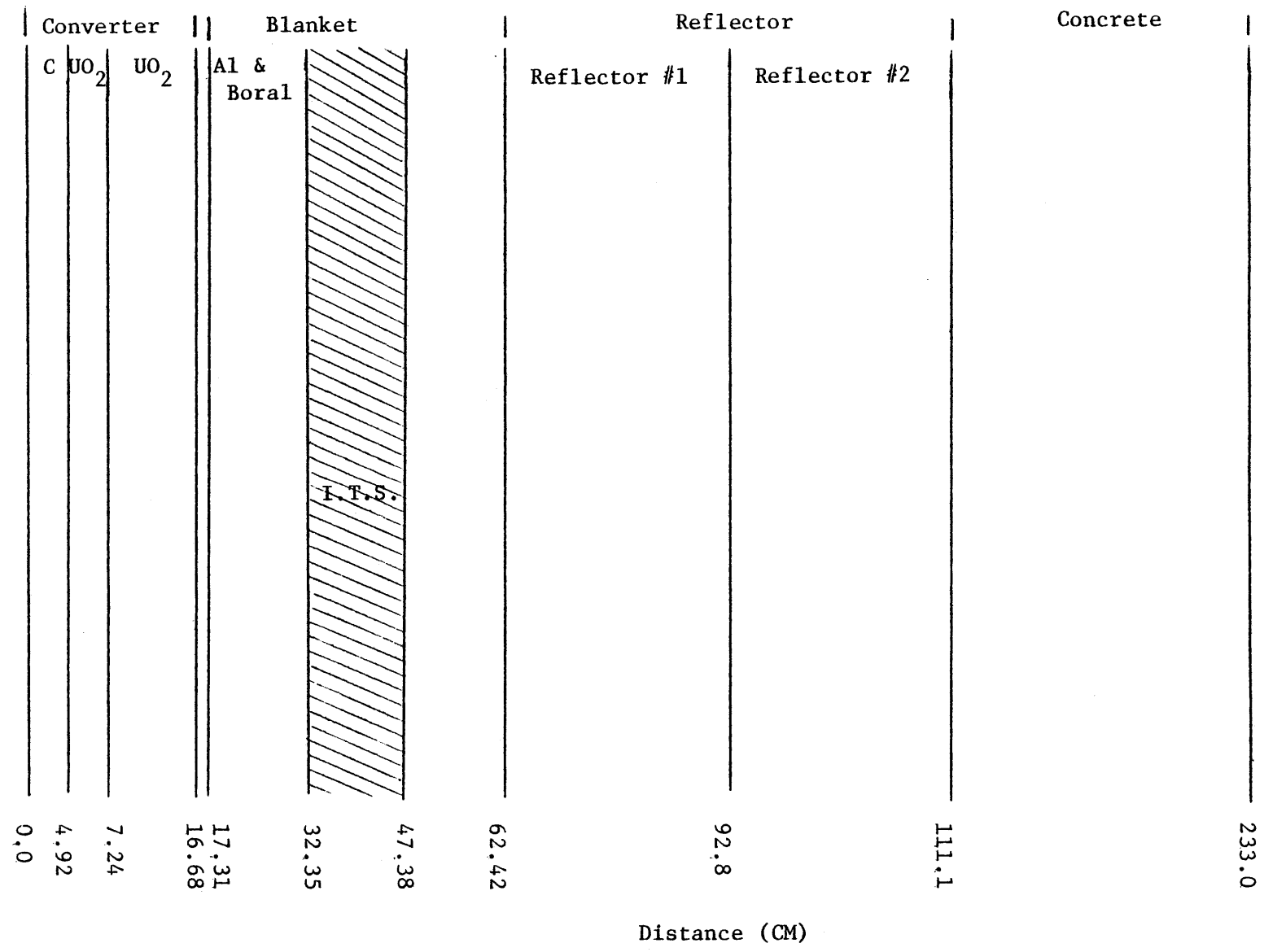

Figure 2.5 CONFIGURATION USED FOR ANISN CALCULATIONS

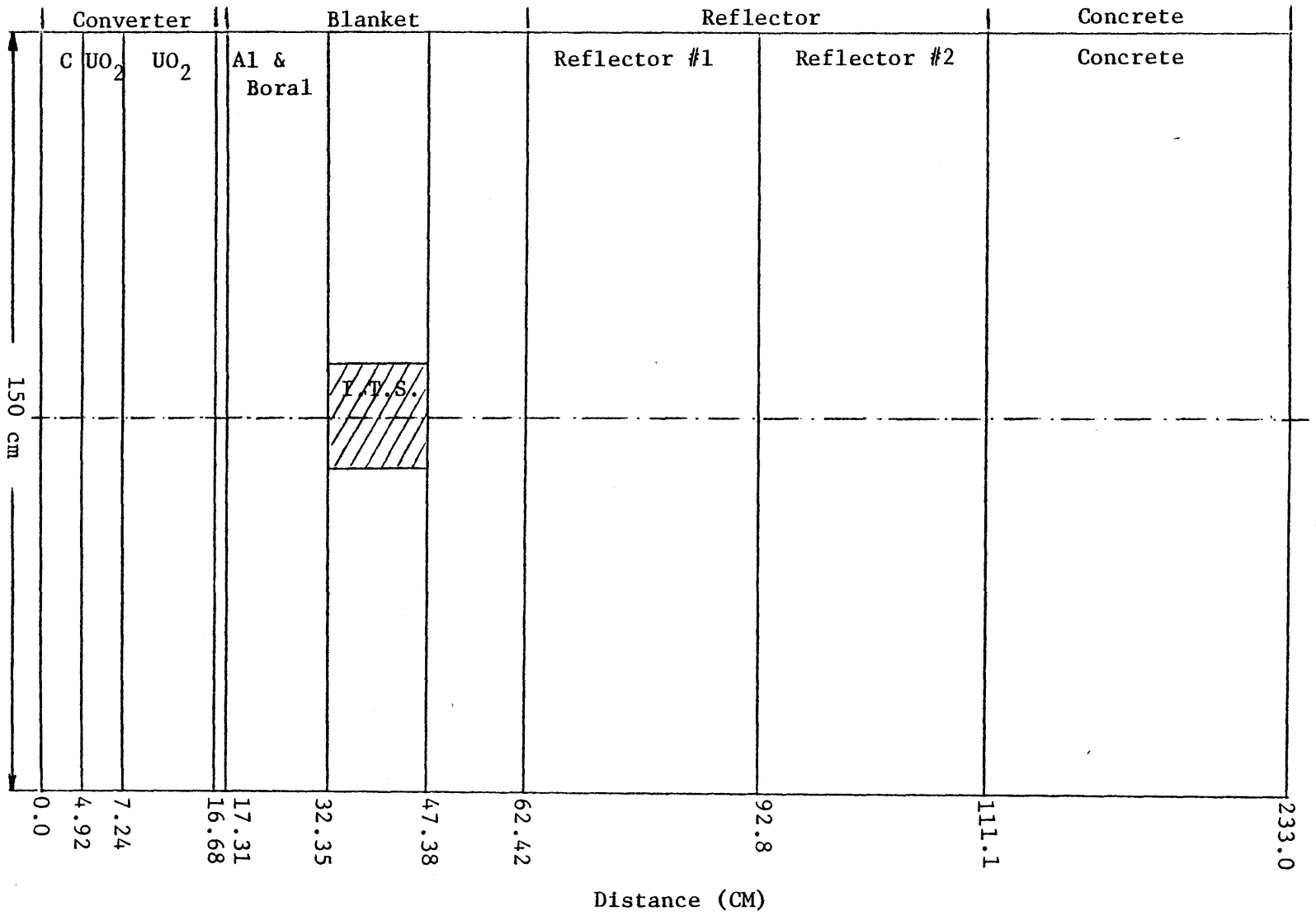

Figure 2.6 CONFIGURATION USED FOR 2DB CALCULATIONS (Top View)

CRITERIA FOR OPTIMIZATION Different materials and a variety of compositions were examined, with emphasis on the "moderator" (i.e. non-fuel) region of the unit cell. Matching the spectrum averaged slowing down powers of the conventional blanket moderator and the new blanket subassembly moderator would in principle provide neutronic similitude. This approach provided a systematic scheme for initial scoping studies. Starting from this point, the atomic number densities were changed to get a better match to various indices of comparison. Since aluminum had been used as a substitute for sodium coolant in earlier fast reactor research (Ref. P1), it was the first material examined. Later, other elements such as magnesium and carbon and mixtures and chemical compounds of these elements, such as Al_2O_3, MgO and Na_2CO_3 were examined. The criteria for optimization are twofold, namely satisfaction of practical engineering constraints and provision of neutronic similitude. The engineering constraints are: (a) the material chosen for substitution is within the limitations imposed by MIT Reactor safety regulations, (b) the material can be easily handled, (c) it is commercially available, (d) the design lends itself to practical construction practice. The neutronic comparability refers to whether the following quantities match in both conventional and new blanket subassemblies, namely, (a) the spatial distribution of the total neutron flux,(b) the neutron energy spectrum at the middle of the blanket subassembly, and more specifically (c) the spatial distribution of the U^{28} capture rate and the ratio of U^{28} capture to U^{25} fissions (U_c^{28}/U_f^{25}).

2.3.3 Final Design of ITS

Utilizing the ANISN and 2DB codes, an optimum design for the ITS was found. The final design of the ITS satisfied the criteria for

optimality in the results obtained from both the ANISN and 2DB codes. Figure 2.7 shows the unit cell of the ITS and Figure 2.8 shows a top view of the ITS. As shown, the subassembly consists of 85 removable Al-clad UO_2 fuel rods which slide into stainless steel tubes, in a hexagonal lattice having a 0.61 inch-pitch; the space in between the stainless steel tubes is filled with anhydrous Na_2CO_3 powder with a measured density one third that of solid crystalline Na_2CO_3 (2.533 g/cm^3). It was found that the optimization is not very sensitive to the amount of Na_2CO_3 used, therefore small deviations from the optimum value of the Na_2CO_3 density as a result of variations in as-loaded density will not compromise the design. In order to show this, and also to show how close the final subassembly design simulates the other assemblies in blanket mockup No. 6, the results of the calculations for three cases are given; blanket mockup No. 6 with and without the test assembly, and the latter case without Na_2CO_3 powder. Table 2.4 gives the atomic number densities of a blanket subassembly for each of these three cases. Figures 2.9 through 2.12 show the spatial distribution of U_c^{28} and U_f^{25} rates through the central blanket subassembly of these three cases, calculated using ANISN and 2DB.

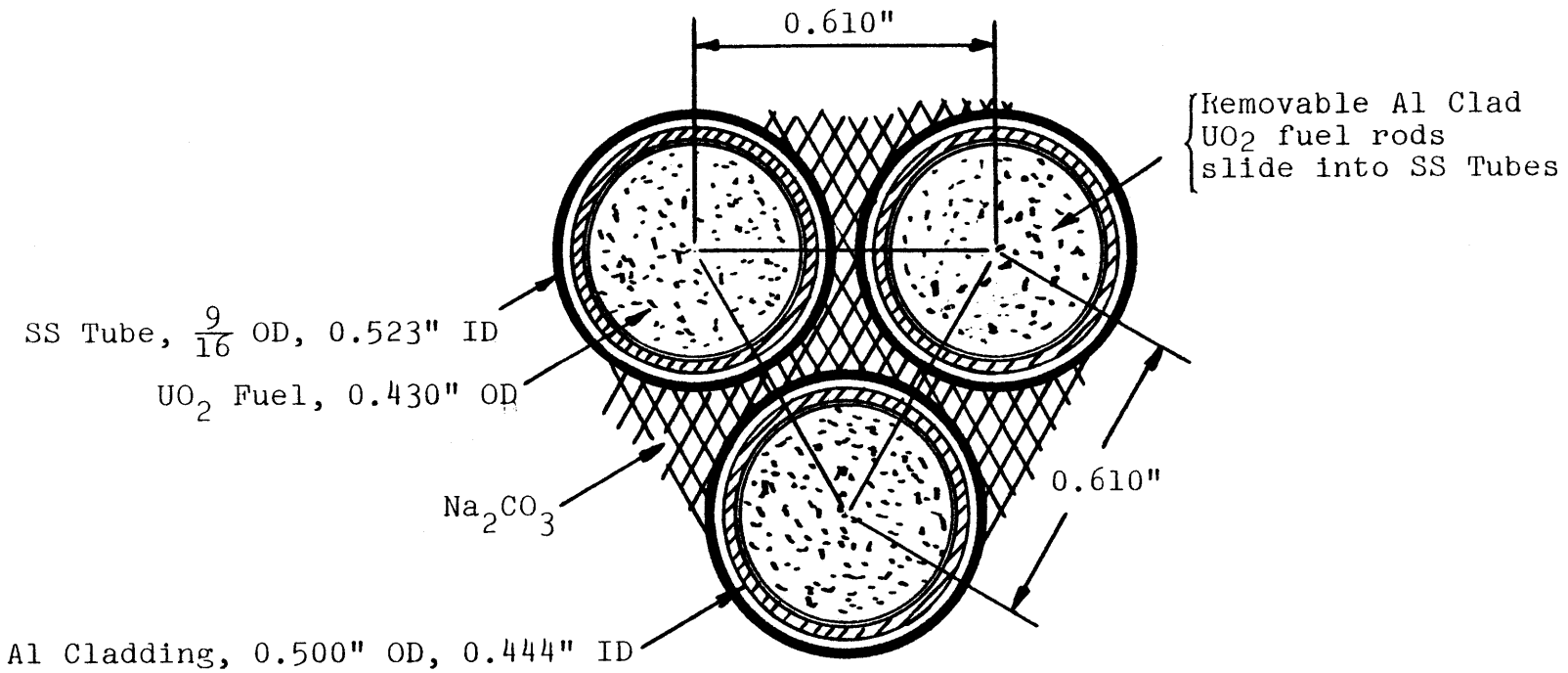

FIG. 2.7 Unit Cell of Special Interface-Traversing Subassembly

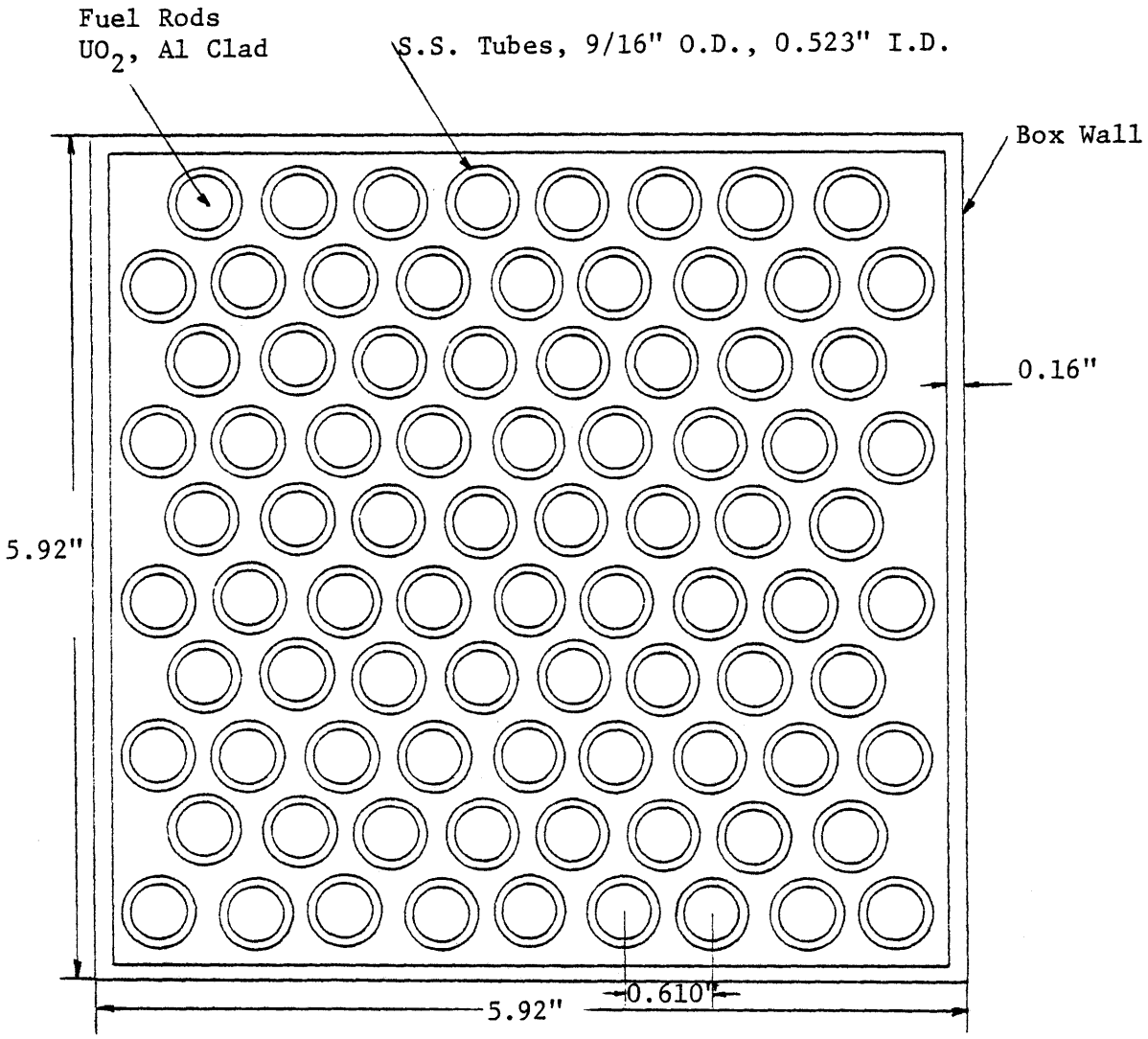

Fig.2.8 FUEL ARRANGEMENT IN SPECIAL SUBASSEMBLY

TABLE 2.4

ATOMIC NUMBER DENSITIES FOR COMPARATIVE CALCULATIONS

Isotope or Element	Atomic Number Densities (nuclei/cc)		
	Blanket No. 6 Subassembly	ITS	ITS without Na_2CO_3
U^{238}	8.872 E19	9.002 E19	9.002 E19
U^{235}	8.020 E21	7.990 E21	7.990 E22
O	1.629 E22	2.258 E22	1.616 E22
Na	8.127 E21	4.238 E21	-
Al	-	6.898 E21	6.898 E21
C	9.513 E19	2.108 E21	2.597 E19
Fe	1.362 E22	1.406 E22	1.406 E22
Cr	4.063 E21	1.348 E21	1.348 E21
Ni	-	5.310 E20	5.310 E20
H	7.313 E19	-	-

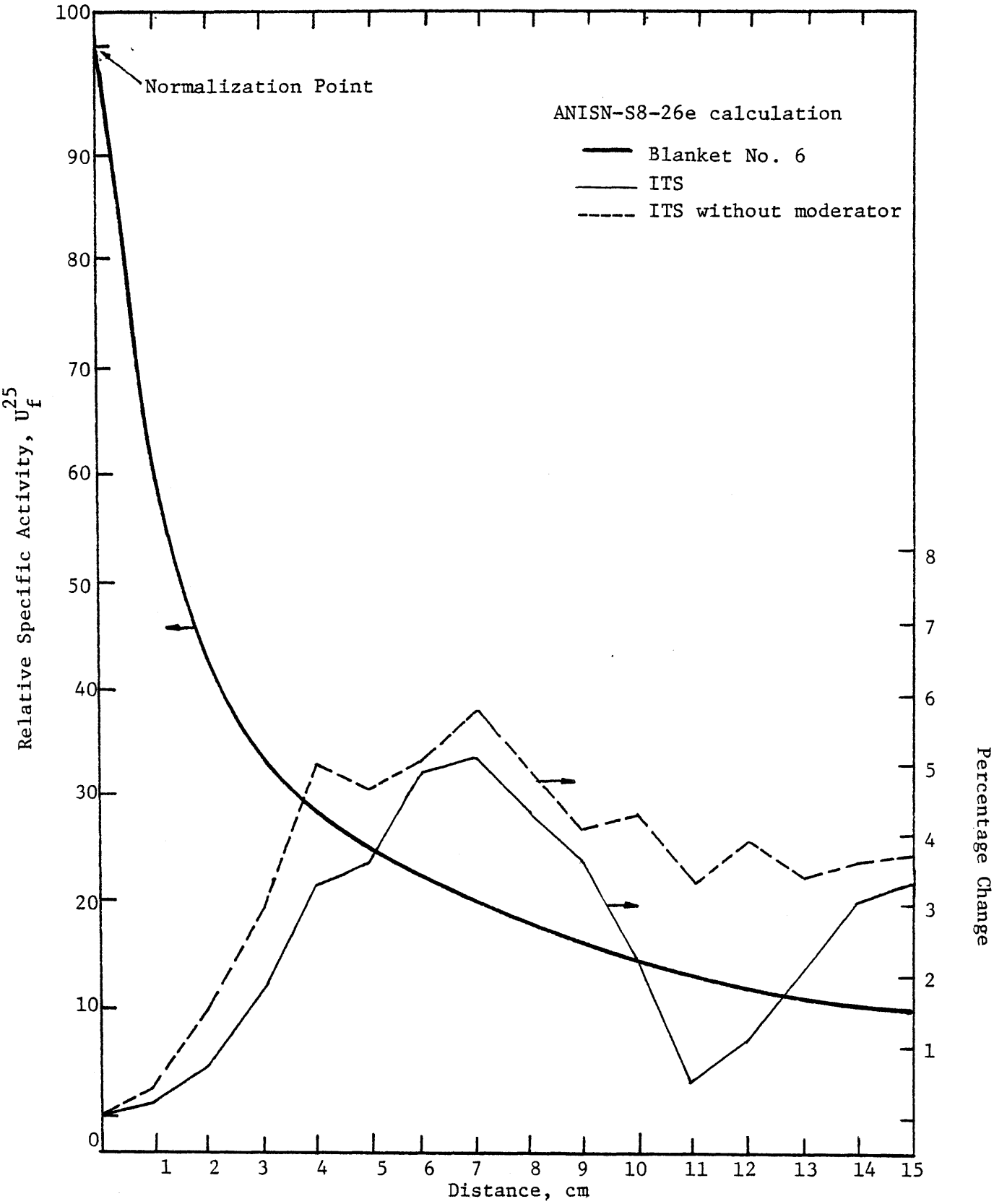

Figure 2.9 U_f^{25} DISTRIBUTION IN BLANKET NO. 6 WITH AND WITHOUT THE ITS

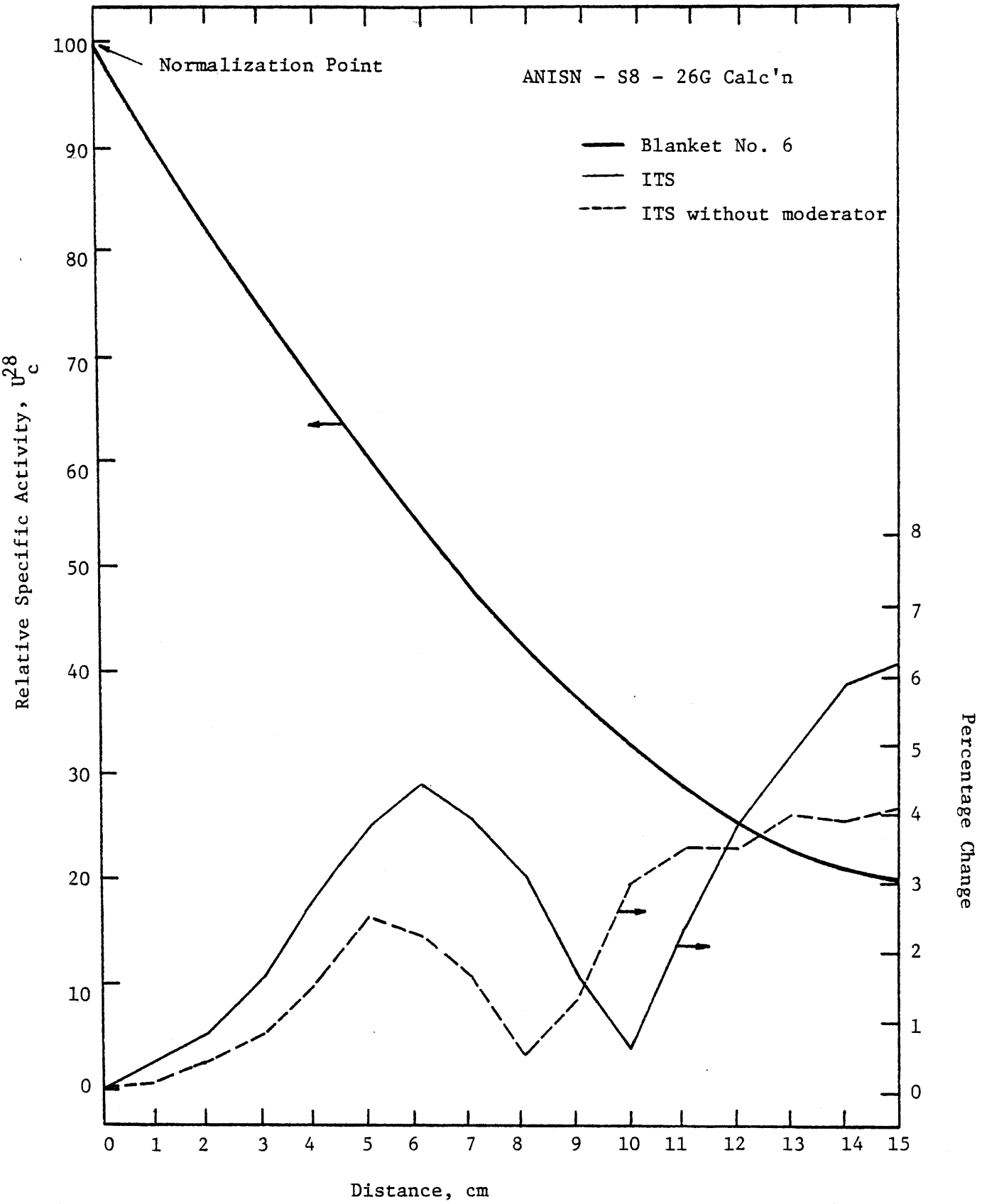

Fig. 2.10 U_c^{28} DISTRIBUTION IN BLANKET NO. 6 WITH AND WITHOUT THE ITS

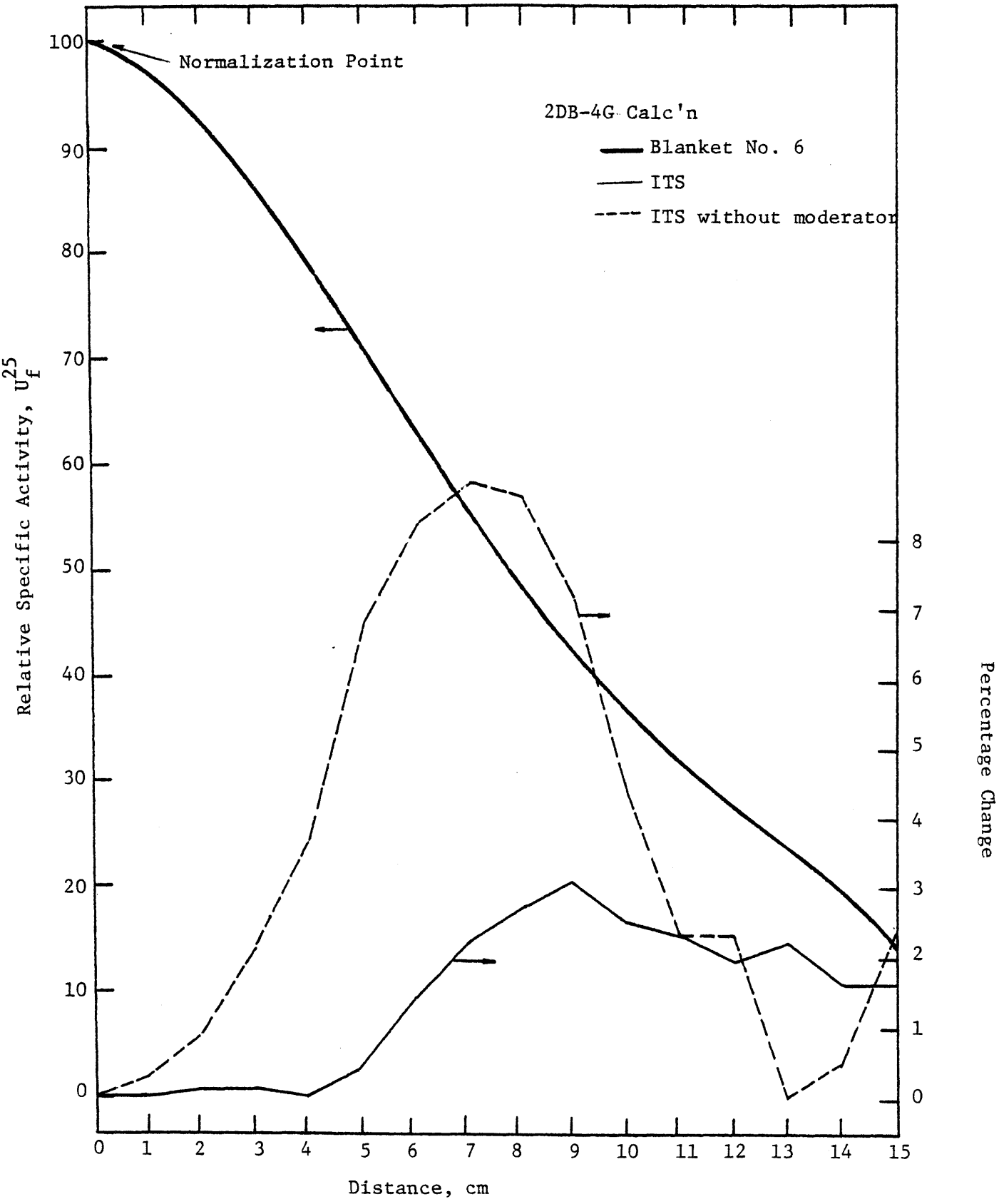

Fig. 2.11 U_f^{25} DISTRIBUTION IN BLANKET NO. 6 WITH AND WITHOUT THE ITS

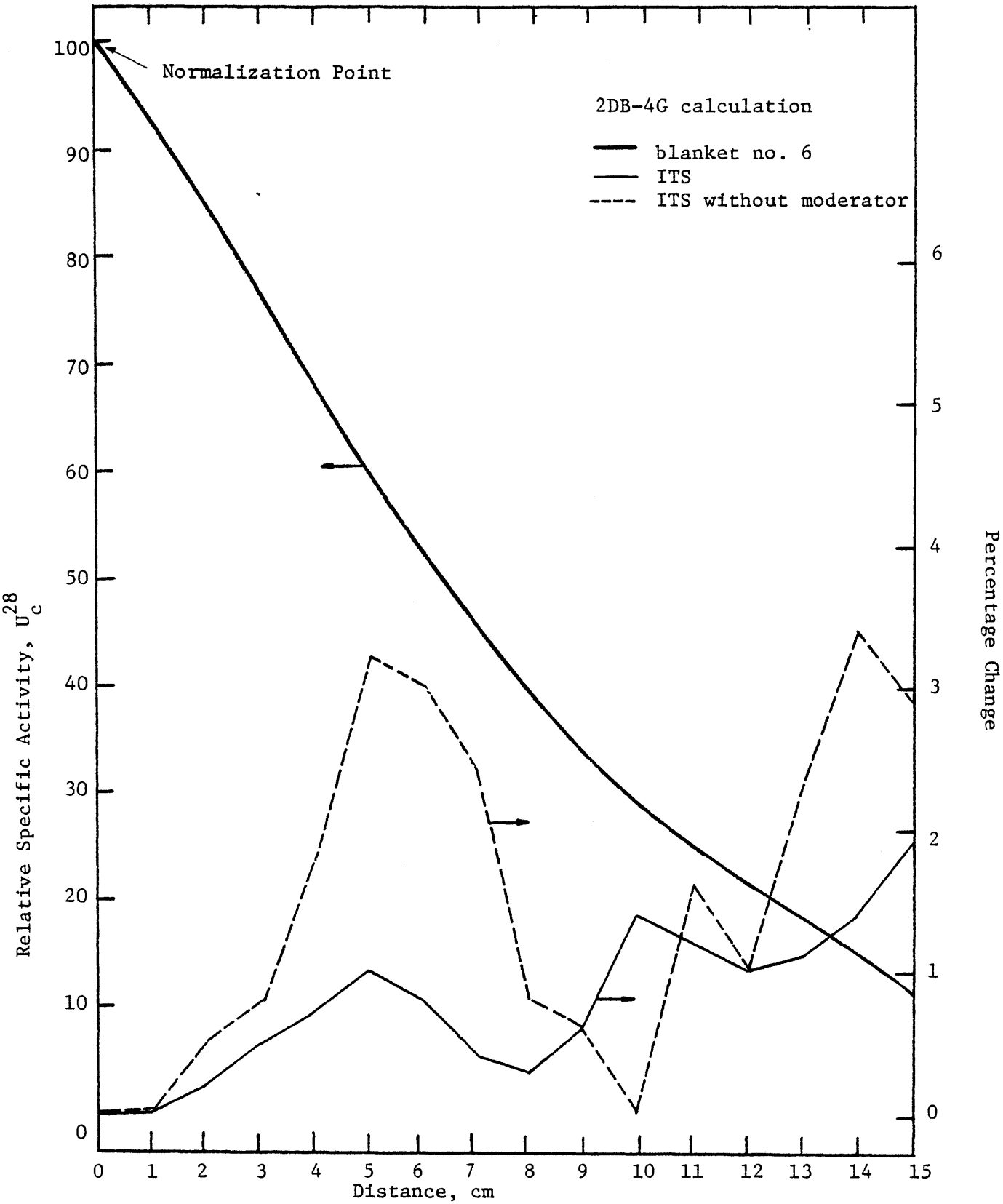

Figure 2.12 U_c^{28} DISTRIBUTION IN BLANKET NO. 6 WITH AND WITHOUT THE ITS

2.4 CONSTRUCTION OF THE ITS

The as-built ITS consists of 85, 4 ft. long, 9/16 in. O.D. and 0.523 in. I.D. stainless steel (type 321, having a density of 7.92 g/cc) tubes placed in a 4.2 ft. long square low-carbon steel (0.15 w/o C; 7.86 g/cc density) open ended box with 5.92 in sides and an 0.16 in. wall thickness. The stainless steel tubes are held in a hexagonal lattice layout (see Figure 2.8) using two (type 1100) aluminum grids, at top and bottom. The bottom grid (5.6 in. by 5.6 in. by 0.25 in.) is sealed (with epoxy) to a solid aluminum end plate having the same dimensions. Stainless steel tubes were fitted into the bottom grid holes and sealed in place with epoxy to prevent any leakage from the moderator region into the tubes, and hence preventing the fuel rods from becoming contaminated by moderator in-leakage. The top grid (5.6 in. x 5.6 in. x 0.125 in.) is placed at a distance of one inch from the top of the stainless steel tubes. Figures 2.13 and 2.14 show the subassembly lattice before it was inserted into the steel box. As can be seen numerous holes are cut through the top grid to allow later ingress to the Na_2CO_3 powder. After inserting the subassembly into the steel box, Na_2CO_3 powder was poured over the top of the subassembly, and using an electric hammer to shake the box, the powder was allowed to fill the spaces between the stainless steel tubes uniformly. During this operation, the stainless steel tube tops were plugged with rubber stoppers. The total amount of Na_2CO_3 powder loaded weighed 10281.5 grams. That makes the homogenized density of Na_2CO_3 over the subassembly equal to 0.373 g/cc, which is quite close to the Na_2CO_3 density in the optimum design calculation (0.36 g/cc). The top grid cut outs were then sealed with epoxy to prevent any subsequent

Fig. 2.13 ISOMETRIC VIEW OF ITS

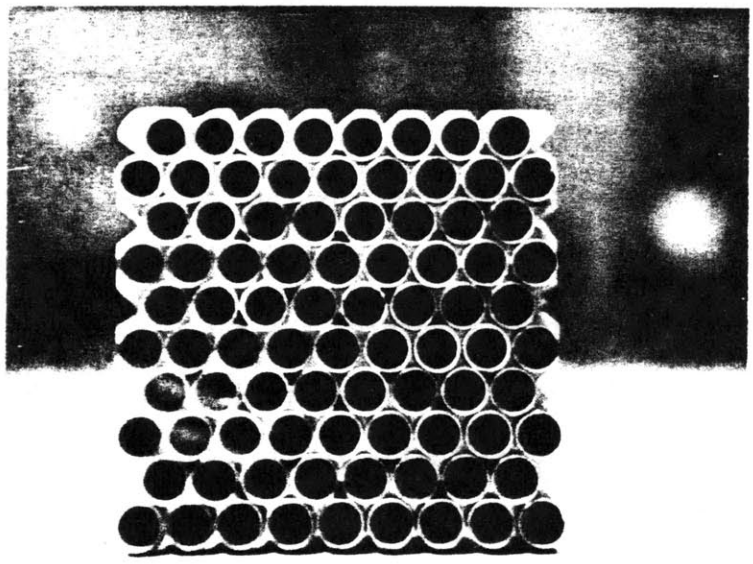

Fig. 2.14 TOP END VIEW OF ITS

loss of the Na_2CO_3 powder and to prevent absorption of moisture by the powder. The subassembly was then loaded with its fuel rods and with special experimental fuel rods. Uranium oxide fuel rods with Al cladding (type 1100) are used. A typical fuel rod contains UO_2 pellets (containing 1.099 w/o U-235) having an 0.431 inch diameter, and various lengths ($\sim$ 5/8 in. to 1 in.). The total uranium per rod weighs 1035.396 grams (total U^{25}/Rod = 11.388 grams). Figure 2.15.a shows a typical fuel rod. The end plugs are aluminum (type 1100) and the diameter at the weld on the end plugs is 0.515 inches. The experimental fuel rod is essentially identical to a fuel rod, except that its pellets can be slipped out to permit insertion of the desired foils at the proper positions inside the fuel rod, for measuring horizontal and/or vertical reaction rate distributions. For this purpose, some of the standard fuel rods were initially transformed into experimental rods by cutting off their tops and removing the fuel pellets. When these rods were again loaded with pellets and interspersed foils, and the first set of experiments was performed, the pellets could be removed only with great effort, and in some cases, the rods had to be cut open in order to reach the foils. Therefore another design for the experimental rods was adopted. Since the foils were only to be situated near the center of the rod, some fuel rods were cut into three segments; the top and bottom segments were sealed with epoxy, and the middle segments into which foils were to be inserted, were prepared (by polishing the internal surface) so that pellets could be easily loaded and unloaded. Figure 2.15.b shows a typical experimental fuel rod. The middle segment was attached to the top segment using 3-mil thick Mylar tape, and for loading and unloading the foils only these two attached segments were removed from the blanket subassembly.

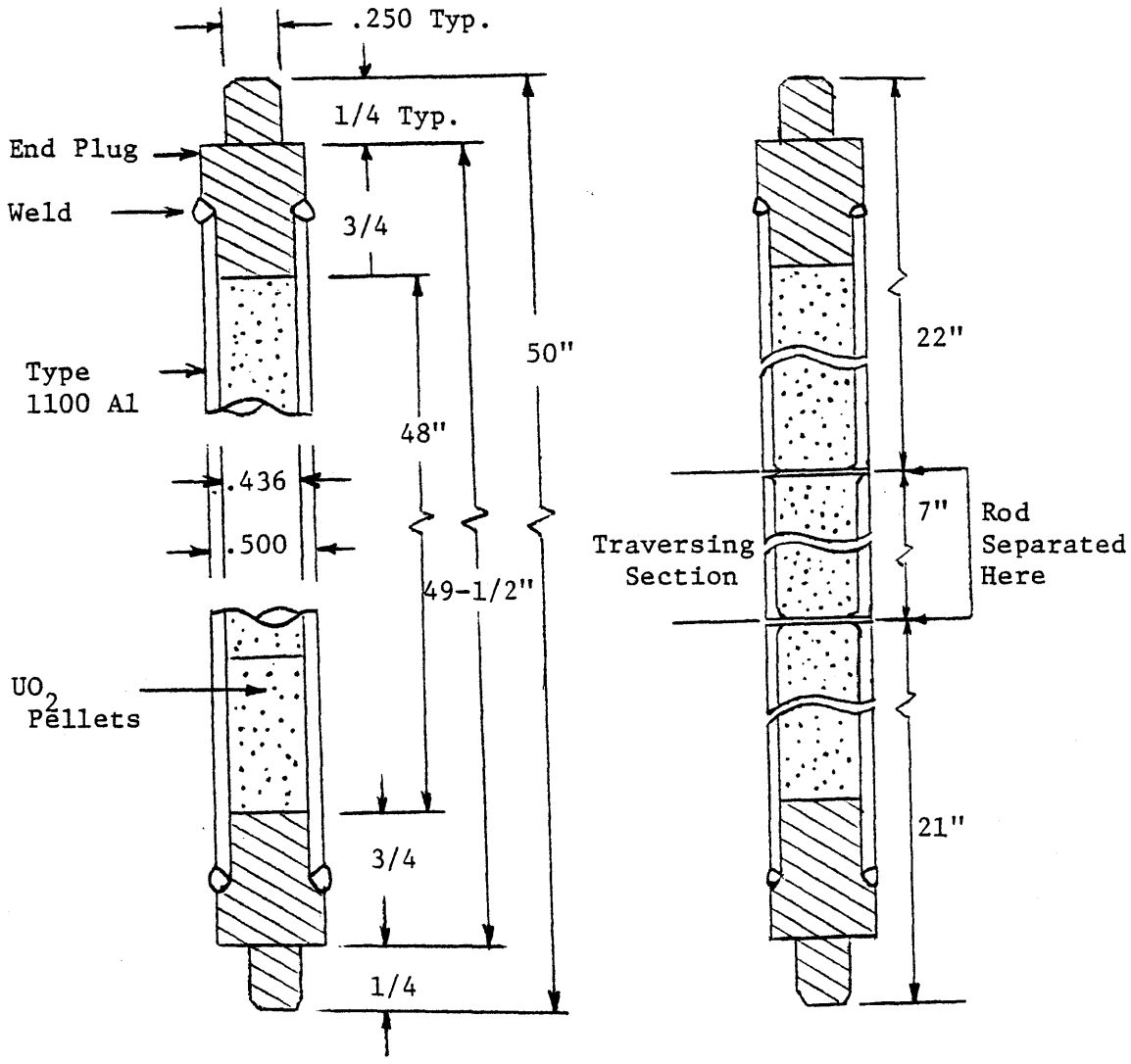

(a) Standard Rod (b) Experimental Rod

Fig. 2.15 DESIGN OF STANDARD AND EXPERIMENTAL FUEL RODS USED IN THE ITS

The bottom segments were left in position. Table 2.5 shows the atomic number densities of the as-built blanket subassembly in comparison with the design specifications.

2.5 SUMMARY AND CONCLUSIONS

In this chapter, after showing that the available MIT Blanket Test Subassemblies were unable to meet the needs of present interest, another more suitable subassembly was designed. The criteria for design were both practical (maximizing the accessibility to the fuel rods for foil insertion) and theoretical (matching the neutronics of the surrounding conventional subassemblies). Using the ANISN and 2DB codes, the ITS was designed and built with the following features: a hexagonal lattice, Al clad UO_2 fuel rods inserted into stainless steel tubes and "moderated" by dry Na_2CO_3 powder. This design provides the capability for studying interfacial effects on any boundary of the blanket subassembly.

TABLE 2.5

Comparison of Number Densities of Designed vs. Constructed ITS

Isotope or Element	Constructed ITS*	Designed ITS*
U^{238}	9.002 E19	9.002 E19
U^{235}	7.990 E21	7.990 E21
O	2.258 E22	2.049 E22
Na	4.238 E21	4.164 E21
Al	6.898 E21	6.089 E21
C	2.108 E21	2.108 E21
Fe	1.406 E22	1.023 E22
Cr	1.348 E21	1.350 E21
Ni	5.310 E20	5.310 E20

*differences are due primarily to such factors as the inability to predict in advance the exact packing density of Na_2CO_3 powder

CHAPTER 3

ITS EXPERIMENTS AND RESULTS

3.1 INTRODUCTION

As suggested in Chapter 2, our intent is to measure the horizontal distribution of the U^{28} capture rate and the U_c^{28}/U_f^{25} ratios near the blanket-reflector interface. It is also desired to study the U_c^{28} rate through the fuel rods nearest to the reflector, where changes in the U^{28} self-shielding are most pronounced. The required reaction rates were measured using depleted and enriched uranium foils. After the first experimental runs, it was decided to also monitor the Au^{197} capture reaction rate to obtain an indication of the total neutron flux distribution.

The experimental procedure is covered in Section 3.2, followed by the presentation of experimental results in Section 3.3 This chapter is concluded by a brief summary in Section 3.4.

While standard procedures used in conjunction with blanket operation have been well documented in a series of reports (D2, D3), sufficient information is repeated here to characterize the essential features of the present work.

3.2 EXPERIMENTAL PROCEDURE

3.2.1 Description of Foil Materials

The physical characteristics of the detector foil materials which were used in the reaction rate measurements in the ITS of Blanket Mockup No. 6 are listed in Table 3.1. The "mini-foils" are small (0.056 in. diameter) foils cut out of a highly depleted uranium metal foil (18 ppm U^{25}) which is 0.431 inches in diameter, 5 mils thick and 204.45 milligrams in weight (see Fig 3.1), and "ring-foils" are six concentered uranium foils (188 ppm U^{25})

TABLE 3.1

Physical Specifications of Foil Materials

Reaction	Foil Material	Diameter (inch)	Thickness (mils)	Typical Weight (mg)	Purity (weight %)
$^{197}Au(n,\gamma)^{198}Au$	Dilute gold in Al	0.431	5	22	4.3
$^{238}U(n,\gamma)$	Depleted Uranium	0.431	5	180	170 ppm U-235
$^{235}U(n,f)$	Dilute Uranium in Al	0.431	5	35	U in foil 10% enrichment 93.17%
$^{238}U(n,\gamma)$	Highly depleted Uranium (mini-foil)	0.056	5	3.5	18 ppm U-235
$^{238}U(n,\gamma)$	Highly depleted Uranium (ring foils)	0.431	5	200	18 ppm U-235
	Segment #1	0.902 (outer diameter)	5	8.5	18 ppm U-235
	#2	0.158	5	18.5	18 ppm U-235
	#3	0.226	5	27.5	18 ppm U-235
	#4	0.294	5	37.0	18 ppm U-235
	#5	0.364	5	49.0	18 ppm U-235
	#6	0.431	5	55.0	18 ppm U-235

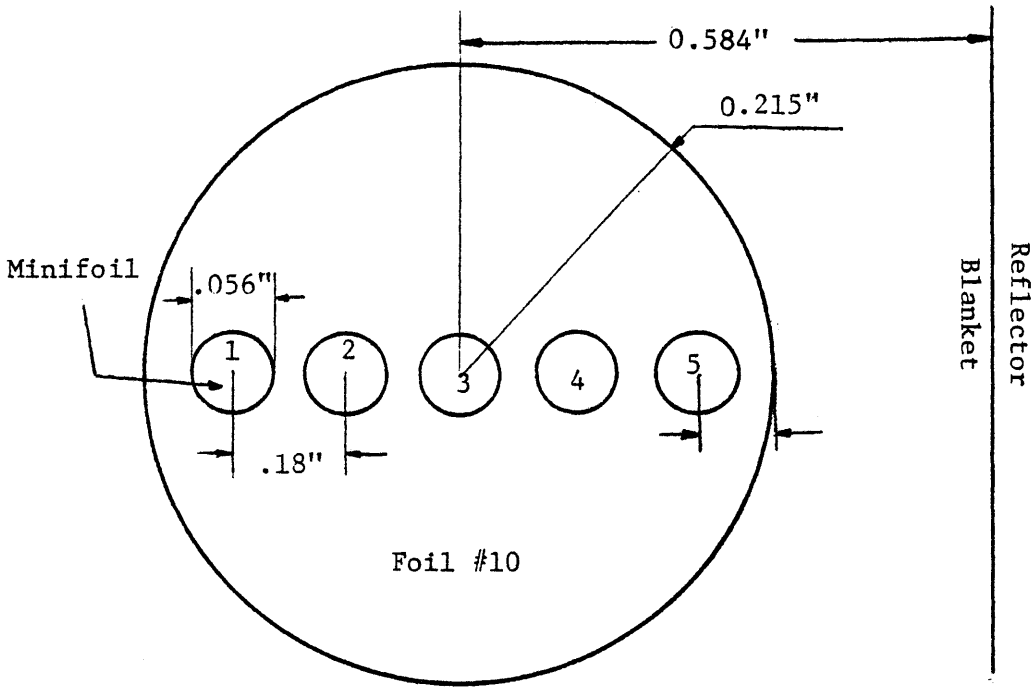

Figure 3.1 MINIFOIL ARRANGEMENT

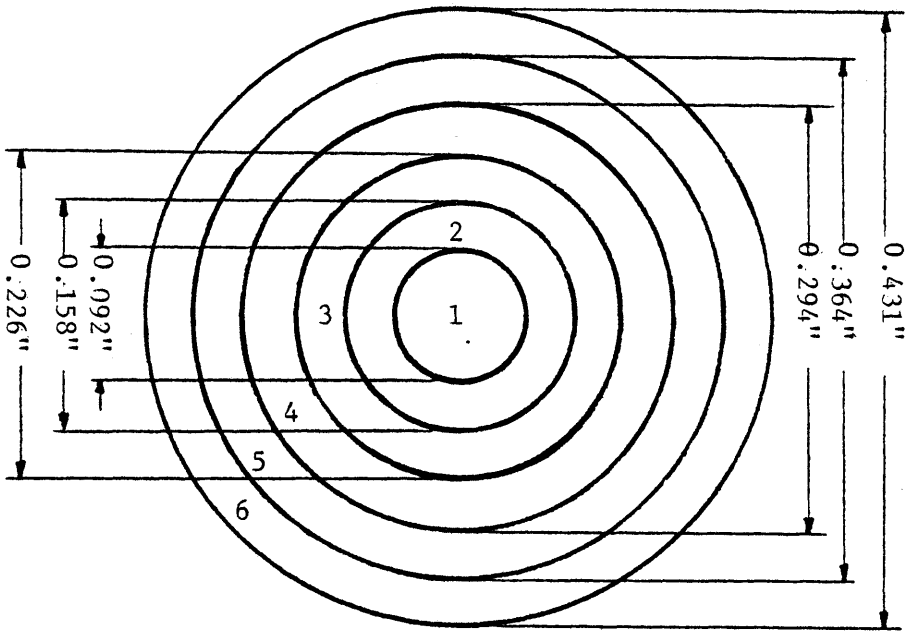

Figure 3.2 RING FOIL ARRANGEMENT

(see Figure 3.2) numbered 1 through 6 from the innermost through the outermost (see Ref. T1 for more information). All foils used are in metallic form, in either disc or ring configuration. The OD of 0.431 in. is selected to match the O.D. of the UO_2 fuel pellets.

3.2.2 Experimental Setup

The position of the ITS in BTF Mockup No. 6 and of the experimental fuel rods in the ITS during the experiments is shown in Figures 3.3 and 3.4. Since a thorium containing special subassembly (Ref. M2) had been placed in the position shown by letter A in the blanket assembly map, Figure 3.3, the ITS was placed off-center, to provide enough distance between special assemblies to preclude any interference the thorium subassembly might induce. In the way that the experimental fuel rods are positioned, not only is more information obtained (ten data points rather than nine data points for the other direction), but the interface is more clearly defined. As shown in Figure 3.4 the experimental fuel rods are numbered 1 through 10; and any foil placed in one of these rods is identified by the selfsame number. Ten depleted uranium foils (designated by "U-238") and ten enriched urainum foils (designated by "U-235") were placed at positions 1 to 30 at heights 23 $\pm$ 1/2 in. and 24 $\pm$ 1/2 in. from the bottom of the ITS, respectively. The 24-inch height is the middle of the fueled length of the fuel rods, and since the axial flux shape (along the vertical axis of the fuel rods) is cosine shaped, it is fairly flat in the central $\pm$ 2 in. region (Ref. M2); thus the U-238 and U-235 foil positions experience equal neutron fluxes. Ten gold foils were placed at the 25 inch height at positions 1 through 10. The gold foils were only used in the second run of the experiments. Since the U-238 resonance self shielding perturbation is pronounced at the

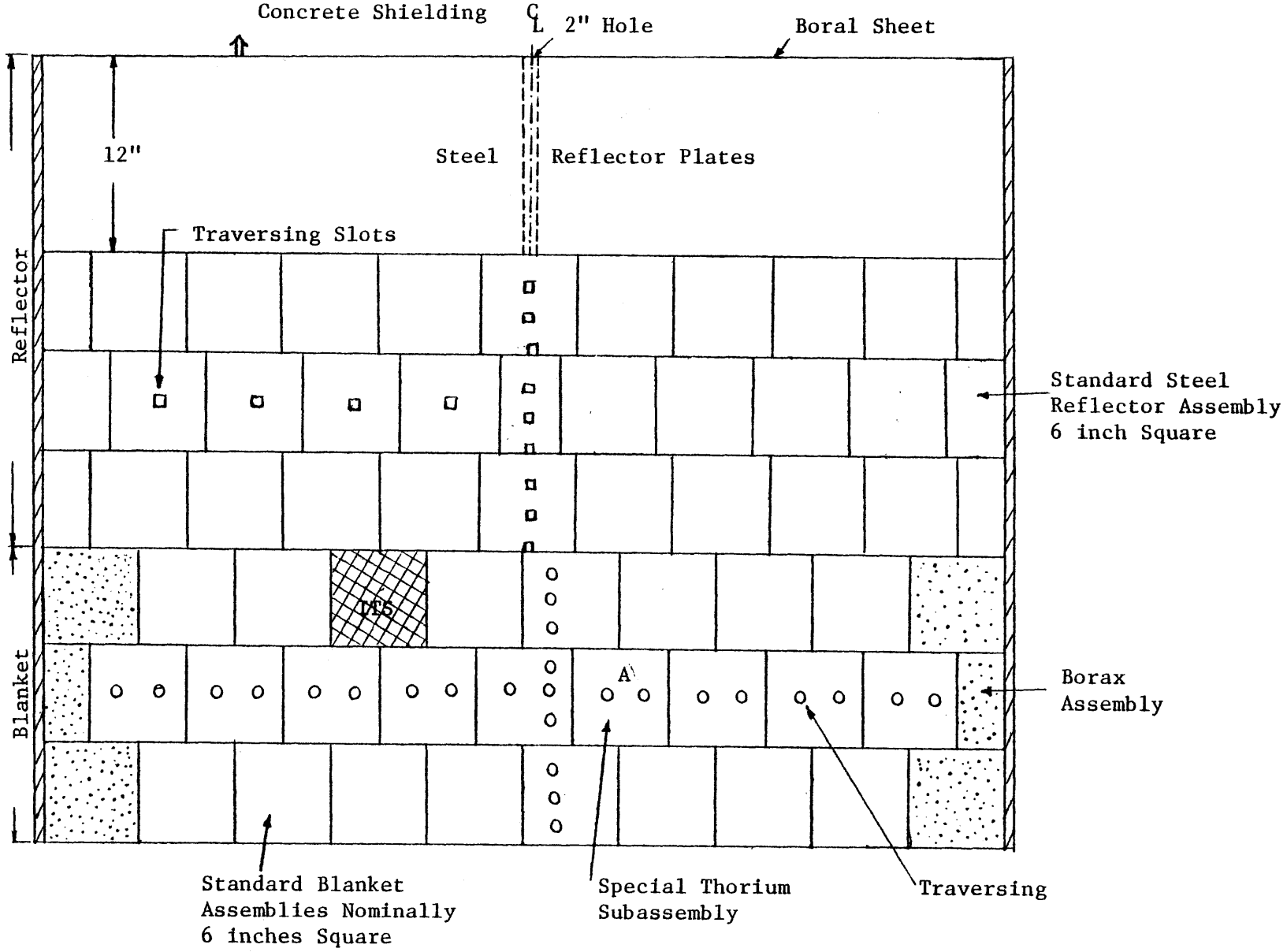

Figure 3.3 TOP VIEW OF BLANKET MOCKUP NO. 6

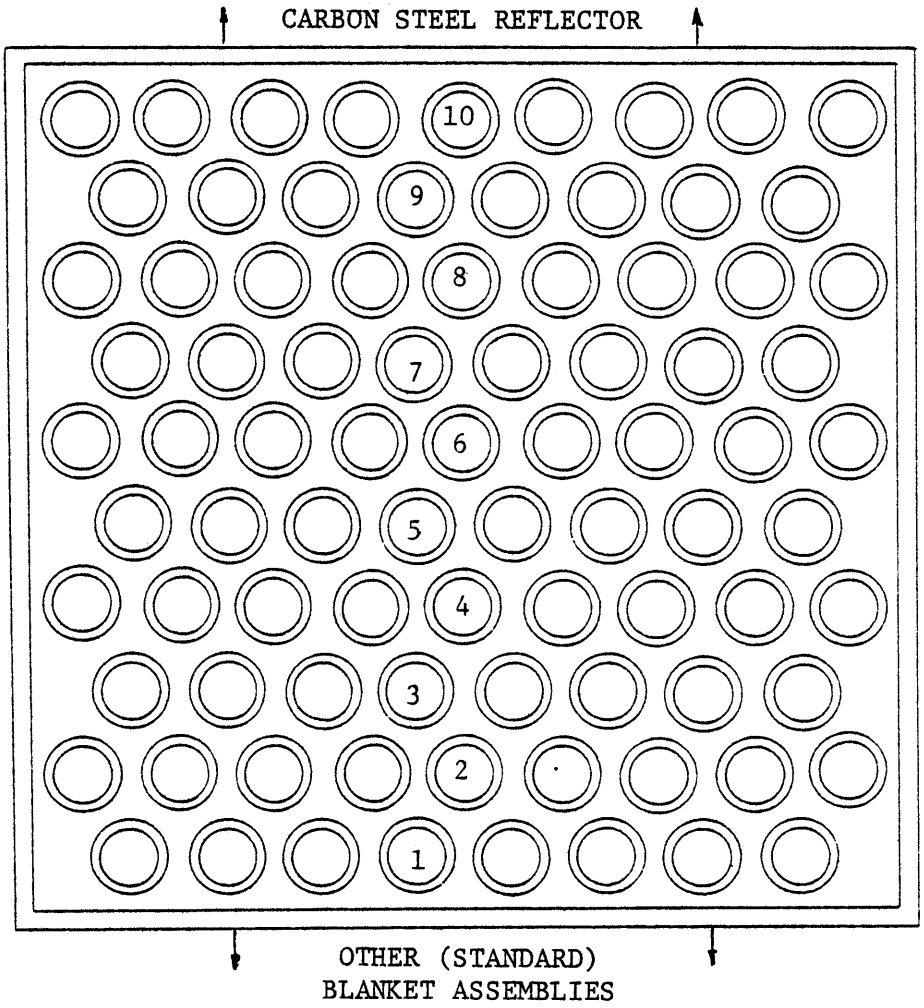

Figure 3.4 POSITION OF EXPERIMENTAL RODS

blanket-reflector boundary, it was decided to measure the U_c^{28} rate distribution in the fuel rod at position 10. For this purpose, a highly depleted uranium foil (shown as "Hi U-238") was placed at the 25-inch height at position 10. An arrow was drawn on the foil, and fuel rod No. 10 was placed in the ITS such that the arrow faced toward the reflector, perpendicular to the blanket-reflector interface. There is an uncertainty of about $\pm$ 15° in this directional positioning. After the irradiation was completed, the "Hi U-238" foil was unloaded and five mini-foils, each of 0.056 inch diameter, were punched from the foil along the arrow, numbered 1 to 5 (see Figure 3.1) and then counted. In the second run of experiments, four highly depleted uranium ring foils (shown as "ring foil") numbered 1, 2, 9 and 10 were positioned at positions 1, 2, 9 and 10, at a height of 26 inches. Each ring foil consists of six segments (see Figure 3.2), which when assembled, reproduce a disc shaped foil having an 0.431 in. diameter (and 5 mils thickness). Measuring the U_c^{28} rate of each segment gives the average radial U_c^{28} rate distribution in the fuel rod. The segments of each ring were assembled and placed in position on aluminum catcher foils (0.431 in. diameter, 1 mil thick). All foils in all experiments were sandwiched between aluminum catcher foils to prevent foil contamination by tramp activity. Figure 3.5 shows experimental fuel rod number 10, when loaded with mini and ring foils in the first and second experiments just described.

Before the uranium foils were loaded, they were counted to measure their residual background activity (see Section 3.2.3). The blanket assembly was irradiated by the MIT Reactor for 12 hours in both experiments. After allowing one hour cooling time, the blanket assembly experimental cart was withdrawn and the experimental fuel rods were unloaded. Counting

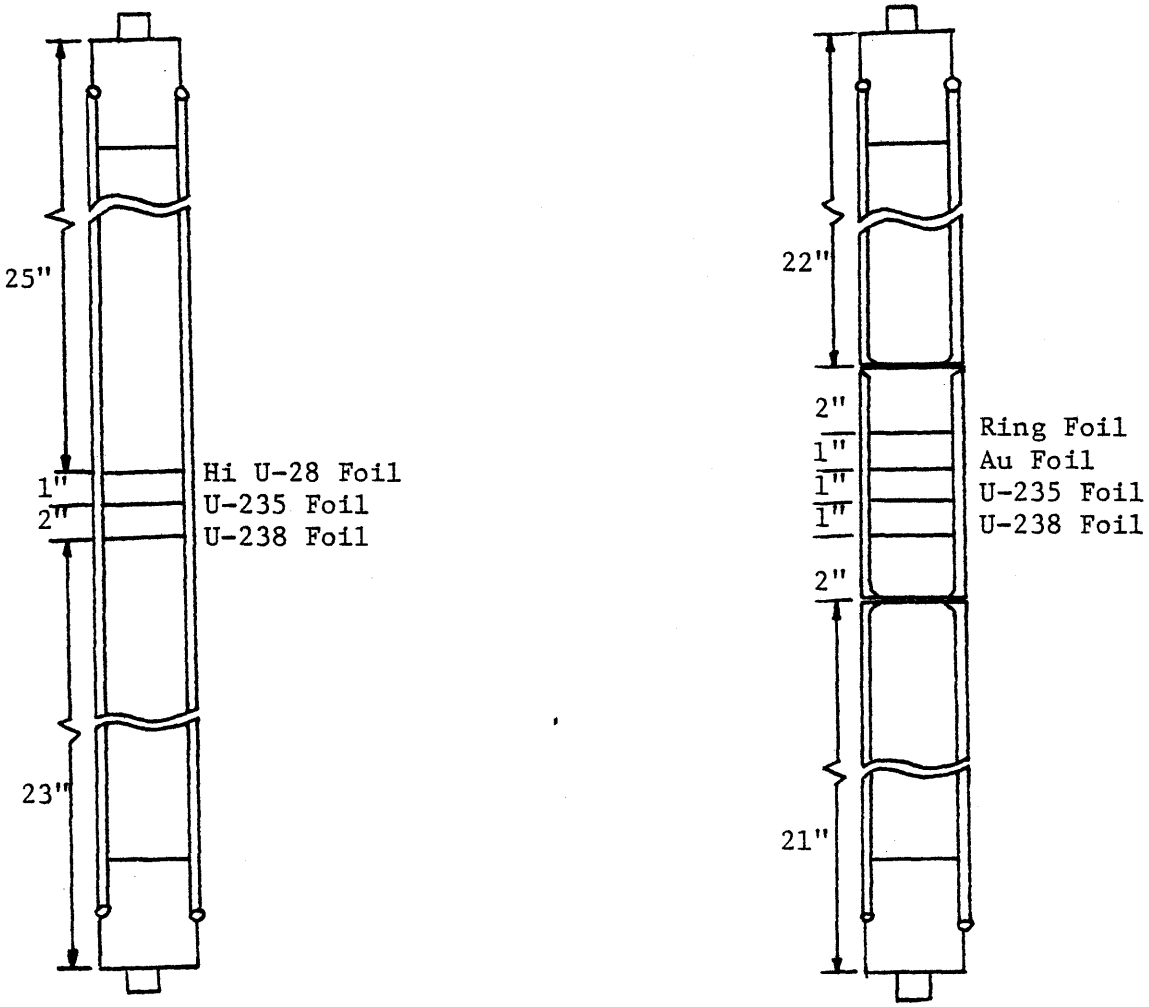

Figure 3.5 FOIL POSITIONS IN FUEL ROD NO. 10

the first set of foils (U-235 foils counted first) was started after four hours total cooling time.

3.2.3 Foil Counting Techniques

3.2.3.1 Counting Equipment

A well-type scintillation counting system was used to measure the gamma activities of the irradiated foils, as shown in Figure 3.6. The well type thallium-activated, sodium iodide crystal was used because of its intrinsically high efficiency. This 2-inch-diameter crystal, with photomultiplier tube and preamplifier, is surrounded by 3 inches of iron shielding and 8 inches of lead shielding to maintain a very low background. The system is located in a room having its own independent electrical supply circuit in order to minimize the effects of background electrical noise on the counting system. The high voltage supply for the photomultiplier tube and the low voltage for the preamplifier were provided by the voltage supply unit, Hewlett-Packard Model 5551A. A single channel pulse height analyzer was used: Hewlett-Packard Model HP-5201L scaler timer. The scaler-timer unit had both preset time or count options, and a 6-digit readout.

The radioisotopes Co^{57}, Mn^{54} and Na^{22} were used to calibrate the counting system. Before each foil counting session, the calibration on the counting system was checked to ensure that there had been no drift in voltage.

3.2.3.2 U-235 Foil Counting

The U-235 fission reaction rate was found by measuring the activity of U-235 fission products. The mean half-life of U-235 fission products

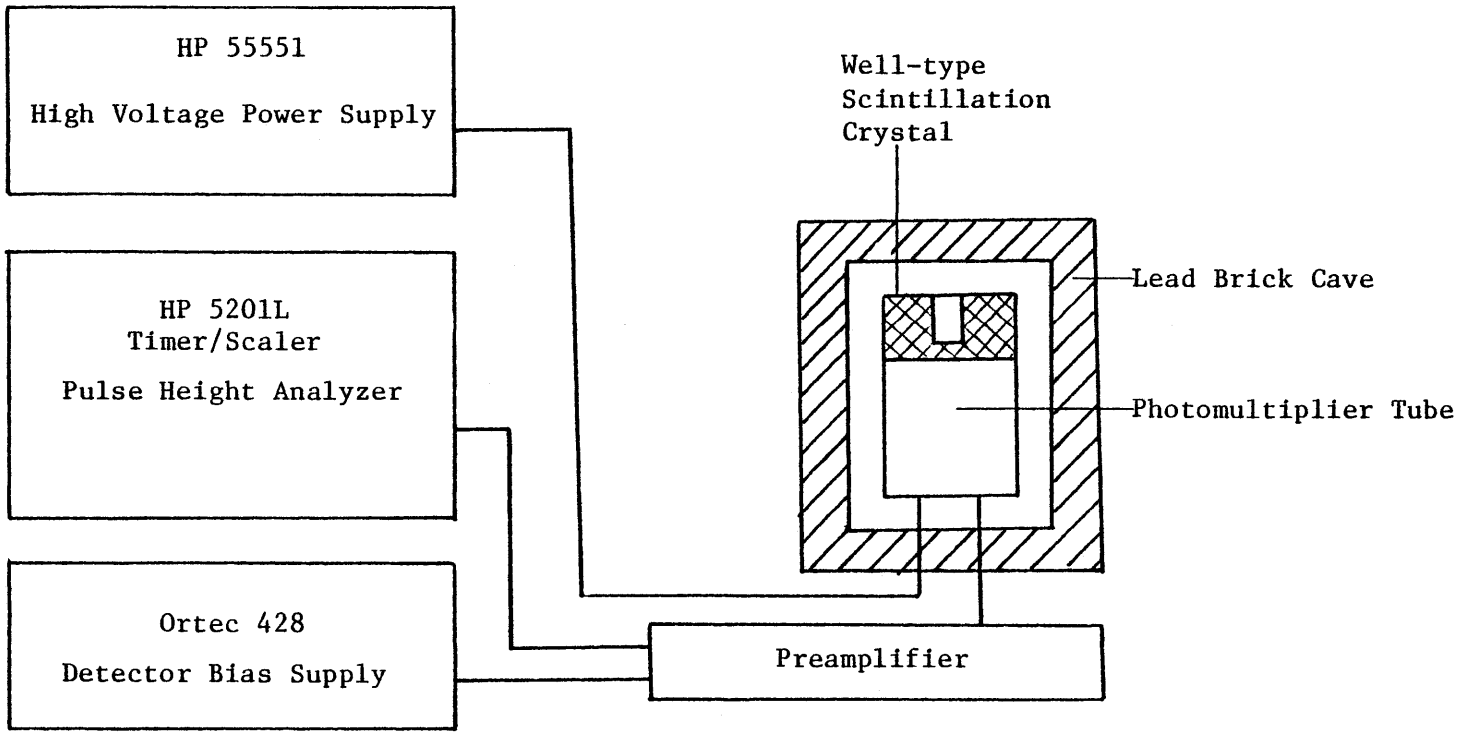

Figure 3.6 COUNTING SYSTEM SCHEMATIC

is about 2.5 hours and changes with time. The technique used for gamma counting U-235 fission product activity was to set on infinite window (i.e. integral setting) with a baseline corresponding to 0.72 Mev. This particular scheme has been used with good results in the past at MIT (Ref. L3). The complication involved in the counting technique used is that the effective fission product activity half-life is time dependent. This was resolved by two different approaches, as applied in the first and second set of experiments. In the first experiment, one foil was counted five times throughout the counting session to monitor the fission product decay and to provide the proper normalization for the measured data. In the second experiment, the U-235 foils were counted twice: in forward and reverse order, keeping the same time interval between measurements. The average activity of each foil, provides an estimate of the foil activity present at the midpoint of the counting sequence. The 23.5 minute half-life of the U-239 activity formed in the U-235 foils (which contained 6.83 w/o U-238) was permitted to decay to an almost negligible level before fission product activity counting was commenced. This required a foil cooling period of about four hours. Otherwise, the 1.21 Mev beta particle emitted by U-239 can introduce bremsstrahlung radiation into the fission product activity measurements. In addition, the 0.72 Mev baseline setting eliminates the bremsstrahlung radiation contribution associated with the 0.72 Mev beta particle emitted by Np-239. The fission product counting was started about four hours after completion of blanket irradiation. All U-235 foils were counted for 10 minutes. The typical residual background and uncorrected count rates (the counts as read from the counter display) are listed in Table 3.2.

TABLE 3.2

Typical Values of Foil Activities

Foil	Product Nuclide	$T_{1/2}$	$E\gamma$ (Mev)	Typical Residual Counts	Typical Uncorrected Counts
Au^{197}	Au^{197}	2.8 days	0.412	-	5000 (10 min)
U^{25}	Gross Fission Product	~2.5 hrs.	$\geq$0.72	200 (2 min)	16000 (2 min)
U^{28} (Depleted Uranium)	Np^{239}	2.33 days	0.103	14000 (2 min)	80000 (2 min)
Mini-foil				400 (500 sec)	7000 (500 sec)
Ring-foil					
Segment: #1				700 (2 min)	4000 (2 min)
#2				1400 (2 min)	9000 (2 min)
#3				2200 (2 min)	15000 (2 min)
#4				2900 (2 min)	21000 (2 min)
#5				3700 (2 min)	27000 (2 min)
#6				4300 (2 min)	35000 (2 min)

3.2.3.3 U-238 Foil Counting

U-238 foils (depleted uranium foils and highly-depleted uranium minifoils and ring foils) were used to measure the U-238 capture reaction rate, $U^{238}(n,\gamma)$. The U-238 neutron capture rate was obtained by counting the Np-239 decay activities of the irradiated depleted uranium foils, which arise from the sequence:

$$U^{238} + n \rightarrow U^{239} \xrightarrow[23\ min]{\beta^-} Np^{239} \xrightarrow[2.333\ days]{\beta^-} Pu^{239}$$

The "103-kev" peak in the γ-ray and x-ray spectrum of the Np^{239} was counted. This characteristic composite peak is due to the 106 kev γ-ray of Np^{239} and the 99-kev and 100-kev x-rays of Pu^{239} from the internal conversion of higher energy γ-rays of Np^{239}. The lower and upper limits chosen for the analyzer window were 85 kev and 125 kev, respectively. The Np^{239} counting was started about 24 hours after irradiation to allow for the decay of fission product activity to the point where the Compton background would not obscure the low energy Np^{239} gammas. All U-238 foils were counted for 2 minutes, except for the minifoils which were counted for 500 seconds. Table 3.2 lists the typical residual background and uncorrected counts of the U-238 foils.

3.2.3.4 Au^{197} Foil Counting

The Au^{197} neutron capture reaction rate, $Au^{197}(n,\gamma)Au^{198}$, was obtained by counting the Au^{198} decay activity of the irradiated gold foils. The Au^{198} decays with a half life of 2.8 days and emission of a characteristic gamma ray with energy equal to 412 kev. The lower and upper levels of the analyzer window were set at 360 kev and 460 kev, respectively.

All Au foils were counted for 10 minutes. Typical uncorrected counts for Au^{197} foils are listed in Table 3.2.

3.2.4 Corrected Activities

Since only the normalized relative distribution of reaction rates through the ITS is desired, there is no need to find the absolute activity of each foil. Thus, in each set of foil counting data (e.g. U-235 foils 1 through 10), the time when the counting of the first foil started was chosen as zero for that set, and the decay time was only measured from that point. The uncorrected counts were then corrected for room background and residual foil background activities, for foil weights and the decay time, according to the following equation:

$$A = \frac{C - B}{w} e^{\lambda t_d}$$

where

A = corrected activity (in counts/min-mg)

C = number of counts read by the counter (uncorrected counts)

B = post irradiation foil residual and room background

λ = decay constant of the product radionuclide

w = weight of foil

t_d = decay time = time interval between the beginning of foil counting and the reference time (start of counting session)

B was found from the following relation:

$$B = B' \cdot \frac{B_R}{B'_R}$$

where B' = pre irradiation foil residual and room background, and

B_R and B'_R are residual and room background of a reference foil, which was not irradiated, counted the same days as B and B' were counted.

Since the counting interval for all foils in a given set was the same, there was no need to correct for decay during the counting period.

3.3 THE EXPERIMENTAL RESULTS

The results of the two sets of experiments performed are plotted in the form of U^{235} fission rate, U^{238} capture rate and Au^{197} absorption rate distributions in Figures 3.7 through 3.13. Since the relative behavior of the sets of foil activities near the ITS-Reflector Interface is desired, each set was normalized to the corresponding foil activity at position #2 (see Figure 3.4) sufficiently deep within the blanket to be free of interface-induced perturbations. In Figures 3.7 through 3.11, positions $x = 0.0$ and $x = 15.0$ indicate Blanket-ITS and ITS-Reflector interfaces respectively.

The uncertainty in the U_f^{25} and U_c^{28} measurements was estimated by the following method. If we have two separate data points of a quantity A, measured in two separate experiments, indicated by $A_i^{(1)}$ and $A_i^{(2)}$ (in this case i = 1, 2,....,10); then the average value of these two measurements is defined as:

$$\bar{A}_i = 1/2\left[A_i^{(1)} + fA_i^{(2)}\right] .$$

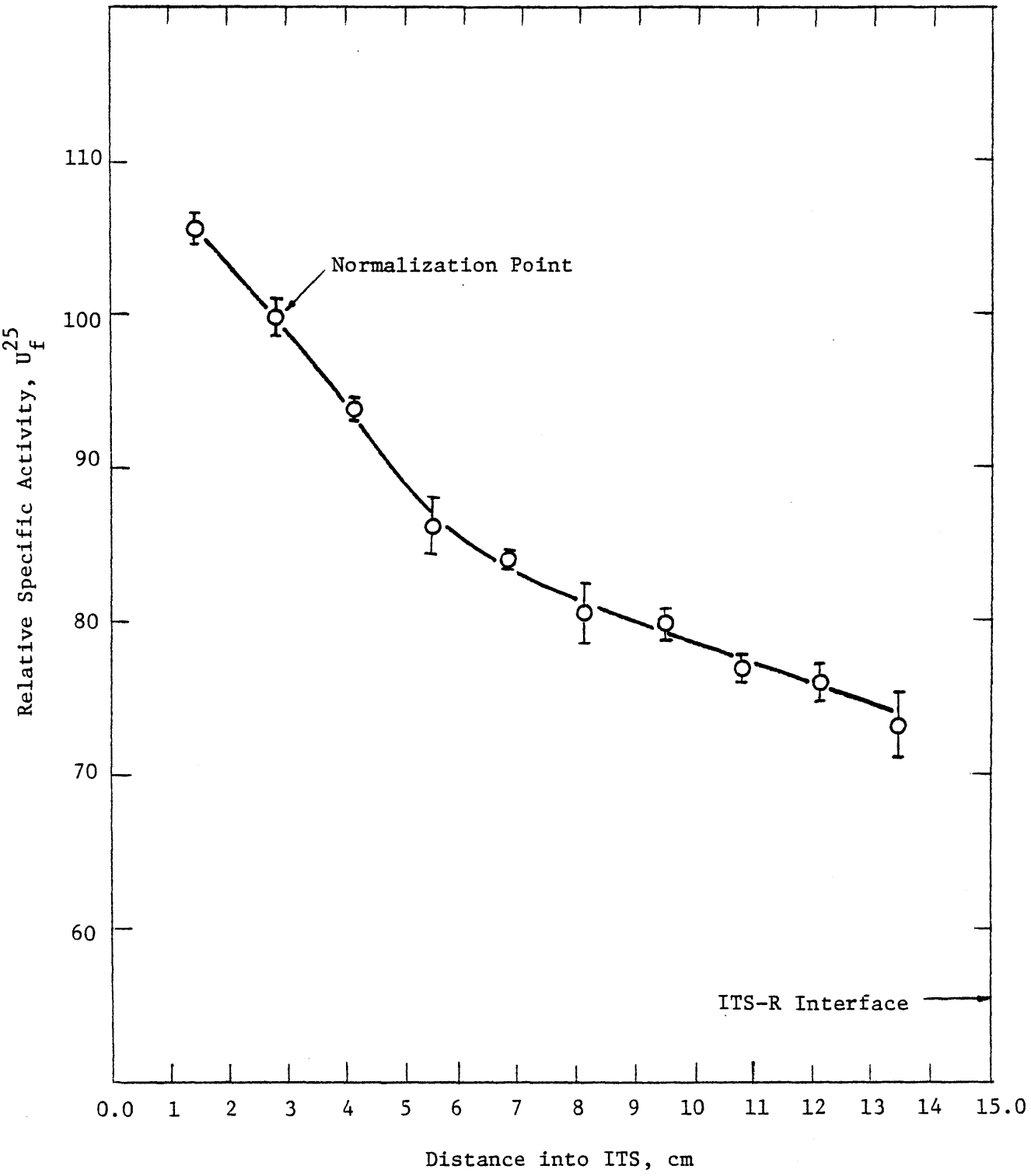

Figure 3.7 NORMALIZED U_f^{25} DISTRIBUTION IN ITS, EXPERIMENT #1

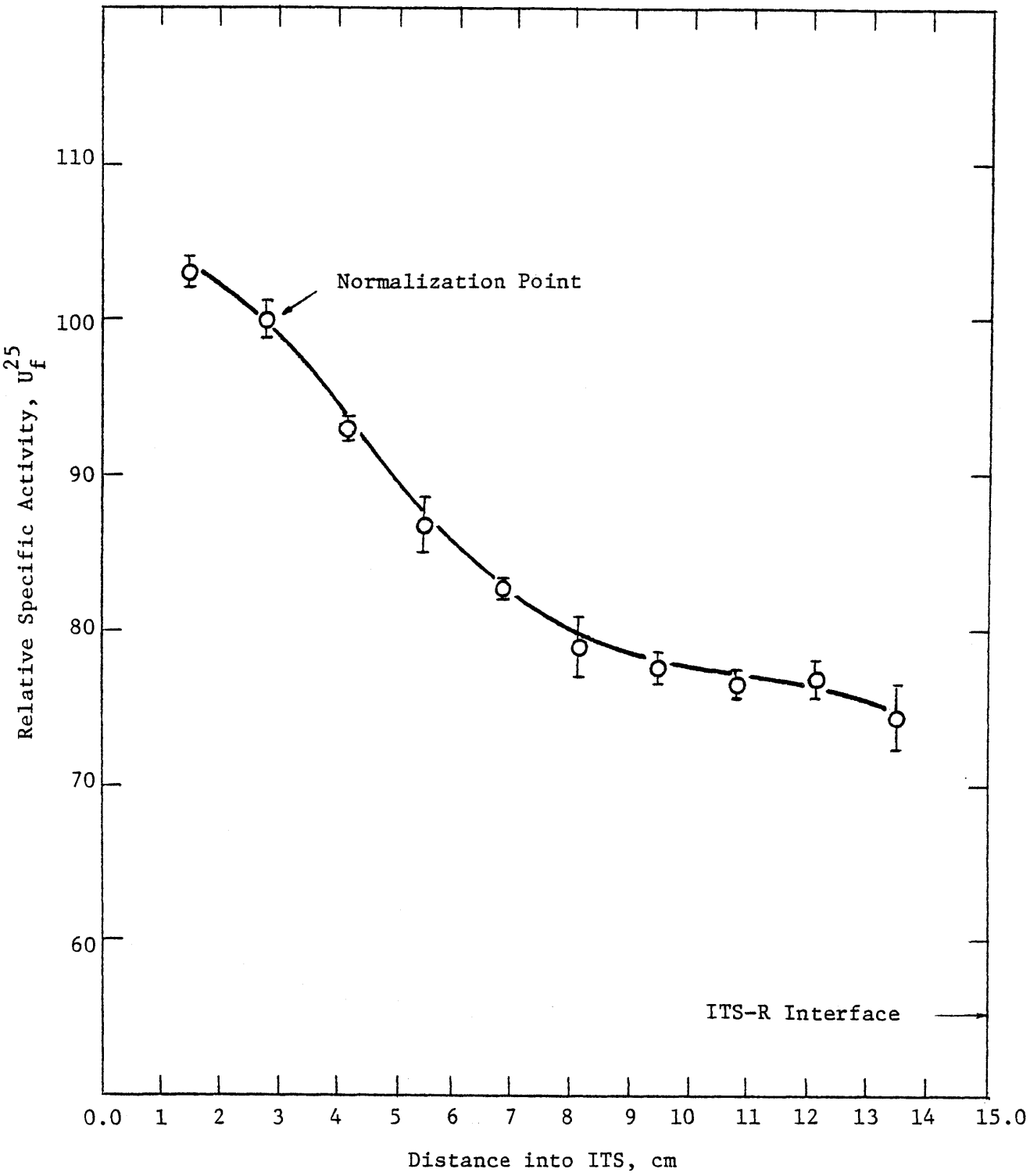

Figure 3.8 NORMALIZED U_f^{25} DISTRIBUTION IN ITS EXPERIMENT #2

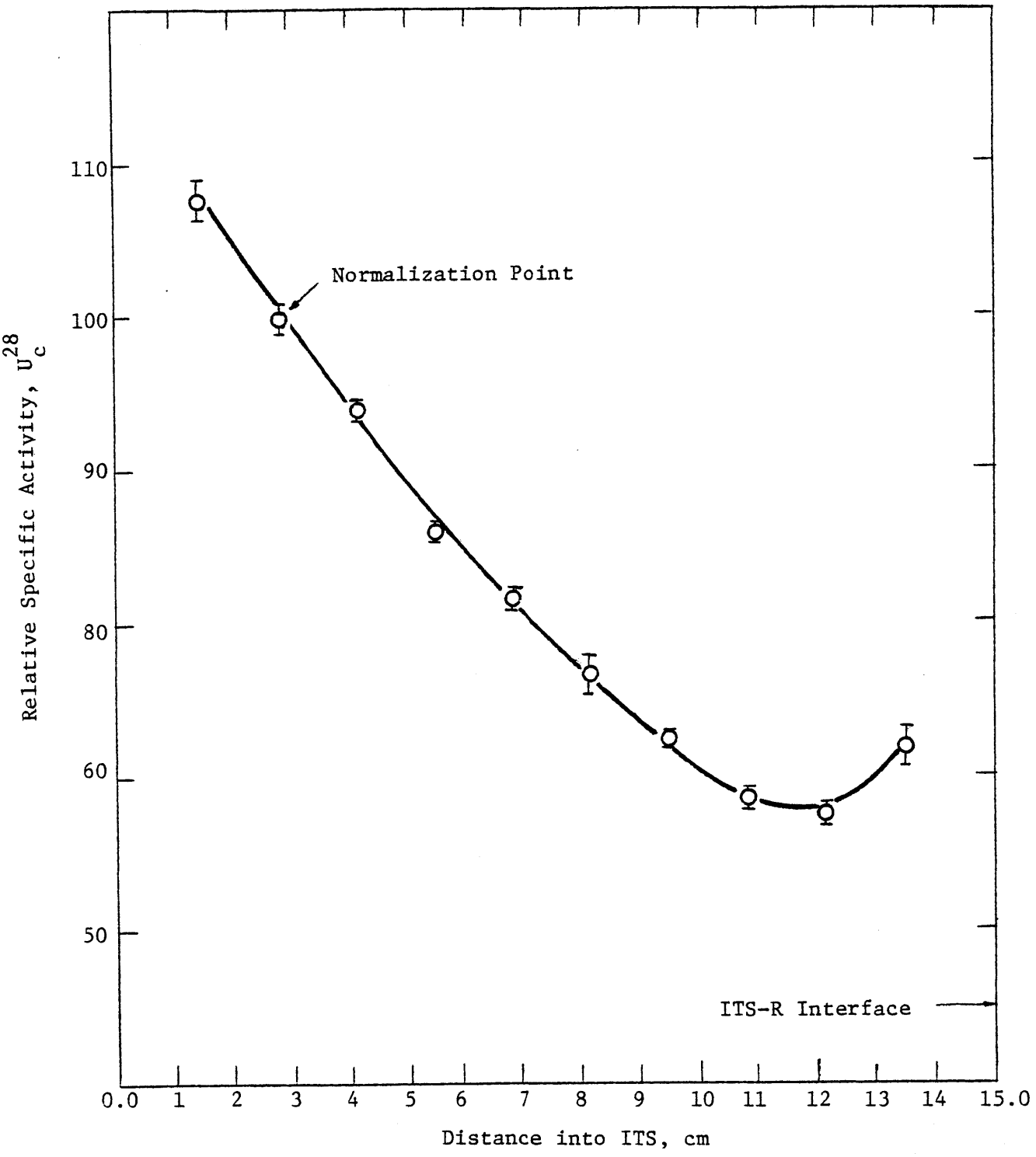

Figure 3.9 NORMALIZED U_c^{28} DISTRIBUTION IN ITS, EXPERIMENT #1

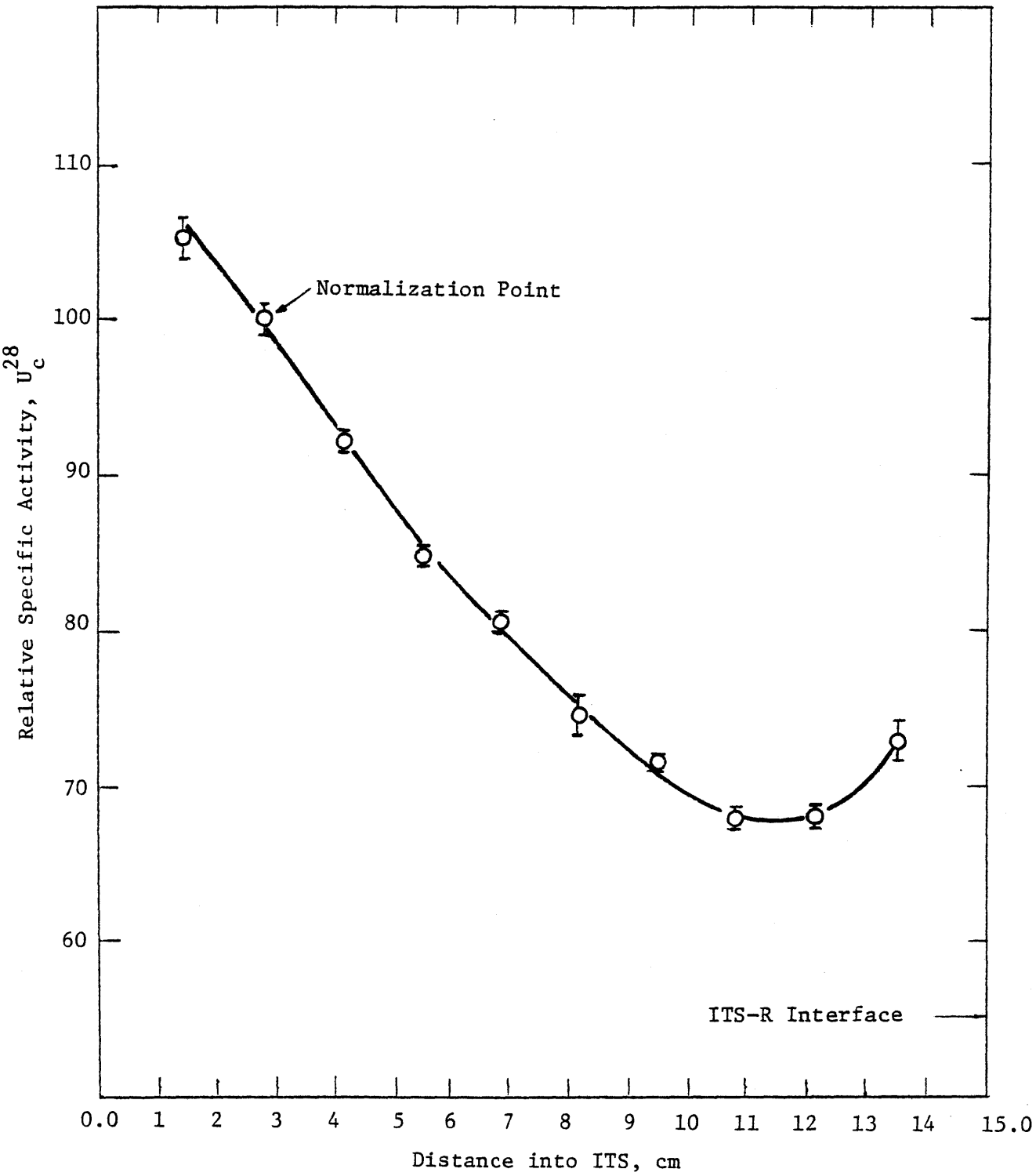

Figure 3.10 NORMALIZED U_c^{25} DISTRIBUTION IN ITS, EXPERIMENT #2

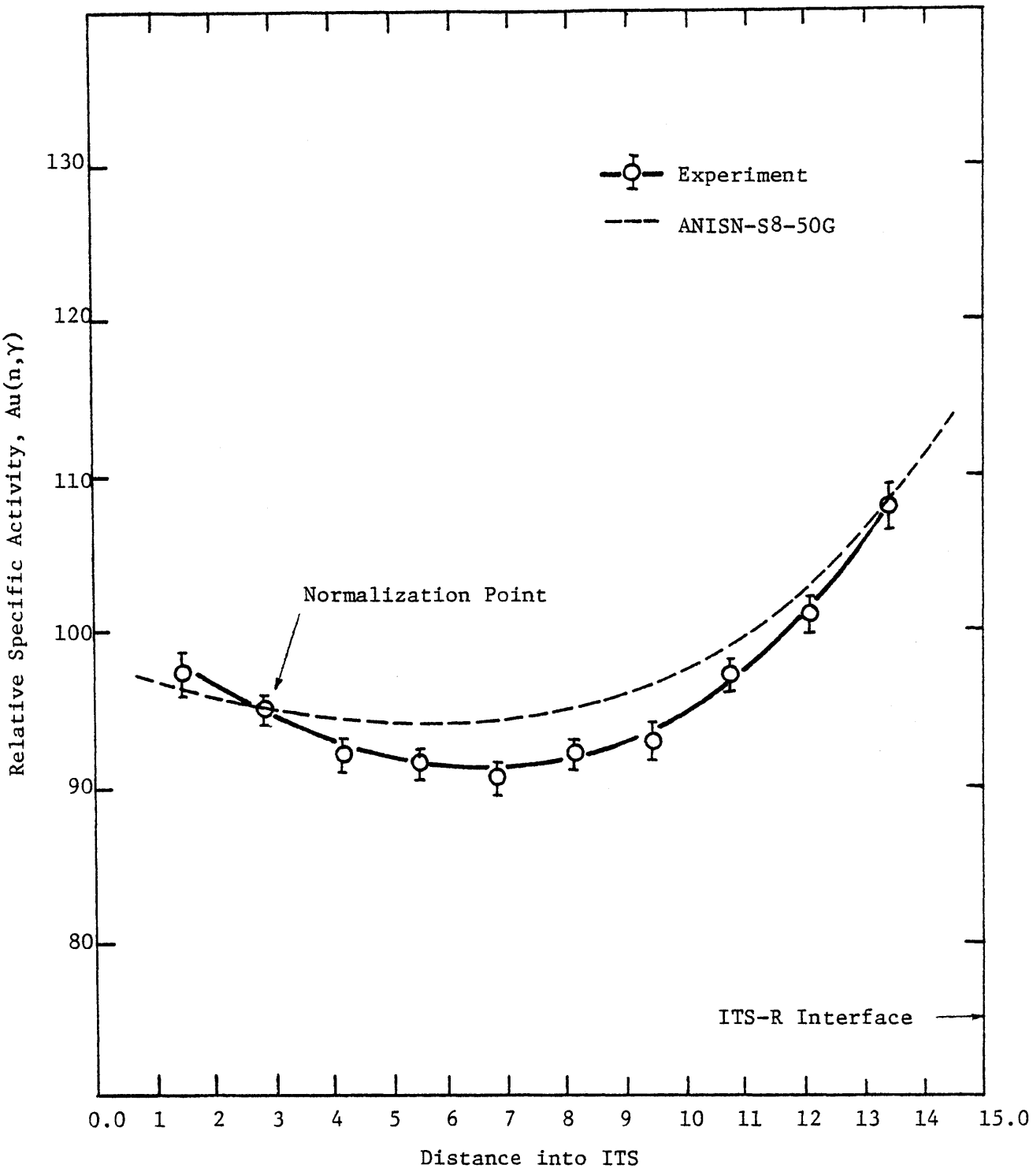

Figure 3.11 NORMALIZED Au(n,γ) ACTIVITY AS A FUNCTION OF DISTANCE INTO ITS

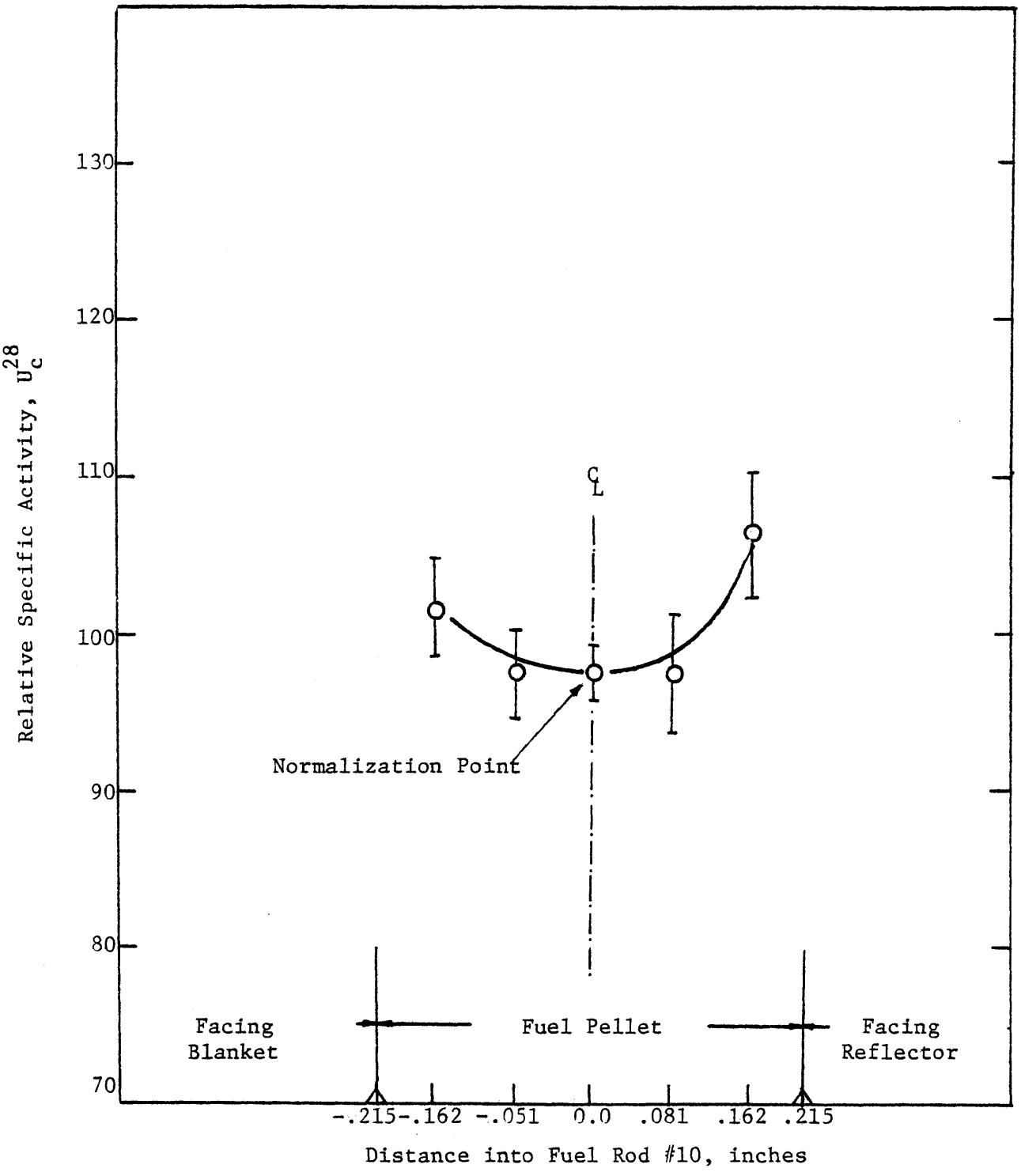

Figure 3.12 NORMALIZED U_c^{28} DISTRIBUTION THROUGH FUEL ROD #10, MINIFOIL RESULTS

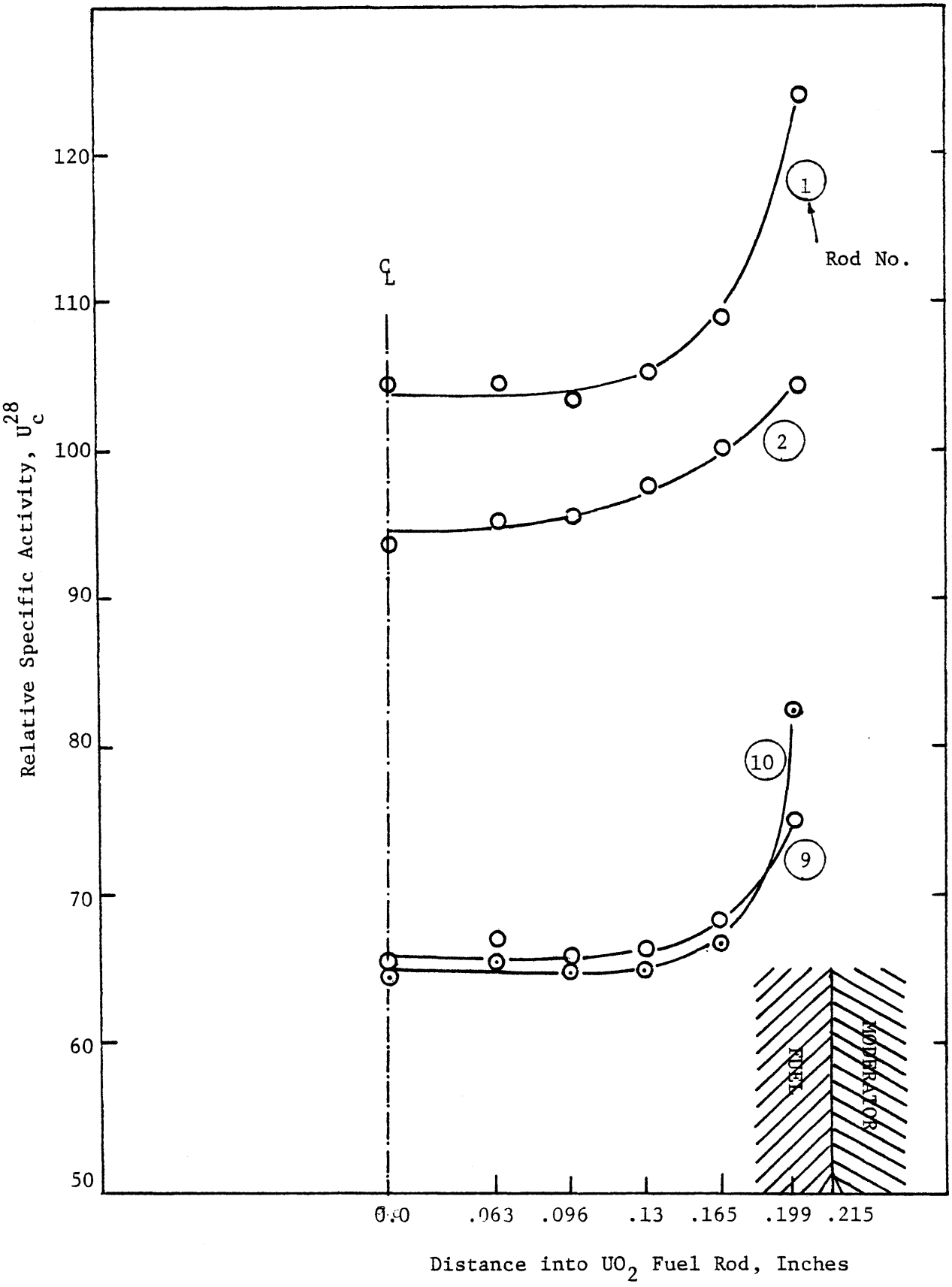

Figure 3.13 AVERAGE RADIAL DISTRIBUTION OF THE U-238 CAPTURE INSIDE UO_2 FUEL PINS, RING FOIL RESULTS

The factor f is found through minimizing the quantity

$$V = \sum_{i=1}^{10} \left[fA_i^{(2)} - A_i^{(1)} \right]^2 .$$

Setting $\frac{\partial V}{\partial f} = 0$ leads to $\sum_i 2A_i^{(2)} \left[fA_i^{(2)} - A_i^{(1)} \right] = 0$, hence

$$f = \frac{\sum_i A_i^{(1)} A_i^{(2)}}{\sum_i \left[A_i^{(2)} \right]^2}$$

From the average value $\bar{A}_i$, we can find the error contributed to each measurement through the formula SDM = σt, where

$$\sigma_i^2 = \frac{\left[A_i^{(1)} - \bar{A}_i \right]^2 + \left[fA_i^{(2)} - \bar{A}_i \right]^2}{2}$$

and

t = 1.86 (the student's t factor for 2)

For the U_f^{25} and U_c^{28} data sets it was found that $f^{(25)} = 1.014$ and $f^{(28)} = 1.0095$, and the calculated SDM values ranged between 0.8% to 3.0% and 0.6% to 2.1% respectively. The foils of each set are at the same height within $\pm$ 0.25 in. Since the foils are placed at the mid-height of the blanket assembly, this deviation in height positioning leads to negligible error, because the flux varies smoothly with height at the mid-height (flux shape is cosine with its peak occuring at mid-height). The error bars in the Au^{197} absorption distribution (Figure 3.11) only include statistical error, ranging between 1.5% and 4.0%. (The previous method could not be applied, since only one data set was available.) Figure 3.12 shows the U_c^{28} rate of the mini-foils positioned in fuel rod #10 (see Figures 3.1 and 3.4). The mini-foil

activities are normalized to the activity in the center mini-foil. The results confirm the expectation that the U_c^{28} rate is lower at the central part of the fuel due to shielding by the peripheral region of the fuel rod. The data also shows that the U_c^{28} rate on the side of the fuel rod facing the ITS-Reflector interface is higher than the U_c^{28} rate at the opposite inboard side, which is in agreement with the whole-foil U_c^{28} distribution near the interface (see Figures 3.9 and 3.10). The uncertainty in the mini-foil activity measurement is attributable to statistical error and positioning error. The statistical error is 1.4%. There are two types of positioning error; error due to inaccurate positioning during the foil punching process and error due to the estimated $\pm$ 15° deviation in rotational alignment. In the first category, the positioning error is at most $\pm$ 0.25 d, where d is the distance between two adjacent mini-foils (d = 0.18 inch). Using a linear interpolation between two adjacent activities, the error contribution is found to be $\pm$ 2.2%. In the second instance, the maximum error would be for the case when the neutrons are flowing in the direction normal to the interface. The 15° deviation would be equivalent to a mispositioning of $\pm$ d (1 - cos 15°). This leads to an error of $\pm$ 0.3%. Thus the overall error ranges between 1.7% and 3.8%.

Figure 3.13 shows the U_c^{28} rate of the ring foil sets in four fuel rods. The ring foil activities were normalized with respect to the average activity of ring foils installed in fuel rod #2. Since in Figures 3.9 and 3.10 the same normalization point was chosen, this makes the comparison more clear. When considered as a single composite foil, the appropriately averaged activity of each set should follow the same trend as the normal one-piece U_c^{28} foils do at the boundary in Figures 3.9 and 3.10. Also, if we calculate the percentage rise in U_c^{28} near the surface of the fuel rod

compared to its center, from the equation

$$\Delta\% = \frac{\text{ring foil \#6 activity - average of ring foils \#1, 2, 3 activity}}{\text{average of ring foils \#1, 2, 3 activity}}$$

we find that $\Delta_1 = 19.0\%$, $\Delta_2 = 10.4\%$, $\Delta_9 = 19.2\%$ and $\Delta_{10} = 27.6\%$, where the indices indicate the location of each set of ring foils. Δ_1 and Δ_{10} are higher, as would be expected for fuel rods placed near the interfaces. Also, Δ_{10} is the largest value observed, which again confirms the expectation that the boundary effect at the ITS Reflector interface will be more pronounced.

The error contributions to ring foil activity are geometrical and statistical errors. The statistical error ranges from 0.6% to 2%. The geometrical error refers to off center positioning during installation of the ring foils in the experimental rod. Even though the ring foils were checked after irradiation and found to be in position, a mispositioning of as much as $\pm \frac{d}{4}$ is assumed (d is the difference between any two adjacent ring average radii, namely 0.023 inch). Using interpolation between ring foil activities, we get the corresponding error for each ring foil due to $\pm \frac{d}{4}$ off-centering. The overall error ranges between 1.2% and 5.5%.

3.4 SUMMARY AND CONCLUSION

By placing the ITS at the Blanket-Reflector boundary, the U_c^{28}, U_f^{25} and Au^{198} activity distributions along the line normal to the interface was measured using uranium and gold foils. The results show a buildup in U_c^{28} near the interface, a trend that was expected. U_f^{25} and Au^{198} activities follow the same trend as with state-of-the-art calculations, in contrast with U_c^{28} activity near the interface, which is not reproduced

by such calculations. The buildup in U_c^{28} starts at foil #8 (4.14 cm from the interface); U_c^{28} in foil #10 (1.46 cm from the interface) is elevated 8% relative to foil #9, however, the U_c^{28} in foil #10 is elevated 16.7% relative to the extrapolated value of U_c^{28} at the same position when there is no interfacial effect. The mini-foil and ring-foil U_c^{28} activities all confirm the interfacial effect, and the ring-foil results for the foil at the position closest to the interface (1.46 cm) shows that the U_c^{28} buildup averaged over the surface of this fuel pin is 17% higher than the average buildup of U_c^{28} over the entire fuel rod. This raises the question as to whether, even though tolerable on a whole-rod basis, highly localized surface capture rates (hence plutonium production, and eventually fission) on the interface side of a pin may cause thermal/hydraulic or mechanical design problems.

CHAPTER 4

ANALYSIS OF ITS EXPERIMENTAL RESULTS

4.1 INTRODUCTION

In this chapter ITS experimental results will be compared with state-of-the-art calculations, and with previous relevant experimental data measured at MIT by Leung (L3), Kadiroglu (K2) and Medeiros (M2).

The state-of-the-art calculations involve use of the ANISN and 2DB codes. Emphasis will be on identification of the factors responsible for the deviation between the experimental and calculational results. It will be shown that changing the number of energy groups and quadrature order does not change the overall shape of the calculated foil activity distributions, but rather shifts the curves up or down. Therefore, the cause of discrepancy near the ITS-Reflector interface is attributed to the use of infinite medium cross sections near the boundaries: this factor is examined further in Chapter 5.

In the next section we compare ITS results with the experiments reported in References (L3), (K2), (M2). We will see that the interfacial effect is more pronounced in these other instances. One of the factors which may cause this difference is the different unit cell structure, which affects the self-shielding factor, and hence the U-238 capture rate; another is the effect of the neutron slowing down in the fuel (UO_2 pellets). These two factors are studied using the SPHINX code, which is described briefly in the next section. Discussion of the effect of the other factors is deferred until Chapter 5.

4.2 COMPARISON OF THE ITS EXPERIMENTAL RESULTS WITH STATE-OF-THE-ART CALCULATIONS

In order to compare the results of the ITS experiments with state-of-the-art calculations an ANISN S8 50-group and a 2DB 4-group run were made, simulating the same geometric arrangement and regional composition (nuclide number densities) used in the experiments. For ANISN calculations a 50-group cross section library was used which contained self-shielded isotopes appropriately shielded for the blanket region. The cross sections had been generated by self shielding a LIB-IV 50-group set for the specific geometry and elemental composition of the blanket regions using the SPHINX code. This cross section set was then collapsed into a 4-group set to be used in 2DB 4-group calculations. Figures 4.1 to 4.3 show the average of the two ITS experimental results (see Section 3.3 for details) along with the computer results for U_f^{25}, U_c^{28} and U_c^{28}/U_c^{25}. In Table 4.1 the averaged experimental values of these quantities are listed. Figures 4.1 and 4.2 show that the general trends of both the experiments and the ANISN calculations are similar for the U_c^{25} distribution, but for the U_c^{28} distribution, and consequently the U_c^{28}/U_c^{25} distribution, the trend near the ITS Reflector interface differs for the experiments and the calculations. This indicates that there is an effect which is influential only on U_c^{28} near the interface, and which is not accounted for in the state-of-the-art calculations. The experimental value of U_c^{28} rises about 8% near the interface relative to the computer results, which show a steady decrease. The rise in U_c^{28} starts at fuel rod number 9 (2.8 cm from the ITS-R interface: in the second "row" of fuel pins). That is, in this case the interfacial effect dies out within 2.8 cm of the interface.

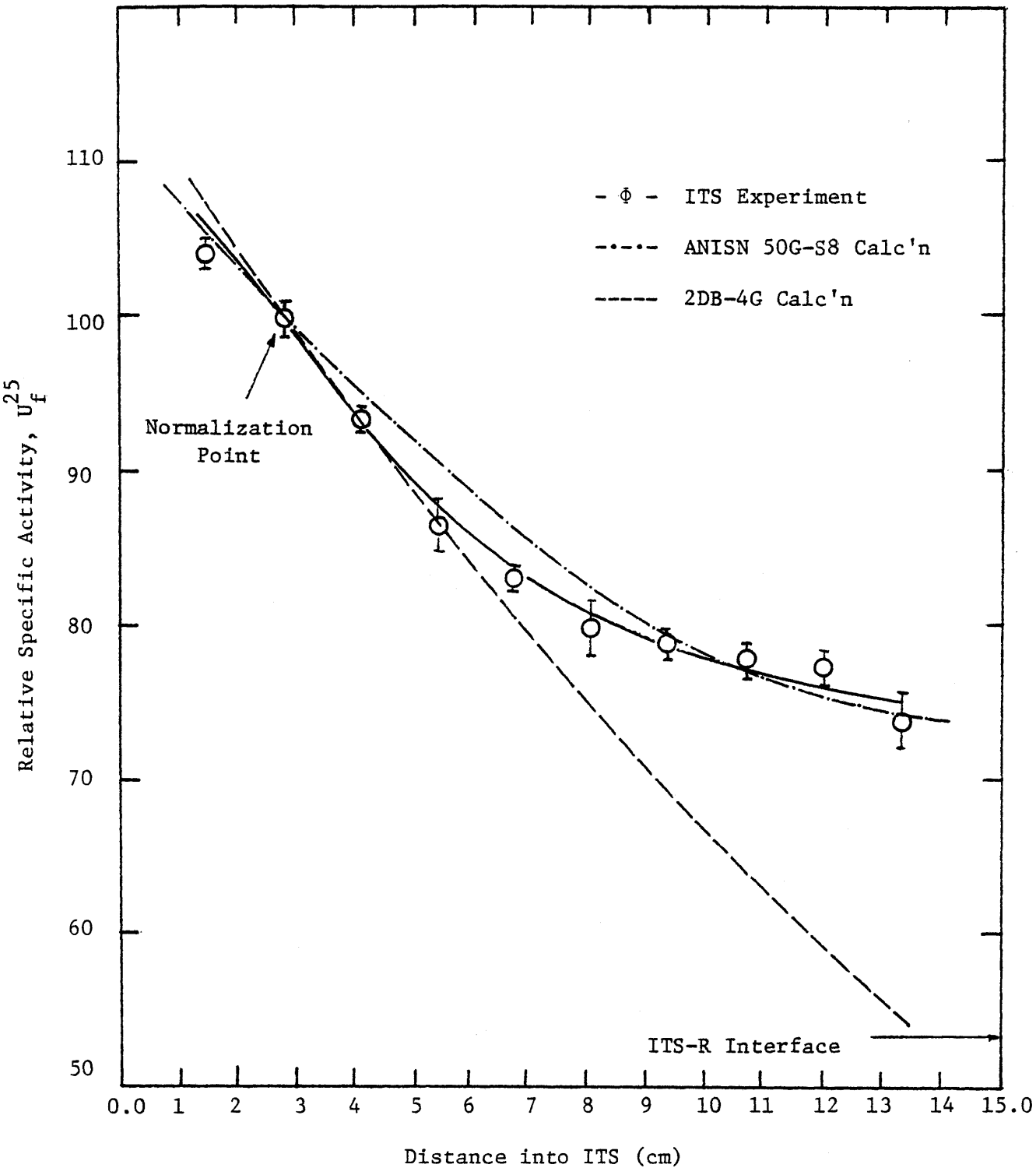

Fig. 4.1 NORMALIZED AVERAGE EXPERIMENTAL U_f^{25} TRAVERSE THROUGH THE ITS

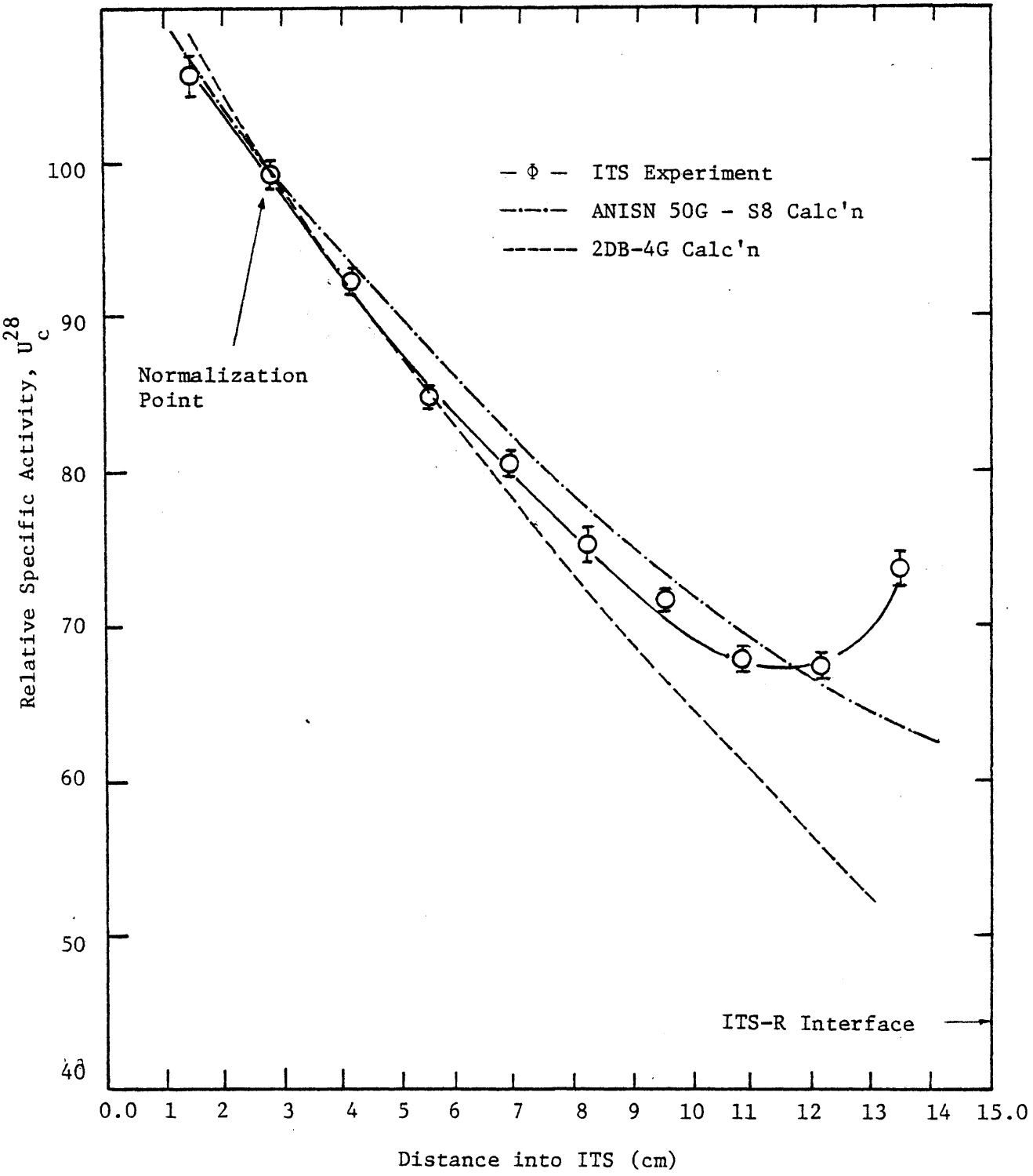

Fig. 4.2 NORMALIZED AVERAGE EXPERIMENTAL U_c^{28} TRAVERSE THROUGH THE ITS

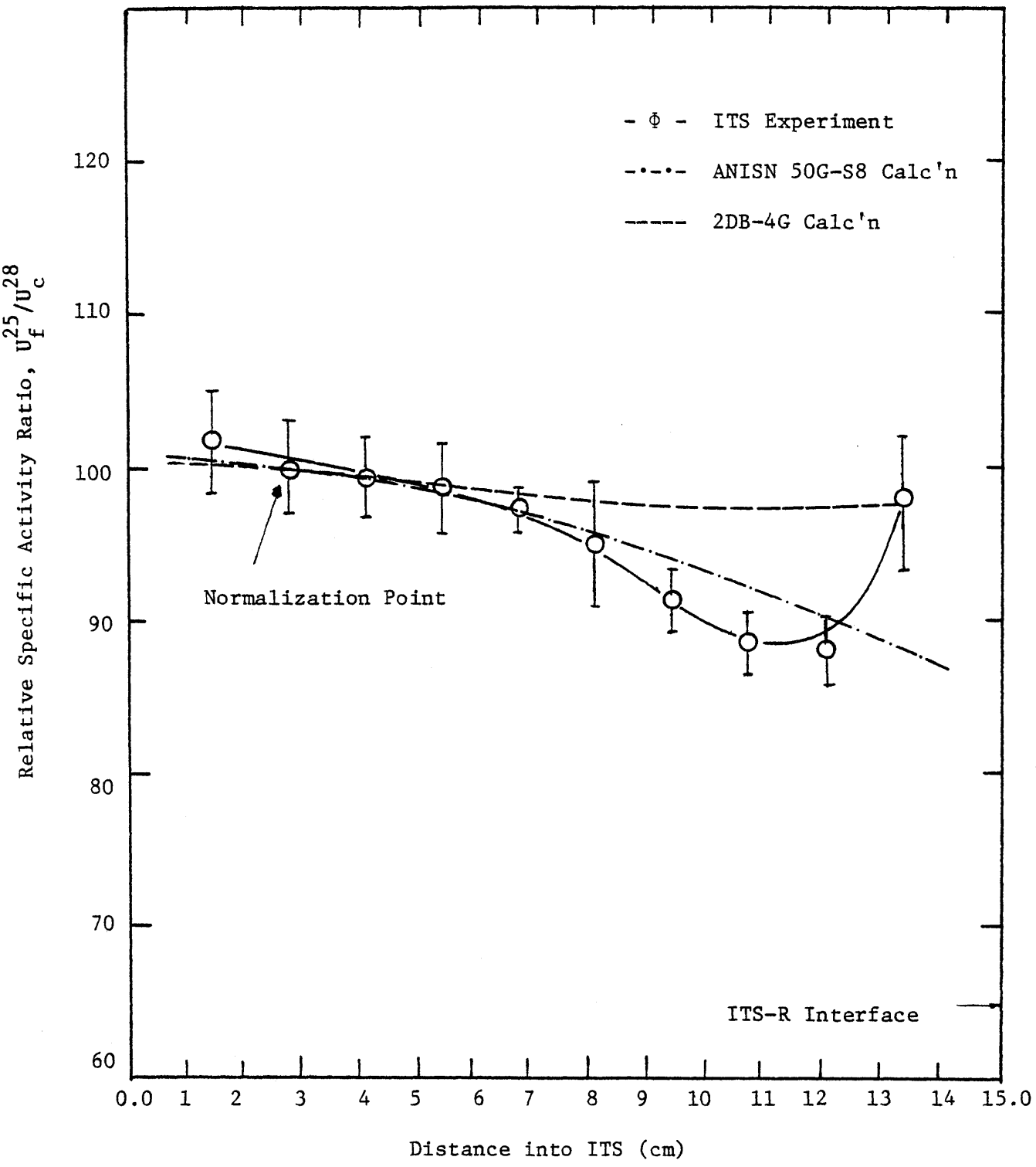

Fig. 4.3 NORMALIZED AVERAGE EXPERIMENTAL U_f^{25}/U_c^{28} TRAVERSE THROUGH THE ITS

TABLE 4.1

AVERAGE NORMALIZED EXPERIMENTAL VALUES OF U_f^{25}, U_c^{28}, U_c^{28}/U_f^{25}

Position #	Distance Into ITS (cm)	U_f^{25}	U_c^{28}	U_c^{28}/U_f^{25}
1	1.5	104.3 ± 2	106.5 ± 1.8	102. ± 3.5
2	2.8	100. ± 2	100. ± 1.3	100. ± 3.4
3	4.2	93.5 ± 1.3	93. ± 0.9	99.5 ± 2.4
4	5.5	86.5 ± 2.2	85.4 ± 0.6	98.7 ± 3.2
5	6.8	83.3 ± 0.7	81.1 ± 0.6	97.4 ± 1.5
6	8.2	79.8 ± 2.2	75.7 ± 1.3	94.9 ± 4.5
7	9.5	79. ± 1.4	72.1 ± 0.4	91.3 ± 2.1
8	10.9	77. ± 1.2	68.2 ± 0.5	88.6 ± 2.1
9	12.2	76.9 ± 1.6	67.6 ± 0.5	87.9 ± 2.6
10	13.6	74.5 ± 2.2	72.4 ± 1.5	97.8 ± 4.9

There is also a substantial difference between the ANISN and 2DB results, which is due to their different group structure (i.e. 50G for ANISN and 4G for 2DB) and also due to inherent differences between these two codes. The ANISN code is a one-dimensional transport (S_N) code which does not simulate two (or three) dimensional cases in a precise manner (although a transverse buckling was used); and the 2DB code is a two-dimensional diffusion code, which would be expected to have some difficulty near the interface.

The other macro-size traverses are less informative. The trend of the U_c^{28}/U_c^{25} results in Figure 4.3 is explained by reference to the U_c^{28} distribution (Figure 4.2). Figure 3.11 shows that both experimental and ANISN S8 50-group results show the same general trend for the Au^{198} activity. Hence the gold data offer very little insight not provided by the U-235.

The neutron flux distribution inside a fuel rod has been derived and approximated (T1) as:

$$\phi(r) \cong A_o + A_1 \left(\frac{r}{a}\right)^{8/3} \tag{4.1}$$

where a is the radius of the fuel rod. The ring foil activities were examined to see if they could be fit to Equation (4.1) for proper choice of A_o and A_1. It was found that only the ring foils in fuel rod #2 (see Figure 3.4) fit the above equation (for $A_0 = 93.8$ and $A_1 = 13.7$). For the other sets it was noticed that the experimental results show a higher rate of increase in their outer rings than the above equation permits. It is interesting to note that the interfacial effect due to the ITS boundaries is negligible at fuel rod #2 while it is strongest at

fuel rod #10. This may explain the discrepancy observed between the experimental data and Equation 4.1 , particularly since this discrepancy between curve-fit and experimental results was largest for the ring foil set positioned at fuel rod #10. Equation 4.1 is derived assuming no flux gradient through the medium. Correcting for the fact that the global flux decreases exponentially in the ITS, as $e^{-\gamma r}$, Equation 4.1 changes to:

$$\phi(r) \cong [A_o + A_1\left(\frac{r}{a}\right)^{8/3}]\left(1 + \frac{\gamma^2 r^2}{4}\right)$$

If we calculate the γ from the gold foil activity distribution (which closely represents the total flux distribution) in the ITS (see Figure 3.11) we get $\gamma = 0.1$ and therefore $\frac{\gamma^2 r^2}{4} << 1$ and hence the change in $\phi(r)$ due to this modification is negligible. Thus we are left with "interfacial effects" as the leading candidate for the micro-scale discrepancies as well.

4.3 EFFECT OF NUMBER OF ENERGY GROUPS

One may argue that the discrepancy between the experimental and calculational results is a matter of group structure, that is, it can be resolved by choosing the proper group structure. In order to check this argument, ANISN S8 calculations with G = 4, 26 and 50 (G = number of energy groups; for group structure see Tables 2.3 and 4.1) and 2DB calculations with G = 4 and 26 were performed. The results are illustrated in Figures 4.4 and 4.5 in the form of U_f^{25} and U_c^{28} spatial distributions. By examining the figures, we first notice that all cases show the same

TABLE 4.2

GROUP STRUCTURE OF LIB-IV CROSS SECTION SET (K1)

Group	Neutron Velocity (cm/sec)	Upper Energy (ev)
1	5.27745E + 09	1.99711E + 07
2	3.89009E + 09	1.00000E + 07
3	3.02960E + 09	6.06531E + 06
4	2.35946E + 09	3.67879E + 06
5	1.83755E + 09	2.23130E + 06
6	1.43108E + 09	1.35335E + 06
7	1.11453E + 09	8.20850E + 05
8	9.18596E + 08	4.97871E + 05
9	8.10658E + 08	3.87742E + 05
10	7.15404E + 08	3.01974E + 05
11	6.31341E + 08	2.35177E + 05
12	5.57157E + 08	1.83156E + 05
13	4.91689E + 08	1.42642E + 05
14	4.33914E + 08	1.11090E + 05
15	3.82928E + 08	8.65170E + 04
16	3.37933E + 08	6.73795E + 04
17	2.98225E + 08	5.24752E + 04
18	2.63182E + 08	4.08677E + 04
19	2.32258E + 08	3.18278E + 04
20	2.04967E + 08	2.47875E + 04
21	1.80882E + 08	1.93045E + 04
22	1.59628E + 08	1.50344E + 04
23	1.40871E + 08	1.17088E + 04
24	1.24319E + 08	9.11882E + 03
25	1.09711E + 08	7.10174E + 03
26	9.68193E + 07	5.53084E + 03
27	8.54428E + 07	4.30743E + 03
28	7.54030E + 07	3.35463E + 03
29	6.65429E + 07	2.61259E + 03
30	5.87239E + 07	2.03468E + 03
31	5.18237E + 07	1.58461E + 03

TABLE 4.2

(continued)

Group	Neutron Velocity (cm/sec)	Upper Energy (ev)
32	4.57342E + 07	1.23410E + 03
33	4.03603E + 07	9.61117E + 02
34	3.56178E + 07	7.48518E + 02
35	3.14326E + 07	5.82947E + 02
36	2.77392E + 07	4.53999E + 02
37	2.44798E + 07	3.53575E + 02
38	2.04133E + 07	2.75364E + 02
39	1.58989E + 07	1.67017E + 02
40	1.23813E + 07	1.01301E + 02
41	9.64257E + 06	6.14421E + 01
42	7.50964E + 06	3.72665E + 01
43	5.84851E + 06	2.26033E + 01
44	4.55483E + 06	1.37096E + 01
45	3.54730E + 06	8.31529E + 00
46	2.76264E + 06	5.04348E + 00
47	2.15155E + 06	3.05902E + 00
48	1.67563E + 06	1.85539E + 00
49	1.30498E + 06	1.12635E + 00
50	5.73538E + 05	6.82560E - 01
		1.00002E - 05

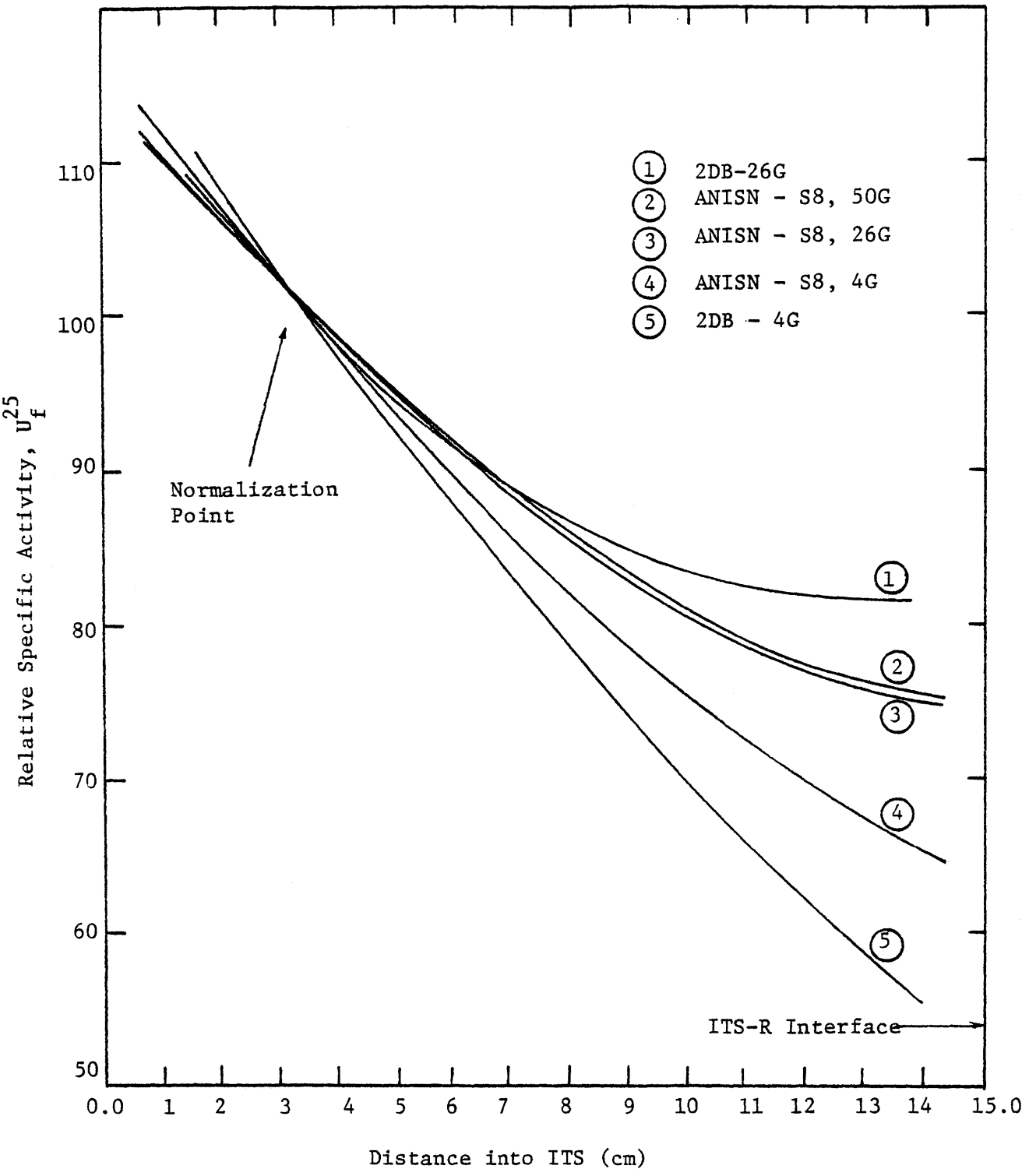

Fig. 4.4 NORMALIZED U_f^{25} DISTRIBUTION THROUGH THE ITS AS A FUNCTION OF THE NUMBER OF GROUPS

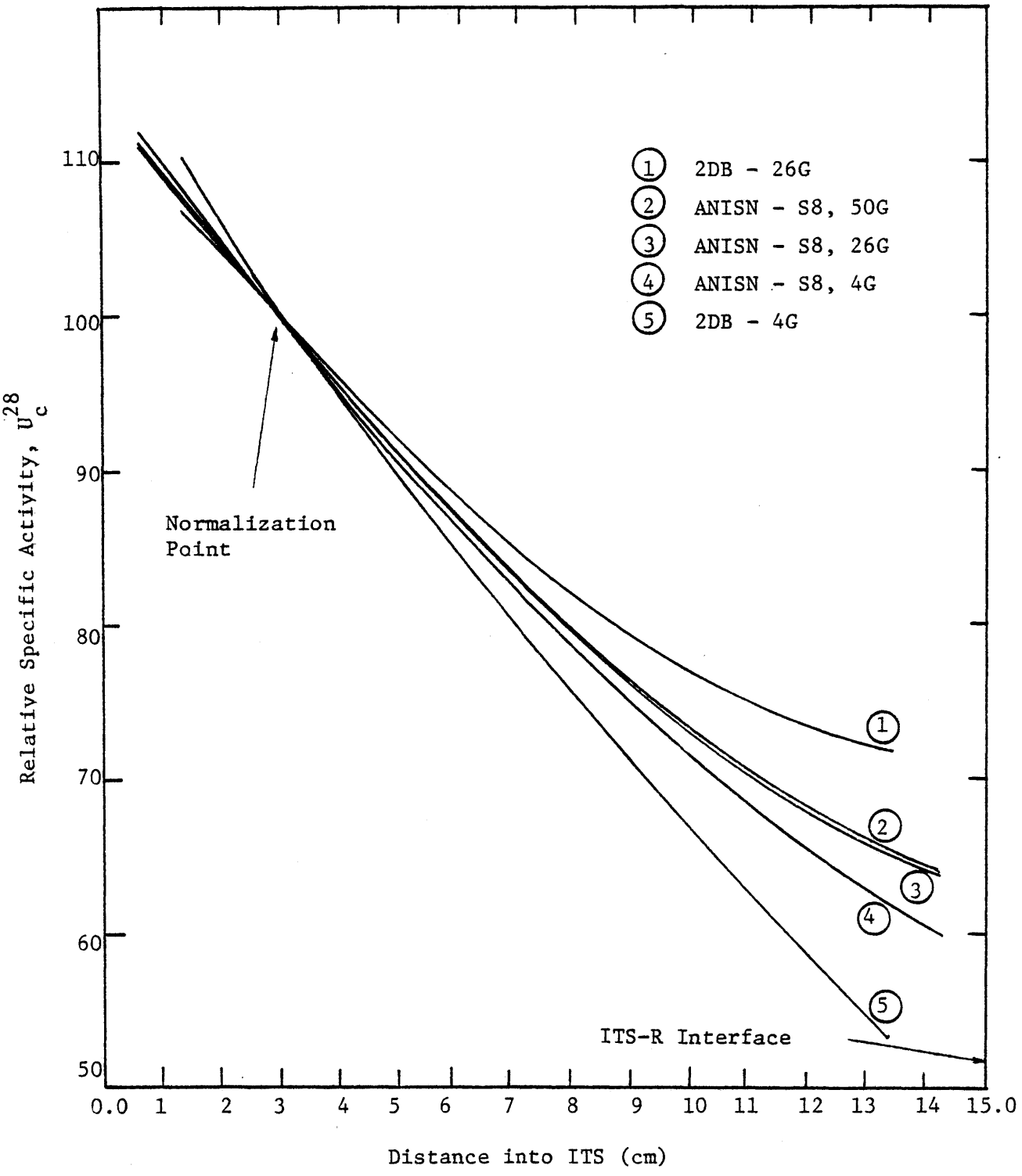

Fig. 4.5 NORMALIZED U_c^{28} DISTRIBUTION THROUGH THE ITS AS A FUNCTION OF THE NUMBER OF GROUPS

general trend, and none show the interfacial effect for the U_c^{28} distribution. The curves are only shifted up or down around the normalization point. One notices larger differences in going from G = 4 to G = 26 than from G = 26 to 50, as would be expected. One must conclude that 4 groups are just too few for present purposes. It is also noticed that the G = 26 (S8) and G = 50 (S8) results are very close, hence the G = 26 level calculation would be sufficient for computer simulations. The change from G = 4 to G = 26 for U_f^{25} is more pronounced than for U_c^{28}. This can be explained by the large values of the weakly shielded U-235 fission cross section in all epithermal groups. We note that ANISN and 2DB results having the same number of groups, G, differ considerably (due to inherent differences between these two codes; i.e. transport versus diffusion theory), and the corresponding ANISN result is closer to the experimental result, as would be expected. The 2DB G = 4 and G = 26 results underestimate and overestimate the experimental results. For ANISN, the U_f^{25} and U_c^{28} rates are about the same for G = 50 and G = 26; therefore increasing the number of groups beyond some sufficient value does not necessarily give closer agreement with experiments.

In short, we conclude that increasing G does not reproduce the interfacial effect, and calculations at the ANISN-S8-26G level are adequate for computer simulation of most aspects of the problem.

4.4 EFFECT OF QUADRATURE ORDER ON ANISN RESULTS

In the solution of the Boltzmann equation, integration over the direction variable, $\hat{\Omega}$ is necessary (H1). In obtaining numerical solutions in the ANISN code, this integration is performed by mechanical

quadrature, where the continuous variable $\hat{\Omega}$ is represented by a set of discrete directions ($\hat{\Omega}_s$) and a corresponding set of weights (P_s). These directions are then equivalent to a set of points upon a unit sphere with origin at R. In these cases where the azimuthal $\hat{\Omega}$ component can be eliminated, the mechanical quadrature representation is achieved using a set of direction cosines (μ_m) for the discrete directions (Ω_s) and a set of level weights (w_m) for the point weights (P_s) over level m (see Reference A1 for tables of μ_m and w_m for different quadrature order). It should be noted that this method (called the S_N method, where N is the quadrature order-number of discrete directions) is based on the assumption of linear variation of the directional flux between interpolation points in both angular and spatial variations (see Reference C1). Even though the S_N method is very useful for the analysis of reactor problems for which diffusion theory is an inadequate approximation, it suffers from one defect that can be serious in certain types of problems. The effect referred to, called the ray effect, arises because neutrons that can move only in certain discrete directions will not be able to reach certain portions of the media by direct flight. In order to check for this effect and others on the ITS results, ANISN 50 group and 4 group runs were performed with N = 2 and N = 8. It was found that the U_c^{28} and U_f^{25} distribution through the ITS were almost the same (within 2%) for N=2 and N=8 cases. This also implies that the flux is not too far from isotropic, that is,not a strong function of the angular direction $\hat{\Omega}$.

4.5 COMPARISON WITH PREVIOUS MIT EXPERIMENTS

In this section the ITS experimental results are compared with results of other similar experiments which have been done at MIT using the Blanket Test Facility. This comparison should provide a better appreciation of the nature of the interfacial effect. There are three sets of data for comparison; the experiments performed by Leung (L3), Kadiroglu (K2) and Medeiros (M2); for simplicity in this section they are indicated by L3, K2 and M2. Some of the L3 data are shown in Figures 4.6 and 4.7 (reproduced from Reference L3). The figures show the U_c^{28} distribution for two cases, one when non-fuel traversing tubes were used, the foils being placed vertically in the tube (the so-called ex-rod U^{28} capture rate), and the other when the traversing tubes were filled with uranium metal slugs and the uranium foils sandwiched horizontally between the slugs, as was done in the ITS experiments. Three ANISN S8 calculations are also plotted in Figure 4.6; the dotted line is when unshielded cross sections were used and the solid line is when self-shielded cross sections were used for calculating the flux (but for calculating the U_c^{28} rate, the fluxes were multiplied by unshielded U^{28} cross sections since the foils were placed in unfueled tubes). In Figure 4.7, the dotted line represents the ANISN S8 results for the U_c^{28} distribution when self-shielded cross sections are used both in the flux computations and in the U_c^{28} calculations for the in-rod uranium foils. This is also the procedure followed for the current ITS ANISN calculations. Comparing the ITS U_c^{28} experimental results with the Figure 4.7 in-rod foil results shows that they both follow the same trend, and they both show that the interfacial effect starts about 3.0 cm from the interface in the blanket. However,

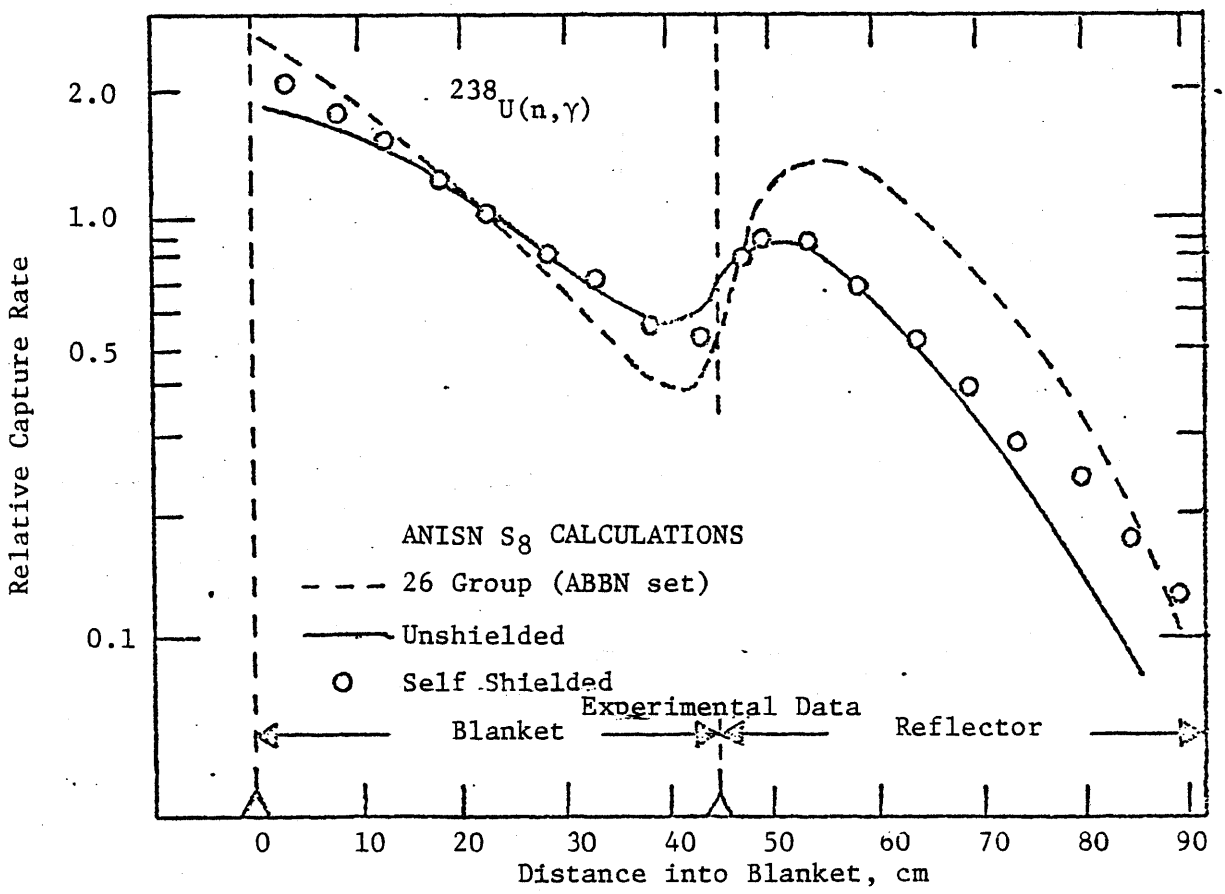

Figure 4.6 Effect of 238U Self-Shielded Cross Sections on Reaction Rate Calculations (from Ref. L3)

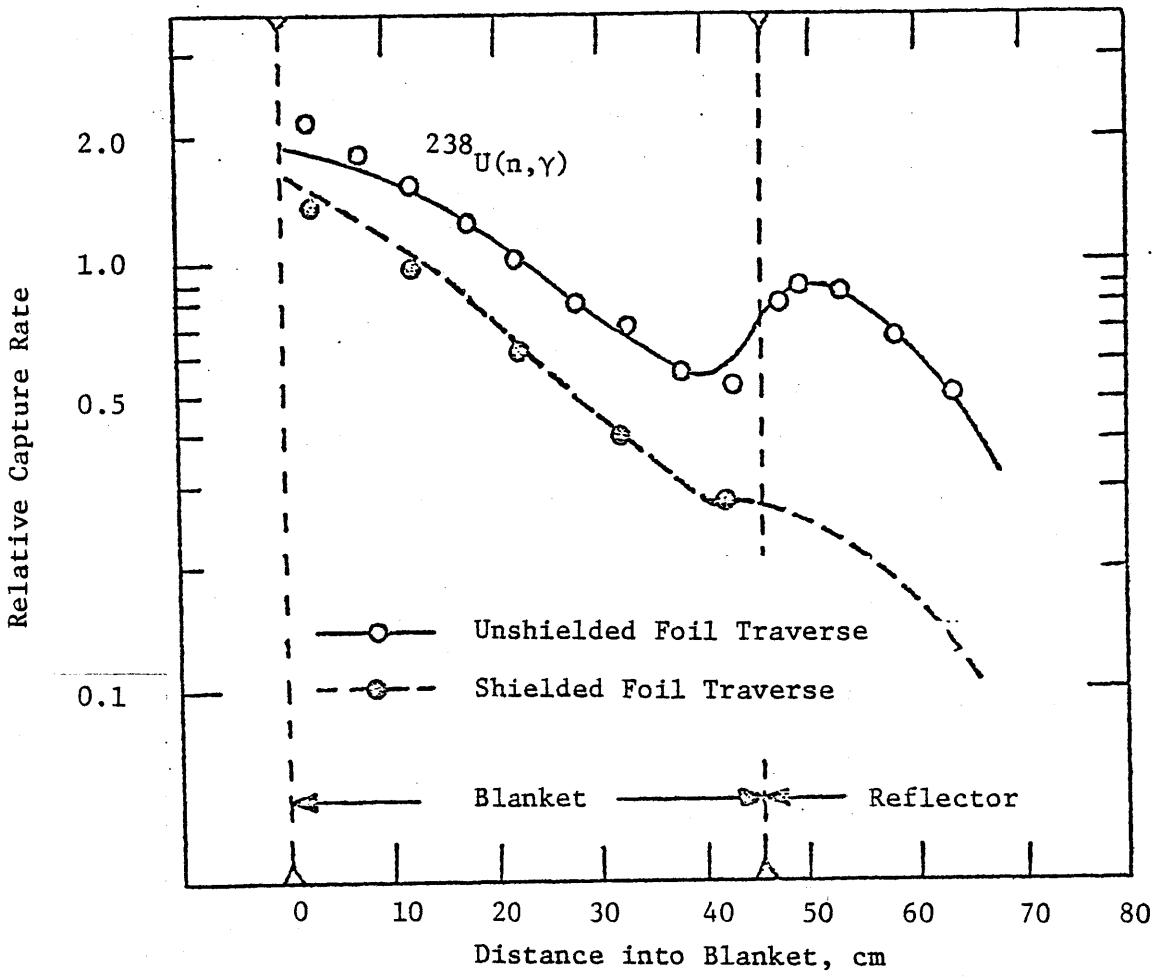

Figure 4.7 Comparison of Shielded (in-rod) and Unshielded (ex-rod) 238-U Foil Traverses (from Ref. L3)

due to the wide data point spacing, there is no data for comparison in the crucial 2 cm zone near the interface. Figure 4.6 shows that neither of the two ANISN calculations can fit the experimental data well, but rather suggests that a cross section set in between the self-shielded and unshielded sets might suffice. In Chapter 5 this intermediate cross section set is generated. Figure 4.7 shows that the ANISN calculation for ex-rod foils can produce a buildup in U_c^{28} near the interface, while all the state-of-the-art calculations (2DB and ANISN, for different numbers of energy groups) performed for the ITS indicate a steady decrease in U_c^{28} even near the interface. Examining the neutron flux in each group shows that the high energy neutron flux steadily decreases through the interface, while the low energy neutron flux (below $\sim$0.2 kev and especially the group around the highest resonance in U^{28} at $\sim$6 ev) starts to increase near the interface. Therefore for the ex-rod U_c^{28} distributions, since unshielded cross sections were used for the U_c^{28} calculations the large values of σ_c^{28} at low energies ($\sim$264 barns at g = 45 in a 50-group structure) make the effect of the low energy fluxes more pronounced, and hence Leung's U_c^{28} ex-rod calculation shows a buildup, while for the in-rod U_c^{28} distributions in the present case, self shielded cross sections are used, and σ_c^{28} values in this case are smaller ($\sim$20 barns at g = 45) and hence the U_c^{28} in-rod calculations show a steady decrease right up to the interface. This behavior also suggests that in order to treat the interfacial effect properly, one should use an "intermediate cross section set", one which systematically interpolates between the heavily shielded in-blanket structure and the unshielded in-reflector case.

The K2 experimental results were renormalized to the same point as the ITS U_c^{28} distribution, and both are plotted in Figure 4.8. Since the

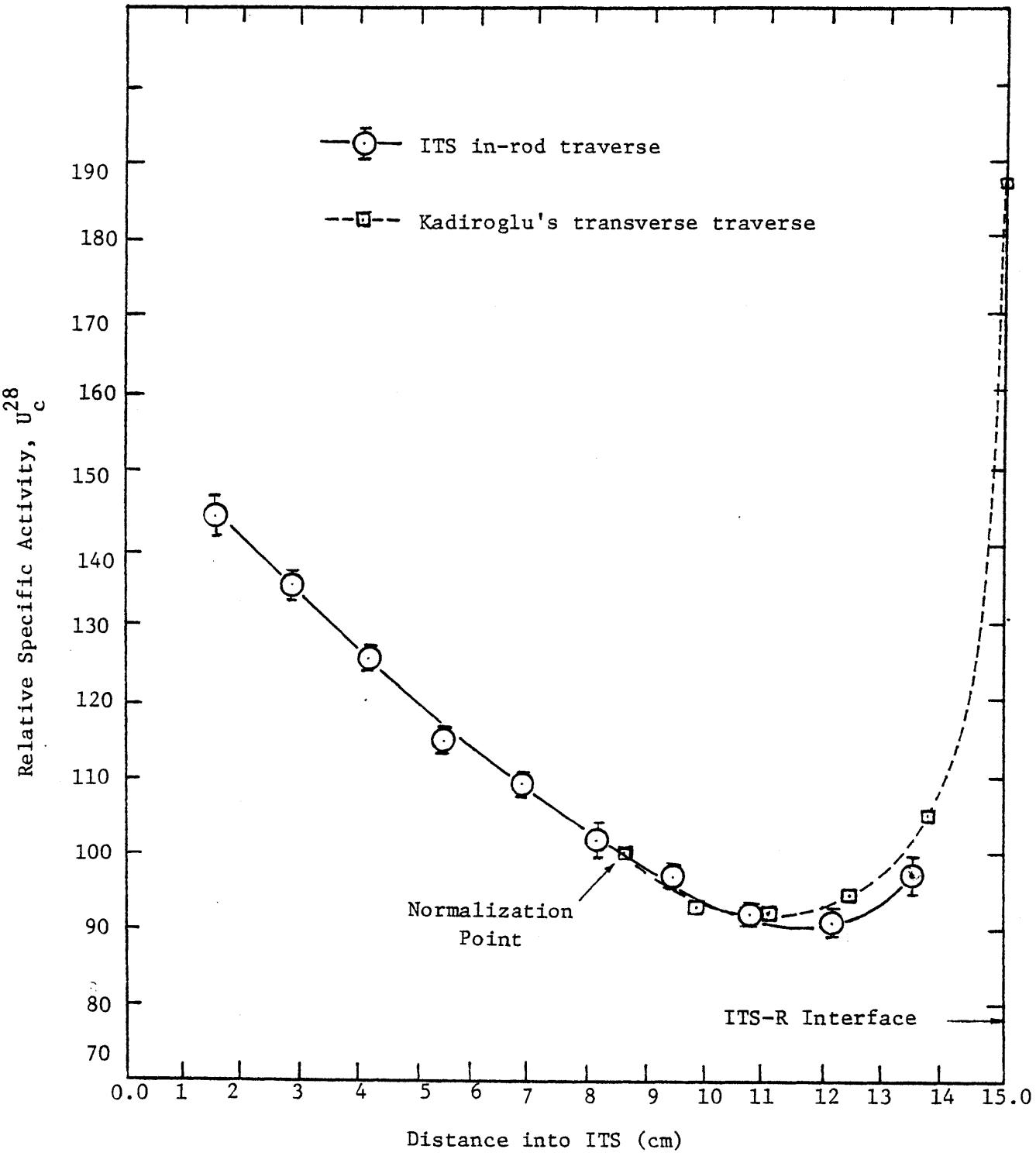

Fig. 4.8 U_c^{28} DISTRIBUTION THROUGH BLANKET SUBASSEMBLY AND ITS

only data available from K2 was the plot, some error is introduced in the data transfer and renormalization process. Nevertheless, it is evident that the experiments are in good agreement. Note that the K2 data were measured using a fuel pin inserted normal to the interface rather than parallel as in the ITS work. Thus the data point at the interface in the K2 experiment is the U_c^{28} activity of a foil placed vertically exactly at the blanket-reflector interface. In this regard it can be thought of as more of an "ex-rod" foil. In the ITS data the horizontal in-rod foil averages U_c^{28} over the entire fuel pin cross section; presumably only the outer layer of the pin facing the reflector is as highly activated as the outermost foil in the K2 results. Next the M2 experiment is considered, one carried out on a configuration considerably different than those considered up to this point. As Figure 4.9 shows, the interfacial effect is significant in this case. The figure illustrates the U_c^{28} and the Th_c^{02} captures inside a fuel rod of a special subassembly in which each uranium fuel rod contains a 12 inch thorium insert at the mid plane (see Reference M2 for more information). The uranium-thorium foils are placed 2 inches apart and both types of foils are paired at the uranium-thorium interface. A 70% buildup in U_c^{28} in the interfacial foil is observed compared to the next interior uranium foil. This high buildup is expected, since it represents the interface effect right at the intersection: somewhat analogous to the situation in the K2 experiments. The thorium foils at the midplane and at the upper Th/U interface show a similar, but smaller effect (since the infinitely dilute resonance integral for Th-232 is smaller than that of U-238, 80 versus 264 barns respectively).

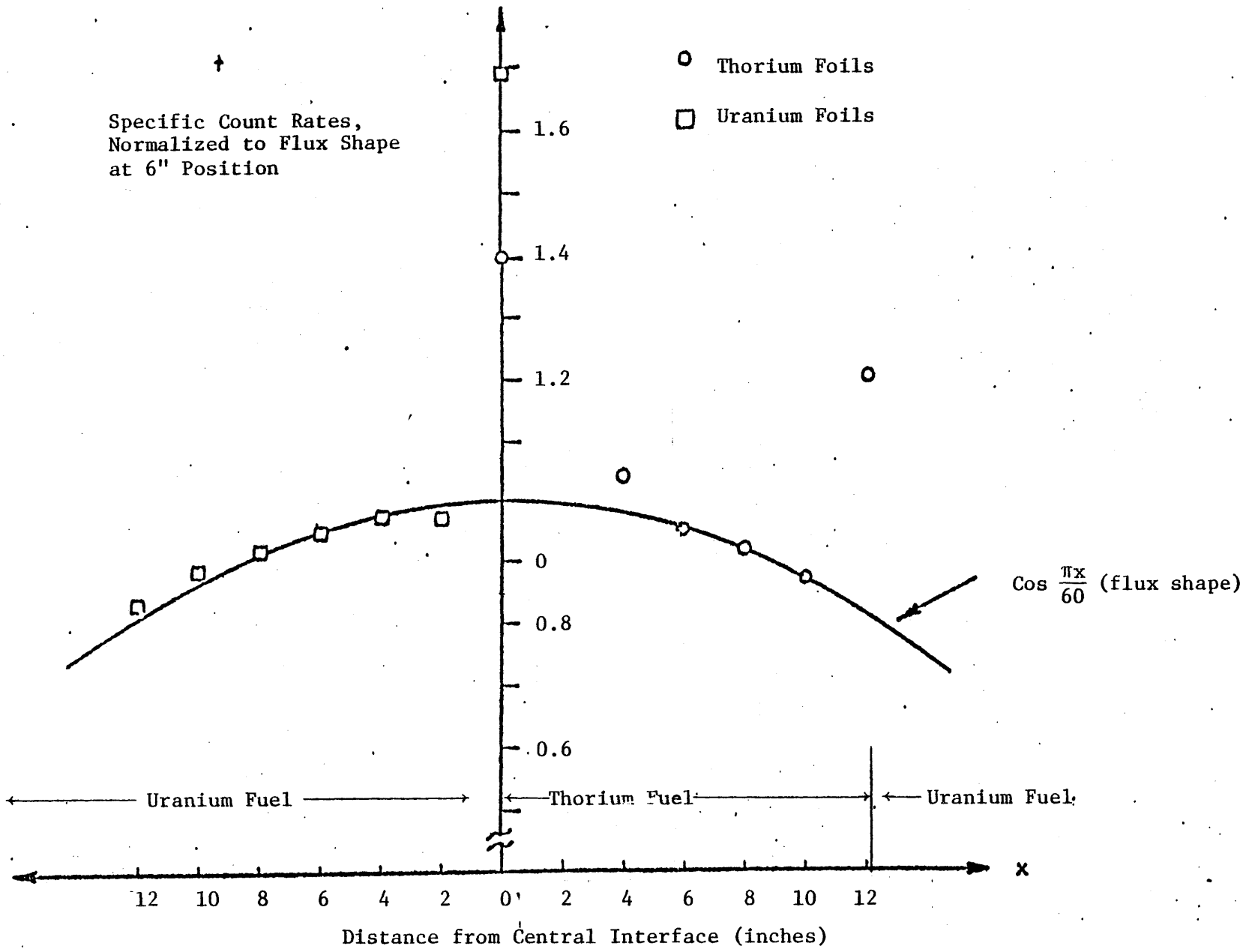

Figure 4.9 Uranium and Thorium Traverses (from Ref. M2)

4.6 EFFECT OF LATTICE STRUCTURE AND FUEL SLOWING DOWN SOURCE (Q_f) ON THE SELF-SHIELDING FACTOR

In section 4.5 it was noted that the K2 results and the results of the present work for the U_c^{28} distribution in the blanket and near the interface are similar within the errors involved. This suggests that even though the unit cell structure differs for the two cases and Q_f is essentially zero for the K2 experiments (uranium metal fuel) but non-negligible for the ITS cell (UO_2 fuel), the overall effect is negligible. It was, however, considered desirable to study these phenomena more thoroughly to find how much of an effect these variables have on the self-shielding factor, and consequently on cross sections and on enhancement of the interfacial effect. Since all calculations and experiments done in the present work have been for a specific cell structure (see Figure 2.7), it will be of interest to examine whether the numerical results are also valid for the Standard Blanket cell structure (the cell structure used in the K2 and other experiments).

In order to calculate the self-shielding factors, the SPHINX code (D4) was used, which is described briefly in the following subsection, followed by the case studies in the next subsection.

4.6.1 The SPHINX Code

The SPHINX code uses both one dimensional diffusion and transport theories in order to provide a calculational scheme for generating multigroup cross sections which may then be self-shielded and space-energy collapsed to desired specifications. The basic input to SPHINX are cross sections and self-shielding factors in standard format as

produced by the cross section processing code MINX (W1). The MINX Code produces pseudo-composition independent libraries of group cross sections, self-shielding factors and group-to-group transfer matrices. The group cross sections and transfer matrices are stored on the ISOTXS file (C1) and the self-shielding factors are stored on the BROKXS files(C1). SPHINX interpolates the self-shielding factors from MINX to correct for composition and temperature by calculating the equivalent background cross section σ_o (see Chapter 5 and also refer to Ref. D3 for more detail). SPHINX uses these σ_o values to determine self-shielding factors from the tables of self-shielding factors versus σ_o contained on the BROKXS file. Since the σ_o's calculated for a given composition of interest rarely match the σ_o values on the BROKXS file, interpolation is required to determine the self-shielding factors. The interpolation algorithm used (P2) is an Aitken-Lagrange interpolation scheme. The order of the Lagrangian interpolations is determined by the number of table points. SPHINX also generates cross sections for heterogeneous cells. Applying an equivalence theorem, it homogenizes the cell by using the equivalent σ_o for a heterogeneous cell. Eight options (indicated by a parameter called ISSOPT varying from 0 to 7) are offered in SPHINX for the calculation of σ_o (D3):

1. Homogeneous option
2. Sauer's approximation in cylindrical geometry within a hexagonal lattice (S3)
3. Sauer's approximation in cylindrical geometry within a square lattice (S3)
4. Symmetric slab cell

5. Asymmetric slab cell
6. Isolated rod
7. Cylindrical cell in the Bell Approximation (B2)
8. Symmetric slab cell in the Bell Approximation (B2)

In these options, the appropriate Dancoff factor is calculated, and used to correct the corresponding value of σ_o. In section 5.3, we will derive a formula for calculating the Dancoff factor at the interface which can be added to the SPHINX code as another option.

The SPHINX code was developed at WARD and completed in August 1977. The version of SPHINX which exists in MIT only produces P_o cross sections.

The SPHINX code needs as input the specific geometry of the pin cell, the number densities, and the temperature. For more information about SPHINX one may consult the literature (C1, D3, M1).

4.6.2 Case Studies

Six different cases were studied using the SPHINX Code. A square lattice and a hexagonal lattice with the same elemental composition as a Standard Blanket Cell (See Table 2.4) were investigated. It was found that the self-shielding factors were essentially the same in both cases for all energy groups (a 50-group structure was used; see Table 4.1 for the group structure).

In another case study, the ITS unit cell was used in two cases but with smaller V_m (moderator fractional volume) and V_f (fuel fractional volume) by a factor of 2.5, while keeping the V_m/V_f ratio the same. The self shielding factor for the smaller cell was greater for groups $g \geq 16$

but with percentage differences less than 4.5%; the other factors were essentially the same for $g \leq 16$. In another case study the K2 unit cell (r_f = 0.318 cm, r_m = 0.732 cm, V_m/V_f = 5.30) was compared versus another unit cell with the same elemental composition but with ITS lattice structure (r_f = 0.546 cm, r_m = 0.814 cm, V_m/V_f = 2.22). It was found that the self-shielding factors for the K2 cell were greater for $g > 16$ (but not more than 48%) and about equal for $g \leq 16$.

To study the effect of a slowing down source in the fuel region, Q_f, the ITS unit cell (UO_2 pellets; $Q_f \neq 0$) was compared with the same ITS unit cell but with the O_2 constituent of the UO_2 transfered to the moderator region. The self shielding factors of the $Q_f \neq 0$ cell were greater, but differences were less than 2% for $g > 17$ and negligible for $g \leq 17$. This shows that the effect of Q_f on the self shielding factor is negligible. In the method developed by A. Salehi (S2) at MIT for treating heterogeneous cells, self shielding factors and Dancoff factors are derived for $Q_f = 0$. In Appendix B the Dancoff factor for $Q_f \neq 0$ is derived, and it is shown that the correction changes the Dancoff factor, and hence the self-shielding factor, very slightly (less than 1%) which is consistant with the case study results.

Lastly, the K2 unit cell (see Figure 2.4) and the ITS unit cell were studied, and it was found that the self shielding factor of the former was smaller than the latter, with percentage differences not greater than 5% for $g > 16$; and values are essentially the same for $g \leq 16$. In this case two factors affect the self-shielding, but in opposite directions, hence the overall effect is smaller than the individual effects. These two factors are number densities of the unit cell and V_m/V_f ratio. Even though

the ITS and K2 unit cells have different V_m/V_f ratios, they also have different number densities which vary proportional to the inverse of V_m/V_f and hence partly cancel out each other.

From these case studies, it is concluded that the Q_f value has a negligible effect on the self-shielding factor value, and unit cell structure and elemental composition together introduce minor changes in the self-shielding factor, therefore both bulk medium and interface effects for the Standard Blanket-Reflector and for the ITS-Reflector should be comparable.

Finally, it should be noted that at higher energies, that is in the lower numbered energy groups, where the resonances are small or unresolved, the self-shielding effect is insignificant, and hence the self-shielding factor is close to 1.0. This is why in all of the above case studies values match for $g \leq 16$ ($E \geq 67.4$ kev).

4.7 SUMMARY

In this chapter the ITS experimental results were compared with state-of-the-art calculational results, and with other comparable experiments performed at MIT, to isolate the factors which are involved in the interfacial effect. It was found that the state-of-the-art calculations (using infinite medium shielding) did not show the interface effect, and changing group structure or quadrature order does not help. Examination of Leung's results (L3) showed that neither of the two limiting cross section sets, that is unshielded and shielded, correctly predict the behavior near the interface, hence supporting the view that an intermediate cross section set should be used near the interface or

in other words that space dependent effects on self shielding should be considered. Comparison with Kadiroglu's results (K2) showed that the interfacial effect in his assembly agrees with that measured with the ITS, and accounted for an augmentation of about 8% in the U_c^{28} rate of the blanket pin nearest the interface. This correspondence was shown to be compatible with theoretical expectations. Even though the K2 and ITS have different unit cell structure and fuel slowing down sources, the effect of these factors on the self-shielding factor was studied and found to be negligible. Finally, comparison with Medeiros' results (M2) showed that the interface effect can be quite large right at the boundary, but dies out quite rapidly with depth. Thus, pin-averaged capture rates are much less than surface foil rates.

CHAPTER 5

DERIVATION OF SELF SHIELDING FACTORS AT AND NEAR AN INTERFACE

5.1 INTRODUCTION

An adequate foundation has now been established to permit a more analytic examination of the self-shielding factor at and near an interface. To procede toward this objective, in Section 5.2 different types of self shielding are discussed, along with their relative importance, and the possible effect of interface effects on each. Section 5.2 is devoted to a derivation of modified space-dependent homogeneous and heterogeneous self-shielding factors. Using these new factors, appropriately self-shielded cross sections are generated in Section 5.4. Using this new cross section set in the ANISN program, fertile capture distributions for the ITS-Reflector and Th-U assembly cases are developed, as explained in Section 5.5. In this section the new ANISN results are also compared with experimental data and with previous ANISN calculations. Finally this chapter is summarized in Section 5.6.

5.2 NEUTRON CROSS SECTION SELF-SHIELDING PHENOMENA

An essential step in most reactor physics calculations is the replacement of the energy-space dependent diffusion or transport equation by space dependent few group equations. The few group method is rationalized by introducing few group constants such as the diffusion constant, D_g, (where g is the energy group number) which correctly reproduce group leakage, or microscopic cross sections, σ_g, based on preserving reaction rates.

To proceed, we begin with homogeneous systems. For an infinite homogeneous system the group-averaged cross sections when the resonant materials present in the medium are infinitely dilute are defined as follows:

$$\sigma_{xg} = \frac{\int_{\Delta Eg} \Phi(r,E)\sigma_x(E)dE}{\int_{\Delta Eg} \Phi(r,E)dE} \tag{5.1}$$

If we assume that $\Phi(r,E) = \Phi(r)\psi(E)$, which is valid within the medium but not valid near the interfaces of two dissimilar materials, we get:

$$\sigma_{xg} = \frac{\int_{\Delta Eg} \psi(E)\sigma_x(E)dE}{\int_{\Delta Eg} \psi(E)dE} \tag{5.2}$$

For the infinite dilution case, the neutron energy spectrum, $\psi^{\infty}(E)$, is (to good and often used approximations) $\frac{1}{E}$ for the epithermal energy range, maxwellian for thermal energies, and a fission spectrum for the fast energy range. But if there is an appreciable resonant isotope concentration in the system, the neutron flux is depressed for those energies in the neighborhood of the resonance (see Figure 5.1). This effect is known as "energy self-shielding" or "homogeneous self-shielding" since the strong absorption of the resonance tends to shield the absorber nuclei from neutrons with energy $E \sim E_o$ (the flux depression). Since resonance cross sections are strongly temperature dependent, it therefore follows that self-shielding is a temperature-dependent phenomena as well. Self shielding also depends on medium composition. When the resonant isotopes in the medium are not infinitely dilute, the energy spectrum is found by solving the slowing down

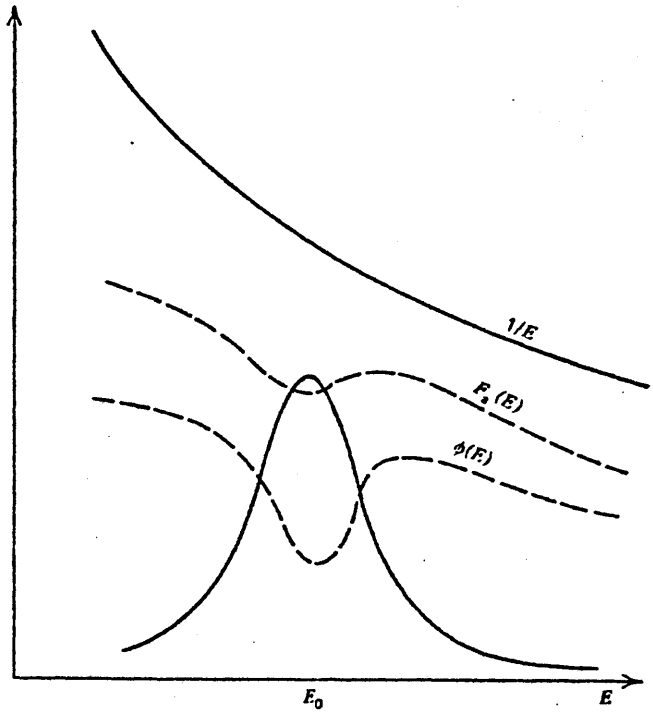

Figure 5.1 Flux Depression in the Neighborhood of a Resonance

equation for a uniform mixture of infinite extent (G1); using the narrow resonance approximation for non-resonant isotopes and the intermediate resonance approximation for the resonant isotope (in the derivation it is assumed that only one resonant isotope exists in the medium; also since we are most often dealing with U-238 as the resonant isotope the narrow resonance approximation is often adopted; but for the largest and lowest resonances the wide resonance approximation may be more appropriate). The result is:

$$\psi^{hom}(E,T,\sigma_o) = \frac{\sigma_o + \lambda\sigma_{pr}}{\sigma_{ar}(E,T) + \lambda\sigma_{sr}(E,T) + \sigma_o} \frac{1}{E} \tag{5.3}$$

where

$$\sigma_o = \frac{\sum_{i \neq j} \Sigma_{ti}}{N_j}$$

and

Σ_{ti} = total macroscopic cross section (non-resonant isotope i)

N_j = atomic volume (≡ nuclear number) density of resonant isotope j (eg. nuclei/barn cm)

σ_{ar}, σ_{sr}, σ_{pr} = resonant absorption, scattering and potential scattering cross sections of the resonant isotope j

Inserting the value of $\psi(E,T,\sigma_o)$ into Equation (5.2) gives the group averaged cross section for the resonance isotope:

$$\sigma_{xg}(T,\sigma_o) = \frac{\int_{\Delta Eg} \frac{\sigma_o + \lambda\sigma_{pr}}{\sigma_{ar} + \lambda\sigma_{sr} + \sigma_o} \sigma_x(E,T) \frac{dE}{E}}{\int_{\Delta Eg} \frac{\sigma_o + \lambda\sigma_{pr}}{\sigma_{ar} + \lambda\sigma_{sr} + \sigma_o} \frac{dE}{E}} \tag{5.4}$$

Since σ_o and σ_{pr} are nearly constant within ΔEg then:

$$\sigma_{xg}(T,\sigma_o) = \frac{\int_{\Delta Eg} \frac{\sigma_x(E,T)}{\sigma_{tr}(E,T) + \sigma_o} \frac{dE}{E}}{\int_{\Delta Eg} \frac{1}{\sigma_{tr}(E,T) + \sigma_o} \frac{dE}{E}} ; \tag{5.5}$$

$$\sigma_{tr} = \sigma_{ar} + \lambda\sigma_{sr}$$

The energy self-shielded cross section $\sigma_{xg}(T,\sigma_o)$ and unshielded cross section σ^{∞}_{xg} (infinitely dilute cross section defined in Equation (5.2)) are customarily related by a factor called the "self shielding factor", $f_{xg}(T,\sigma_o)$:

$$\sigma_{xg}(T,\sigma_o) = f_{xg}(T,\sigma_o)\sigma^{\infty}_{xg} \tag{5.6}$$

The "self shielding factor" was first popularized by Bondarenko in 1964 (B1). Having the f_{xg} values at different T and σ_o values, and σ^{∞}_{xg} values, one can find the σ_{xg} values. The f factors for elastic scattering, capture, fission transport and total cross sections for different values of T and σ_o are tabulated in a number of state-of-the-art cross section libraries: LIB-IV for example (K1). The f factors for any given T and σ_o can then be obtained

by interpolating in these tables. Reference (K5) describes the conventions employed in some detail.

But the assumption $\Phi(r,E) = \Phi(r)\psi(E)$ is not valid near interfaces and hence the energy self shielded cross sections σ_{xg}, would be space dependent near an interface between two dissimilar media. Refer to Equation (5.2) and note that $\sigma_{xg}(T,\sigma_o)$ defined in Equation 5.5 only represents the asymptotic value. The σ_{xg} and σ^{∞}_{xg} values are valid a few mean free paths away from the interface. In the next section proper group-averaged cross sections near the interfaces are derived.

So far we have been discussing the self shielding of homogeneous systems. But in essentially all reactor designs, lumped fuels are used rather than a homogeneous mixture of fuel material and moderator, due to practical problems and physical advantages. When the fuel is lumped into a heterogeneous lattice, the resonance escape probability increases dramatically (D3, H1). This occurs because neutrons are slowed down past resonance energies in the moderator, escaping exposure to nuclei within the fuel region at resonance energies. That is, the outer layers of the fuel tend to "shield" its interior from resonance neutrons, thereby decreasing the net resonance absorption and hence increasing the resonance escape probability, p. This self shielding, which is called "spatial" or "heterogeneous" self-shielding is in many ways analogous to the energy self-shielding. Both effects tend to decrease resonance absorption, thereby increasing the resonance escape probability.

Heterogeneous self shielding is very often treated by cell homogenization through application of so-called equivalence theorems. It is assumed that one subelement, or so-called "unit cell" is repeated throughout

the core or blanket. The essential scheme in cell homogenization is to perform a detailed calculation of the flux distribution in a given unit cell of the lattice - assuming that there is zero net neutron current across the boundary of the cell. The various energy dependent cross sections characterizing materials in the cell are then spatially averaged over the cell, using the flux distribution as a weighting function. In this way one can characterize the cell by effective group constants accounting for the inhomogeneous flux distribution in the cell. This scheme essentially replaces the actual unit cell by an equivalent homogeneous unit cell characterized by these effective cross sections. The homogenization process is affected by applying equivalence theory prescriptions to reduce heterogeneous configurations to the corresponding homogeneous cases for which resonance integrals are defined (D5, H1, L4, M3). Representative equivalence theorems are (D1, D5):

1. Heterogeneous systems with the same σ_o' have equal resonance integrals.
2. A heterogeneous system will have the same resonance integral as a homogeneous system evaluated at σ_o' where

$$\sigma_o' = \frac{\bar{\Sigma}_{tn\,f}}{\bar{N}_j} + \frac{1}{1 + \frac{1}{a}\tau_{tm}} \frac{\bar{\Sigma}_{tm}}{\bar{N}_j} \tag{5.6}$$

$\bar{\Sigma}_{tnf}$ = total macroscopic cross section of non-resonance isotopes of fuel region homogenized over the fuel region

$\bar{N}_j$ = homogenized atomic density of resonant isotope j over the fuel region

$\bar{\Sigma}_{tm}$ = total macroscopic cross section of isotopes in the moderator homogenized over the moderator region

τ_{tm} = total optical thickness of the moderator

a = Levine factor (L2)

σ_o' is the modified constant "background" cross section per resonant nucleus j. The above derivation for σ_o' is based on the assumption that the unit cell is truly isolated and hence the interference from the surrounding fuel lumps has not been considered. To correct for this effect, the rod shadowing concept (D1, D5) is introduced. The correction is made through the introduction of an effective surface area of the fuel S_{eff} (F1): $S_{eff} = S(1 - C)$ where C is called the "Dancoff-Ginsberg" factor or more commonly just the "Dancoff" factor (D6), and S is the fuel surface area. Actually, this treatment merely corresponds to increasing the average chord length ($\ell = \frac{4V}{S}$) in the fuel lump by a factor $(1 - C)^{-1}$. Hence the Dancoff factor simply decreases the resonance cross section. This correction implies that

$$\sigma_o' = \frac{\bar{\Sigma}_{tn\ f}}{\bar{N}_j} + \frac{a(1 - C)}{1 + (a - 1)C} \frac{\bar{\Sigma}_{tm}}{\bar{N}_j} \tag{5.7}$$

As a point of interest it is noted that Salehi has derived this relation directly from unit cell theory without the need for first neglecting and then re-introducing the shadowing by neighboring unit cells (S2). He has also incorporated the more general formulations of intermediate

resonance (IR) theory in his derivation, which incorporate the NR and WR results into a consistent framework.

In the heterogeneous self shielding treatment, it was noticed that first the treatment was based on having no shadowing effect, and then it was à posteriori corrected for the shadowing effect. However, the Dancoff factor just refered to is derived for an infinite heterogeneous medium - an assumption which is not valid near interfaces, where one of the half spaces might even be a homogeneous medium (such as at a blanket-reflector interface) or a medium with different unit cell sizes and compositions (core-blanket) or a medium free of the resonance absorber in question. Therefore a space-dependent Dancoff factor near the interface should be derived, with an asymptotic value equal to the Dancoff factor for an infinite medium. This derivation is described in Section 5.4.

Each of the corrections mentioned above decreases the resonance material's absorption cross section, but in different proportion. The energy self-shielding correction is more significant than the other two. For example, the unshielded U-238 capture cross section for g = 45 in the LIB-IV 50 group energy structure (5.04 to 8.32 ev) is $\sim$264 barns. The homogeneously self shielded value is $\sim$25 barns for a typical FBR unit cell, and the overall (spatial plus shadowing) heterogeneous self shielding value is $\sim$20 barns.

5.3 CORRECTION OF INFINITE HOMOGENEOUS SELF-SHIELDING NEAR THE INTERFACE

Consider a two-region homogeneous system with region one containing resonant isotopes with atomic number density N_j and region two containing an infinitely dilute amount of the resonant isotope N_j.

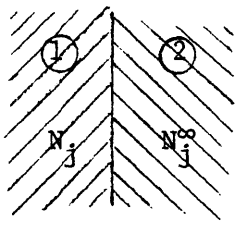

Normally in the state-of-the-art calculations, two different sets of cross sections are used, one in each region: self-shielded cross sections for region one and unshielded cross sections for region two. This treatment is implicitly based on the assumption that flux separability, $\Phi(\underline{r},E) = \Phi(\underline{r})\psi(E)$, is valid throughout each region. But as mentioned previously, this assumption is not valid near the interface of two dissimilar materials, and hence applying σ_{xg}^{hom} and σ_{xg}^{∞} (see Section 5.2 for their definition) for regions 1 and 2, respectively, is erroneous near the interface. Thus our goal is to find a more realistic value for the flux, $\Phi(\underline{r},E)$, at and near the interface. Then by using the definition of "group averaged cross section" given in Section 5.2, an attempt can be made to find a space-dependent group-averaged cross section $\sigma_{xg}^{hom}(x)$ that has an asymptotic value equal to σ_{xg}^{hom} and σ_{xg}^{∞} in regions 1 and 2 respectively.

Since the resonances appear in the slowing down energy region and the self-shielding effect for energies outside this region is negligible, only the neutron energy spectrum in the slowing down region

is considered.

As we recall, from Section 5.2, σ_{xg}^{hom} and σ_{xg}^{∞} were derived by averaging $\sigma_x(E)$ over energy band ΔEg with the weighting functions (neutron energy spectra) equal to

$$\psi^{hom}(E) = \frac{\sigma_o + \lambda\sigma_{pr}}{\sigma_o + \sigma_{ar} + \lambda\sigma_{sr}} \quad \text{and} \quad \psi^{\infty}(E) = \frac{1}{E} \text{ , respectively.}$$

The neutron flux near an interface is the superposition of two components, asymptotic and transient (W1):

$$\Phi(E,x) = \Phi_{As}(E,x) + \Phi_{tr}(E,x) \tag{5.8}$$

A few mean free paths away from an interface the transient neutron flux diminishes and we have $\Phi(E,x) = \Phi_{As}(E,x) = \Phi(x)\psi(E)$. Near an interface $\psi(E)$ is no longer space independent and we have $\Phi(E,x) = \Phi(x)\psi(E,x)$. For $x(E,x)$ we have:

$$\psi(E,x) \to \psi^{hom} \text{ as } x \to -\infty \text{ (by } \infty \text{ we mean far from the interface)}$$
$$\psi(E,x) \to \psi^{\infty} = \frac{1}{E} \text{ as } x \to \infty$$

Since near an interface Φ_{tr} changes more rapidly with x than Φ_{As} does (Φ_{As} is a smooth function of x) the distortion in the neutron energy spectrum, $x(E,x)$, is totally associated with the transient component of the flux. Therefore considering the asymptotic limits of $\psi(E,x)$ mentioned above we get:

$$\psi(E,x) = \psi^{hom}(1 - \phi_{tr}^{(1)}) + \alpha\,\phi_{tr}^{(1)} \qquad x \leq 0$$

$$\psi(E,x) = \psi^{\infty}(1 - \phi_{tr}^{(2)}) + \beta\,\phi_{tr}^{(2)} \qquad x \geq 0 \tag{5.9}$$

$\phi_{tr}(E,x)$ is the transient flux normalized to 1.0 at x = 0.0; $\phi_{tr}^{(1)}(E,0) = \phi_{tr}^{(2)}(E,0) = 1.0$. It is clear from Equation (5.9) that $\psi(E,x)$ tends to x^{hom} inside region 1 as we move away from the interface. $\psi(E,x)$ should be continuous at x = 0.0, which leads to: $\alpha = \beta = \psi^{I}(E)$. Inserting the values of a and b into Equation (5.9) we get:

$$\psi(E,x) = \psi^{hom}(1 - \phi_{tr}^{(1)}) + \psi^{I}\phi_{tr}^{(1)} \qquad x \leq 0$$

$$\psi(E,x) = \psi^{\infty}(1 - \phi_{tr}^{(2)}) + \psi^{I}\phi_{tr}^{(2)} \qquad x \geq 0 \tag{5.10}$$

or

$$\Phi^{(1)}(E,x) = \Phi_{As}^{(1)}(E,x) + \Phi^{(1)}(x)[(\psi^{I}(E) - \psi^{hom}(E))\phi_{tr}^{(1)}(E,x)] \qquad x \leq 0$$

$$\Phi^{(2)}(E,x) = \Phi_{As}^{(2)}(E,x) + \Phi^{(2)}(x)[{}^{I}(E) - \psi^{\infty}(E))\phi_{tr}^{(2)}(E,x)] \qquad x \geq 0 \tag{5.11}$$

(note that $\Phi_{As}^{(1)}(\sigma,x) = \Phi^{(1)}(x)\psi^{hom}(E)$ and $\Phi_{As}^{(2)}(E,x) = \Phi^{(2)}(x)\psi^{\infty}(E)$). Applying the continuity of total and asymptotic current at the interface gives:

$$D^{(1)}(\psi^{I} - \psi^{hom})\phi'^{(1)}_{tr}\Big|_{x=0.0} = D^{(2)}(\psi^{I} - \psi^{\infty})\phi'^{(2)}_{tr}\Big|_{x=0.0},$$

which leads to:

$$\psi^{I} = \frac{D^{(2)}\psi^{\infty}{}'^{(2)}_{tr} + D^{(1)}\psi^{hom}{}'^{(1)}_{tr}}{D^{(2)}\phi'^{(2)}_{tr} + D^{(1)}\phi'^{(1)}_{tr}} \tag{5.12}$$

$D^{(1)}$ and $D^{(2)}$ are diffusion constants at energy E for regions 1 and 2, respectively. The transient neutron flux for the two region system is derived in Appendix A, and the result is:

$$\phi^{(1)}_{tr} = \frac{2}{a+2}\left[E_2(-\Sigma_t^{(1)}x) + a\,E_3(-\Sigma_t^{(1)}x)\right] \qquad x \leq 0$$

$$\phi^{(2)}_{tr} = \frac{2}{a+2}\left[E_2(\Sigma_t^{(2)}x) + a\,E_3(\Sigma_t^{(2)}x)\right] \qquad x \geq 0 \tag{5.13}$$

when a is a slowly varying function of energy, so that it can be considered as a constant within each energy band ΔEg. By substituting Equation (5.13) into Equation (5.12) we get:

$$\psi^{I}(E) = \frac{1}{2}(\psi^{\infty}(E) + \psi^{hom}(E)) \tag{5.14}$$

It can be noticed that the ψ^{I} value is independent of the value of a.

$$\therefore\ \psi^{(1)}(E,x) = \psi^{hom}(E) + \frac{1}{2}(\psi^{\infty}(E) - \psi^{hom}(E))\Phi^{(1)}_{tr} \tag{5.15}$$

Inserting the values of $\psi^{\infty}(E)$ and $\psi^{hom}(E)$ gives:

$$\psi^{(1)}(E,x) = \frac{1}{E}\,\frac{\sigma_o + \lambda\sigma_{pr} + \frac{1}{2}(\sigma_{ar} + \lambda\sigma_{rr})\phi^{(1)}_{tr}}{\sigma_o + \sigma_{ar} + \lambda\sigma_{sr}} \tag{5.16}$$

$$\sigma_{rr} = \sigma_{sr} - \sigma_{pr}$$

If we define an equivalent background cross section $\sigma_o^{(1)}$ in region 1 we have

$$\psi^{(1)}(E,x) = \frac{\sigma_o^{(1)} + \lambda\sigma_{pr}}{\sigma_o^{(1)} + \sigma_{ar} + \lambda\sigma_{sr}} \frac{1}{E} \tag{5.17}$$

which is the same as for $\psi^{hom}(E,x)$, but with σ_o replaced by $\sigma_o^{(1)}$. By equating Equations (5.16) and (5.17), $\sigma_o^{(1)}$ is found:

$$\sigma_o^{(1)} = \frac{\sigma_o + \frac{1}{2}(\sigma_{ar} + \lambda\sigma_{rr})\phi_{tr}^{(1)}}{1 - \frac{1}{2}\phi_{tr}^{(1)}} \tag{5.18}$$

Using the same procedure, an "equivalent background" cross section $\sigma_o^{(2)}$ for region 2 is found:

$$\sigma_o^{(2)} = \frac{\sigma_o + \frac{1}{2}(\sigma_{ar} + \lambda\sigma_{rr})(2 - \phi_{tr}^{(2)})}{\frac{1}{2}\phi_{tr}^{(2)}} \tag{5.19}$$

It is clear from Equations (5.18) and (5.19) that well within regions 1 and 2, where $\phi_{tr}^{(1)}$ and $\phi_{tr}^{(2)}$ go to zero, they reduce to $\sigma_o^{(1)} = \sigma_o$ and $\sigma_o^{(2)} = \infty$, as we expected. If the group values of $\sigma_o^{(1)}(E,x)$ and $\sigma_o^{(2)}(E,x)$ are desired, the group values of σ_o, σ_{sr}, σ_{ar}, and $\phi_{tr}^{(1)}$ and $\phi_{tr}^{(2)}$ should be inserted in Equation (5.18) or (5.19). For instance for $\sigma_o^{(1)}(E,x)$

$$\sigma_{og}^{(1)}(x) = \frac{\sigma_{og} + \frac{1}{2}(\sigma_{arg} + \lambda\sigma_{rrg})\phi_{trg}^{(1)}}{1 - 1/2\,\phi_{trg}^{(1)}} \tag{5.20}$$

where (refer to Equation (5.13))

$$\phi_{trg}^{(1)}(x) = \frac{2}{a_g + 2}\left[E_2(\Sigma_{tg}^{(1)}|x|) + a_g E_3(\Sigma_{tg}^{(1)}|x|)\right] \tag{5.21}$$

Therefore, if $\sigma_{xg}(\sigma_o,T)$ is the correctly self shielded cross section, then:

$$\sigma_{xg}(\sigma_o,T) \equiv \sigma_{xg}^{hom}(\sigma_o',T) \equiv f^{hom}(\sigma_o',T)\sigma_{xg}^{\infty}$$

Equation (5.18) (or (5.19)) represents the new equivalence relation for transforming the energy self shielding treatment near the interface areas into the energy self-shielding treatment of an infinite homogeneous medium.

5.4 CORRECTION OF INFINITE MEDIUM HETEROGENEOUS SELF SHIELDING NEAR THE INTERFACE

In section 5.2 it was shown that in order to correctly take into account the heterogeneous self shielding near the interface, the Dancoff factor should be modified. For this purpose first the Dancoff factor at the interface is derived and then the space-dependent Dancoff factor C(x) is derived.

5.4.1 Dancoff-Factor Correction at Interfaces

When resonance isotopes are in a lump form in a system (i.e. a lattice), then the neutrons heading toward each lump are shielded (shadowed) by the surrounding lumps. According to the definition of the Dancoff-factor, C, these neutrons are being shielded by a factor of (1 - C), and if we divide the heterogeneous system into n regions (for example, each region could be a fuel rod), and the effect of each region on the shielding is C_i, then we have $C = \sum_{i=1}^{n} C_i$ (D4, A2).

With this introduction we consider a two region system, each medium with a Dancoff factor C_i.

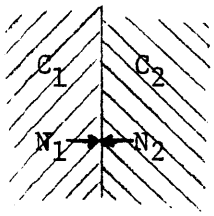

Considering a point at the interface, assume that in the absence of self shielding, N_1 and N_2 are the number of neutrons reaching the interface. The system can be obtained from the superposition of the two following systems.

$$\begin{array}{c|c} C_1 & C_2 \\ N_1 \rightarrow & \leftarrow N_2 \end{array} \quad \rightleftarrows \quad \begin{array}{c|c} C_1 & C_1 \\ \frac{N_1}{2} \rightarrow & \leftarrow \frac{N_1}{2} \end{array} + \begin{array}{c|c} C_2 & C_2 \\ \frac{N_2}{2} \rightarrow & \leftarrow \frac{N_2}{2} \end{array}$$

System 1 System 2

For system 1 the neutrons reaching the interface after shielding are $(\frac{N_1}{2} + \frac{N_1}{2})[1 - (C_1 + C_1)] = N_1(1 - 2C_1)$. For system 2 the corresponding term is $N_2(1 - 2C_2)$. Hence in the superimposed system the neutrons reaching the interface would be $N_1(1 - 2C_1) + N_2(1 - 2C_2) = N'$. By definition of C_I, the Dancoff-factor of the system at the interface we also have $N' = (N_1 + N_2)(1 - C_I)$. Therefore

$$(N_1 + N_2)(1 - C_I) = N_1(1 - 2C_1) + N_2(1 - 2C_2) \tag{5.22}$$

or

$$C_I = \frac{N_1}{N_1 + N_2}(2C_1) + \frac{N_2}{N_1 + N_2}(2C_2) = \frac{N_1 C_L}{N_1 + N_2} + \frac{N_2 C_R}{N_1 + N_2} \tag{5.23}$$

$$C_2 = 2C_1, \quad C_R = 2C_2$$

Equations (5.21) and (5.22) indicate that the Dancoff-factor at the interface is equal to the summation of two infinite half-space systems, each composed of one of the regions 1 or 2, weighted by the fraction of neutrons reaching the interface from each region in the original system. In general, considering neutrons in energy group g we have:

$$C_{Ig} = \frac{N_{1g}}{N_{1g} + N_{2g}} C_{Lg} + \frac{N_{2g}}{N_{1g} + N_{2g}} C_{Rg} \tag{5.24}$$

For the case in which $N_{1g} = N_{2g}$ we get $C_{Ig} = \frac{1}{2}(C_{Lg} + C_{Rg})$. This is the approximation used in SPHINX for treating a slab cell with different moderator materials on each side. In this relation C_{Rg} is the Dancoff-factor for a slab cell with both sides the same as the right side of the original cell (i.e. a regular, symmetric cell). This suggests that they have approached the problem by assuming that the system is the superposition of two other systems, much as we have done here. Now the question is how to find N_{1g} and N_{2g}.

Calculation of N_{1g} and N_{2g}

In problems of current interest three kinds of neutron source distributions are generally encountered: (1) a flat source; (2) an exponential source $e^{\alpha x}$; (3) a cosine source $\cos(Bx)$; x is the distance between the point of observation and the interfacial plane. We assume an isotropic distribution of neutrons in the medium. Considering the coordinate system:

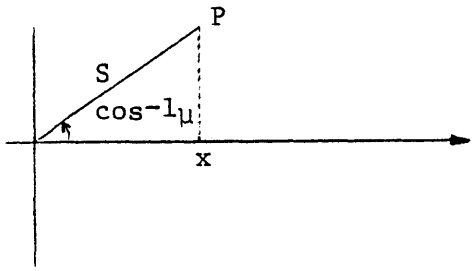

We have

$$N_g = \int_o^\infty dx\, f_g(x) \int_o^1 (\frac{1}{2}\, d\mu) e^{-\frac{s}{\lambda g}} = \frac{1}{2} \int_o^\infty f_g(x)dx \int_o^1 d\mu e^{-\frac{x}{\lambda g \mu}}$$

where

$f_g(\mu)$ = neutron source distribution in group g at point x

λg = mean free path of neutrons in group g

Setting $y = \frac{1}{\mu}$ and using the definition of the E_n functions we get:

$$N_g = \frac{1}{2} \int_o^\infty f_g(x) \int_1^\infty (-\frac{1}{y2}) e^{-\frac{x}{\lambda g} y} dy = \frac{1}{2} \int_o^\infty f_g(x) E_2(\frac{x}{\lambda g}) dx \qquad (5.25)$$

Case 1: $f_g(x) = 1$

$$N_g = \frac{\lambda_g}{4} \qquad (5.7)$$

Therefore $N_{1g} = \frac{\lambda_{1g}}{4}$ and $N_{2g} = \frac{\lambda_{2g}}{4}$

Case 2: $f_{1g}(x) = e^{\alpha_{ig} x}$ $f_{2g}(x) = e^{-\alpha_{1g} x}$

$$N_{1g} = \frac{1}{2\alpha_{1g}^2 \lambda_{ig}} [- \alpha_{1g}\lambda_{1g} + \ell n\, (1 - \alpha_{1g}\lambda_{1g})] \tilde{=} \frac{\lambda_{1g}}{4} (1 + \frac{2}{3} \alpha_{1g}\lambda_{1g})$$

$$N_{2g} = \frac{1}{2\alpha_{2g}^2 \lambda_{2g}} [+ \alpha_{2g}\lambda_{2g} - \ell n\, (1 + \alpha_{2g}\lambda_{2g})] \tilde{=} \frac{\lambda_{2g}}{4} (1 - \frac{2}{3} \alpha_{2g}\lambda_{2g}) \qquad (5.26)$$

α_{1g} and α_{2g} can be positive or negative numbers.

Case 3: $f_{1g}(x) = \cos(Bx)$, $f_{2g}(x) = \cos(Bx)$

$$N_{1g} = \frac{\lambda_{1g}}{4}\left[1 - \frac{1}{2}(B\lambda_{1g})^2\right]$$
$$N_{2g} = \frac{\lambda_{2g}}{4}\left[1 - \frac{1}{2}(B\lambda_{2g})^2\right] \qquad (5.27)$$

In Case 3 one can safely use the flat source approximation because $B = \frac{\pi}{\bar{H}} = \frac{1}{40}\ cm^{-1}$ and λ_g would be at most around 7 cm so

$$\frac{1}{2}(B\lambda)^2_{max} \tilde{-} \frac{1}{2}\left(\frac{7\pi}{40}\right)^2 = 0.15;$$

and for the resonance region $\lambda \tilde{-} 2cm \rightarrow \frac{1}{2}(B\lambda)^2 \tilde{-} 0.01 << 1$. Since at high energies where λ_g is large the self-shielding factor is close to 1.0, then no correction is necessary in any event. Any amount of correction in C would not change the self-shielding factor at these energies (for U-238 and Th-232, $f \geq 0.99$ for $g \leq 17$ in our 50 G structure).

In Case 2 one can also use the Case 1 result since $\alpha\lambda$ is small at energies within or lower than the resonance region. In the problem of present interest, that is the ITS - Reflector interface, if we make a 50 Group S8 run, we notice that the group fluxes near the interface are exponential functions. From these fluxes we find α_{1g}'s and α_{2g}'s and then calculate $\frac{N_{1g}}{N_{1g} + N_{2g}}$. We see that for energy groups $g \geq 29$, where the resonances start to become important, there is an at most 5.5% difference between the Case 2 and Case 1 results. Later we will see that an x% change in $\frac{N_{1g}}{N_{1g} + N_{2g}}$ makes a change in the f-factor not more than $\frac{x}{2}$ %. So we see that using the Case 1 approximation contributes not more

than about 2% error. Still, to improve the approximation, one may use the one-group value of Σ_a for all α_g's in the $g \geq 25$ (for $g < 25$ no correction need be contemplated). This line of attack has been pursued with the aim of simplifying the procedure for correcting the Dancoff-factor and ultimately generating corrected shielded cross sections. For an accurate solution one should in principle run a 50 group S8 version of the problem and find α_g's, as was done in the sample problem, but we have shown that one can get the answer easily without going through the complexity of these calculations.

5.4.2 Determining the Space Dependent Dancoff-factor, C(x), Near the Interface

Up to now, we have determined the Dancoff-factor at the interface (C_{Ig}) and we also have the value of the Dancoff-factor far from the interface (simply the infinite medium case) C_{og}. Now the question is how $C_g(x)$ varies between C_{Ig} and C_{og}.

Since $(1 - C)$ is proportional to the number of neutrons reaching the point in question then, $\delta(1 - C)$, that is $(1 - C_\infty) - (1 - C(x))$ should vary as the transient first flight flux of neutrons shadowed by the fuel in their way. Therefore,

$$(1 - C_{\infty g}) - (1 - C_g(x)) = [(1 - C_{\infty g}) - (1 - C_{Ig})]\Phi_{trg}(x) \qquad (5.28$$

or

$$C_g(x) = C_{\infty g} - (C_{\infty g} - C_{Ig})\Phi_{trg}(x)$$

It should be noted that $\Phi_{trg}(x)$ is normalized to 1.0 at the interface, so that at $x = 0.0$ we get $C_g(o) = C_{Ig}$.

Inserting the expressions for C_{Ig} and $\Phi_{trg}(x)$ (see Appendix A for a derivation of $\Phi_{trg}(x)$) into Equation (5.28) gives ($C_g^{(i)}(x)$ is $C_g(x)$ in region i)

$$C_g^{(i)}(x) = C_{\infty g}^{(i)}[1 - \frac{2}{a_g + 2}(E_2(\Sigma_{tg}^{(i)}x) + a_g E_3(\Sigma_{tg}^{(i)}x))]$$

$$+ \frac{2}{a_g + 2}(E_2(\Sigma_{tg}^{(i)}x) + a_g E_3(\Sigma_{tg}^{(i)}x))[\frac{N_{1g}C_{Lg} + N_{2g}C_{Rg}}{N_{1g} + N_{2g}}] \qquad (5.29)$$

Considering only the correction for heterogeneous self-shielding the equivalent "background" cross section $\sigma_{og}^{'het}$ should then be:

$$\sigma_{og}^{'het}(x) = \frac{\bar{\Sigma}_{tnfg}}{\bar{N}_g} + \frac{a(1 - C_g(x))}{1 + (a - 1)C_g(x)}\frac{\bar{\Sigma}_{tmg}}{\bar{N}_g} \qquad (5.30)$$

The overall correction to the total self-shielding (homogeneous plus heterogeneous) can be (using Equations 5.19 and 5.27) combined into the new equivalent "background" cross section $\sigma_{og}(x)$ (see results of section 5.3):

$$\sigma_{og}^{(1)}(x) = [\frac{\bar{\Sigma}_{tnfg}}{\bar{N}_g} + \frac{a(1 - C_g^{(1)}(x))}{1 + (a - 1)C_g^{(1)}(x)}\frac{\bar{\Sigma}_{tmg}}{\bar{N}_2}$$

$$+ 1/2\ (\sigma_{arg} + \lambda\sigma_{rrg})\phi_{trg}^{(1)}(x)](1 - 1/2\ \phi_{trg}^{(1)}(x))^{-1} \qquad (5.31)$$

$$\sigma_{og}^{(2)}(x) = [\frac{\bar{\Sigma}_{tnfg}}{\bar{N}_g} + \frac{a(1 - C_g^{(2)}(x))}{1 + (a - 1)C_g^{(2)}(x)}\frac{\bar{\Sigma}_{tmg}}{\bar{N}_g}$$

$$+ (\sigma_{arg} + \lambda\sigma_{rrg})(1 - 1/2\ \phi_{trg}^{(2)})](1/2\ \phi_{trg}^{(2)})^{-1}$$

It is clear that as we move away from the interface, $\sigma_{og}^{(1)}$ and $\sigma_{og}^{(2)}$ tend toward σ_o and ∞, as expected. Equation (5.22) represents the new equivalence relation. Using the new "background" cross section to enter (and interpolate within) Bondarenko factor tables provides the corrected self shielding factor, $f_g(\sigma_{og}(x), T)$, and when this is multiplied by σ_{xg}^{∞}, the corrected cross section is obtained.

5.5 CROSS SECTION GENERATION

The self-shielding corrections derived in the previous sections are here applied in two cases: the ITS-Reflector interface problem, and the thorium-uranium subassembly problem (for details refer to Section 4.5 and Ref. M2).

The calculational procedure for cross section generation is divided into four steps:

i. Transient Flux Calculation - Using the SPHINX Code, by applying the modified "background" cross section, $\sigma_o'(x)$, the proper cross sections are generated for each case. But since $\sigma_o'(x)$ is space dependent near the interface, the area in the vicinity of the interface is divided into zones, and for each zone the average value of $\sigma_o'(x)$ is calculated, and consequently for each zone a set of cross sections is generated. If $\langle\sigma_o'\rangle_{x_i x_j}$ denotes the average of σ_o' within the interval x_i and x_j (let $x_j > x_i$) then

$$\langle\sigma_o'\rangle_{x_i x_j} = \left[\frac{\Sigma_{tnf}}{N_j} + \frac{a(1 - \langle C\rangle_{x_i x_j})}{1 + (a - 1)\langle C\rangle_{x_i x_j}} \frac{\bar{\Sigma}_{tm}}{\bar{N}_j}\right.$$

$$\left. + 1/2\ (\sigma_{ar} + \lambda\sigma_{rr})\langle\phi_{tr}\rangle_{x_i x_j}\right](1 - 1/2\langle\phi_{tr}\rangle_{x_i x_j})^{-1} \qquad (5.32)$$

Since the resonant isotopes we are dealing with in these two cases are Th-232 and U-238 and the lower reaches of the resolved resonance range will be examined (where the heaviest shadowing occurs) the Wide-Resonance approximation is applied (H1) to Equation (5.32) by setting $\lambda = 0$. $\langle C\rangle_{x_i x_j}$ is a function of $\langle\phi_{tr}\rangle_{x_i x_j}$. By averaging Equation (5.4) over the (x_i, x_j) interval we get

$$\langle\phi\rangle_{trg\ x_i x_j} = \frac{2}{(2 + a_g)(x_j - x_i)\Sigma_{tg}} [E_3(\Sigma_{tg} x_i) - E_3(\Sigma_{tg} x_j)$$

$$+ a_g E_4(\Sigma_{tg} x_i) - a_g E_4(\Sigma_{tg} x_j)] \qquad (5.33)$$

The E_3 and E_4 values can be found either from tables (as was done in the present work) or approximate analytical equations may be used. As an example $E_2(x)$ is approximated as:

$$E_2(x) = 1 - \frac{1.260578\ x}{0.363948 + x} + \frac{0.260578}{2.60162 + x} \qquad (5.34)$$

Using the relation between the E_{n-1} and E_n functions, analytic approximate forms for E_3 and E_4 can be derived from $E_2(x)$. The a_g values are given in Appendix B. Σ_{tg} is the transport macroscopic cross section of the homogenized medium (in which ϕ_{tr} is being calculated) for group g (summed over all isotopes in the medium, including the resonant isotope); and the microscopic cross sections are the self-shielded LIB-IV 50-group transport cross sections for the specific lattice geometry and composition of the medium. For the ITS-Reflector case, modified cross sections were generated for the ITS medium; and for the Th-U case they were generated for both media. Four sets of modified cross sections were generated, one for each subzone in the medium. The spacing intervals for the ITS medium are as follows. (For the other case the same spacing was again used, this time on each side of the interface):

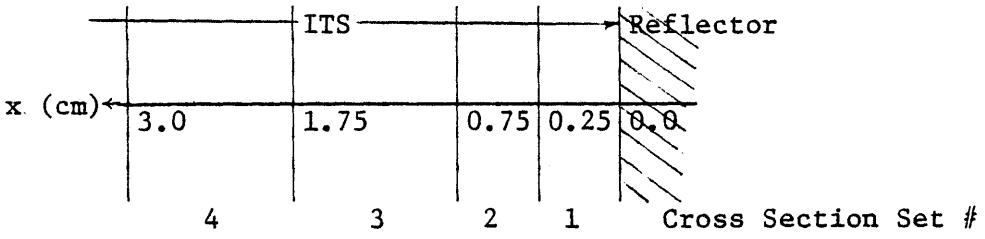

Beyond 3.0 cm, which is about 2-3 mean free paths (over the energy range involved), the $\phi_{tr}(x)$ declines to less than 0.1 (compared to $\phi_{tr}(0.0) = 1.0$). The spacing was chosen so that $\langle\phi_{tr}\rangle$ took on values of approximately 0.25, 0.45, 0.65 and 0.85 for intervals 1, 2, 3 and 4 respectively. Since for $g \leq 17$ and $g \geq 46$, the self-shielding factors for U-238 and Th-232 are ≥ 0.98 (that is, negligible self shielding is incurred), only the energy groups $18 \leq g \leq 45$ were considered in these

calculations. The calculated values of $\langle\Phi_{tr}\rangle$ for the media involved are tabulated in Appendix C.

ii. Dancoff-factor Calculation at Interface - Since for the reflector $C_R = 0$, then for the ITS-Reflector Case C_{Ig} reduces to:

$$C_{Ig}^{ITS} = \frac{N_{1g}}{N_{1g} + N_{2g}} C_{ITSg} .$$

The N_{1g} and N_{2g} were calculated using the approximate formulae $N_{1g} = \frac{\lambda_{1g}}{\lambda_{1g} + \lambda_{2g}}$ and $N_{2g} = \frac{\lambda_{2g}}{\lambda_{1g} + \lambda_{2g}}$, and are listed in App. C. The λ_{1g} and λ_{2g} are simply

$\frac{1}{\Sigma_{tg}^{(1)}}$ and $\frac{1}{\Sigma_{tg}^{(2)}}$ which were explained previously.

Table C.3 shows that C_{Ig}^{ITS} differs from C_{ITSg} by about 30%. The expression for $C(x)_{x_i x_j}$ is as follows:

$$\langle C(x)\rangle_{x_i x_j} = C_{ITSg} - (C_{ITSg} - C_{Ig})\langle\phi_{tr}^{ITS}\rangle_{x_i x_j}$$

$$\langle C(x)\rangle_{x_i x_j} = C_{ITSg}\left[1 - \left(1 - \frac{N_{1g}}{N_{1g} + N_{2g}}\right)\langle\phi_{tr}^{ITS}\rangle_{x_i x_j}\right] = A_{x_i x_j}^{ITSg} C_{ITSg} \qquad (5.34)$$

For the Th-U case, since both have similar compositions, as expected, the calculations showed that $N_{1g} \simeq N_{2g}$ or $\frac{N_{1g}}{N_{1g} + N_{2g}} \simeq \frac{N_{2g}}{N_{1g} + N_{2g}} \approx 1/2$ (see Table C.3). Also since Th and U resonances do not overlap, the U-medium is not shielded by the Th-medium, and vice versa. This means that the Dancoff-factor at the interface of the U-medium and the Th-medium (C_{Ig}^{U} and C_{Ig}^{Th}) would be 1/2 C_{Ug} and 1/2 C_{Thg}, respectively (C_{Ug} is the Dancoff factor for a U-medium of infinite extent). Thus the $\langle C(x)\rangle_{x_i x_j}$

values in the U-medium and the Th medium are as follows:

$$\langle C(x)\rangle_{x_i x_j} = C_{Ug}[1 - 1/2 \langle \phi^{U}_{tr}\rangle_{x_i x_j}] = A^{Ug}_{x_i x_j} C_{Ug} \tag{5.35}$$

$$\langle C(x)\rangle_{x_i x_j} = C_{Thg}[1 - 1/2 \langle \phi^{Th}_{tr}\rangle_{x_i x_j}] = A^{Thg}_{x_i x_j} C_{Thg} \tag{5.36}$$

The values of $A^{ITSg}_{x_i x_j}$, $A^{Ug}_{x_i x_j}$ and $A^{Thg}_{x_i x_j}$ for the four intervals of interest are listed in Table 5.1 .

iii. Homogeneous Self-Shielding Correction In Equation (5.7) the term

$$B^{g}_{x_i x_j} = 1/2\ \sigma_{arg} \langle \phi_{tr}\rangle_{x_i x_j}$$

represents the homogeneous self shielding correction. In this term, σ_{arg} is the unshielded absorption cross section of the resonant isotope. The LIB-IV 50-group cross section set was used. The $B^{g}_{x_i x_j}$ values for the ITS, for the Th-medium and the U-medium are listed in Table 5.2

To summarize, the modifications to homogeneous self-shielding and heterogeneous self-shielding are embodied in parameters $B^{g}_{x_i x_j}$ and $A^{g}_{x_i x_j}$, respectively.

iv. SPHINX Code Modifications The SPHINX Code was used to generate the corrected cross sections. For this purpose the SIGNR subroutine (which calculates σ_o) was modified so that the ISSOPT options (see Section 4.6.1 and Ref. D3) were changed so that each option would imply generating corrected cross section for one subzone. The correction factors $A^{g}_{x_i x_j}$

TABLE 5.1

VALUES OF THE $A^{ITSg}_{x_i x_j}$, $A^{Ug}_{x_i x_j}$ AND $A^{Thg}_{x_i x_j}$ PARAMETERS AT THE INTERFACE AND AVERAGED OVER THE FOUR ADJACENT ZONES

g	Interface	Zone #1 Δx = 0.25 cm	Zone #2 Δx = 0.5 cm	Zone #3 Δx = 1.0 cm	Zone #4 Δx = 1.25 cm
		$A^{ITSs}_{x_i x_j}$ (ITS-medium)			
20	0.24	0.32	0.46	0.61	0.76
25	0.63	0.69	0.77	0.87	0.93
30	0.67	0.72	0.80	0.87	0.93
35	0.72	0.75	0.83	0.89	0.94
40	0.73	0.77	0.83	0.89	0.95
42	0.73	0.77	0.83	0.90	0.95
43	0.72	0.76	0.83	0.89	0.95
45	0.70	0.75	0.82	0.90	0.95
		$A^{Ug}_{x_i x_j}$ (U-medium)			
20	0.50	0.56	0.65	0.75	0.84
25	0.50	0.58	0.70	0.83	0.91
30	0.50	0.57	0.69	0.81	0.90
35	0.50	0.56	0.69	0.81	0.90
40	0.50	0.57	0.69	0.81	0.90
42	0.50	0.57	0.69	0.82	0.90
43	0.50	0.57	0.69	0.81	0.91
45	0.50	0.58	0.70	0.83	0.92
		$A^{Thg}_{x_i x_j}$ (Th-medium)			
20	0.50	0.56	0.60	0.71	0.80
25	0.50	0.57	0.71	0.82	0.91
30	0.50	0.58	0.66	0.79	0.90
35	0.50	0.57	0.65	0.77	0.87
40	0.50	0.56	0.66	0.78	0.87
41	0.50	0.57	0.65	0.78	0.87
42	0.50	0.54	0.67	0.77	0.87
43	0.50	0.55	0.65	0.77	0.86

See Table 4.2 for group structure and Section 5.5 for definition of the A factors.

TABLE 5.2

VALUES OF THE $B^{ITSg}_{x_i x_j}$, $B^{Ug}_{x_i x_j}$ AND $B^{Thg}_{x_i x_j}$ PARAMETERS (IN-BARNS)
AT THE INTERFACE AND AVERAGED OVER THE FOUR ADJACENT ZONES

g	Interface	Zone #1 x = 0.25 cm	Zone #2 x = 0.5 cm	Zone #3 x = 1.0 cm	Zone #4 x = 1.25 cm
		$B^{ITSg}_{x_i x_j}$ (ITS-medium) or $B^{Ug}_{x_i x_j}$ (U-medium)			
20	0.25	0.23	0.17	0.13	0.08
25	0.44	0.37	0.27	0.15	0.08
30	0.90	0.77	0.56	0.35	0.18
35	1.71	1.51	1.06	0.67	0.36
40	12.82	11.15	7.95	5.00	2.56
42	42.5	36.57	26.36	15.7	8.50
43	62.5	53.73	38.74	23.74	11.87
45	131.0	111.32	78.58	44.53	20.95
		$B^{Thg}_{x_i x_j}$ (Th-medium)			
20	0.27	0.24	0.22	0.16	0.11
25	0.46	0.40	0.27	0.16	0.08
30	1.04	0.89	0.71	0.44	0.22
35	2.14	1.85	1.52	0.99	0.58
40	13.82	12.31	9.40	6.22	3.60
41	4.07	3.50	2.89	1.83	1.10
42	24.45	22.50	16.38	11.25	6.60
43	16.23	14.61	11.33	7.63	4.55

See Table 4.2 for group structure and Section 5.5 for definition of the B factors

and $B^g_{x_i x_j}$ were input to the subroutine. By this method the other normal ISSOPT options are by-passed. Therefore in the long run, if corrections of the present type are to be made routinely it is recommended that the SPHINX code be permanently altered to incorporate the appropriate ISSOPT options. In the calculation of $A^g_{x_i x_j}$ and $B^g_{x_i x_j}$ only cross sections, number densities and tables of the E_3 and E_4 functions were necessary. The SPHINX code already has access to the cross sections and number densities. Therefore a separate subroutine (incorporating tables of E_3 and E_4 functions or analytic approximations) may be written to calculate the $A^g_{x_i x_j}$ and $B^g_{x_i x_j}$ parameters, so that just by specifying the x_i and x_j values and other data which is input to a normal run of the SPHINX code, the corrected cross sections can be generated by the code.

For Dancoff-factor calculations, Sauer's approximation (S3) which was already built into the SPHINX code was employed. Since Salehi's cell treatment (S2) is more accurate, it is also recommended that his formula for Dancoff factor calculations be added to the SPHINX code as an extra option.

5.6 ANISN RESULTS

Using the cross sections generated for the zones adjacent to the interface, ANISN S8-50G simulations of the ITS-Reflector and the Th-U cases were performed. Since the ITS duct wall is carbon steel, the same material as the reflector, it is more logical to include the ITS wall adjacent to the reflector in the reflector zone, and to consider the inner plane surface of the duct wall as the interface (it should be noted that since the variation of space-dependent cross sections at

distances very close to the interface is large, it can be important where the interface location is chosen). In order to maintain symmetry, the opposite wall of the ITS was also excluded. The cross section sets that were generated for the ITS-R and Th-U cases, were arranged as in Section 5.5. Also, to maintain a closer simulation of the problem, a set of cross sections was generated for the rest of the ITS (asymptotic region) using the same geometry and composition as the ITS unit cell. In previous state-of-the-art simulations the cross sections that had been generated for a standard blanket had been used. In order to appreciate the significance of each of the corrections made on both homogeneous and heterogeneous self shielding, two ANISN runs were performed. In one run, the cross sections were corrected only for heterogeneous self shielding and in the other run both homogeneous and heterogeneous corrections were made. The results are plotted as U_c^{28} distributions in the ITS in Figure 5.2.

For comparison, a case for which no correction is made has also been plotted (curve No. 3). It is noticed that when only the heterogeneous correction is made (curve No. 2) a slight change occurs in the U_c^{28} distribution, but when both heterogeneous and homogeneous corrections are made (curve No. 1), the ANISN result reproduces the experimental results within the error involved. The U_c^{28} distribution rises at the interface by 44% and 7% in curves No. 1 and No. 2, respectively, relative to curve No. 3. In order to show how the equivalent background cross section, $\sigma_{og}(x)$, the self shielding factor, f, and the U-238 capture cross section σ_c^{28} vary near the ITS-R interface, these parameters are tabulated in Appendix C for a number of representative groups, and Table 5.3 also lists

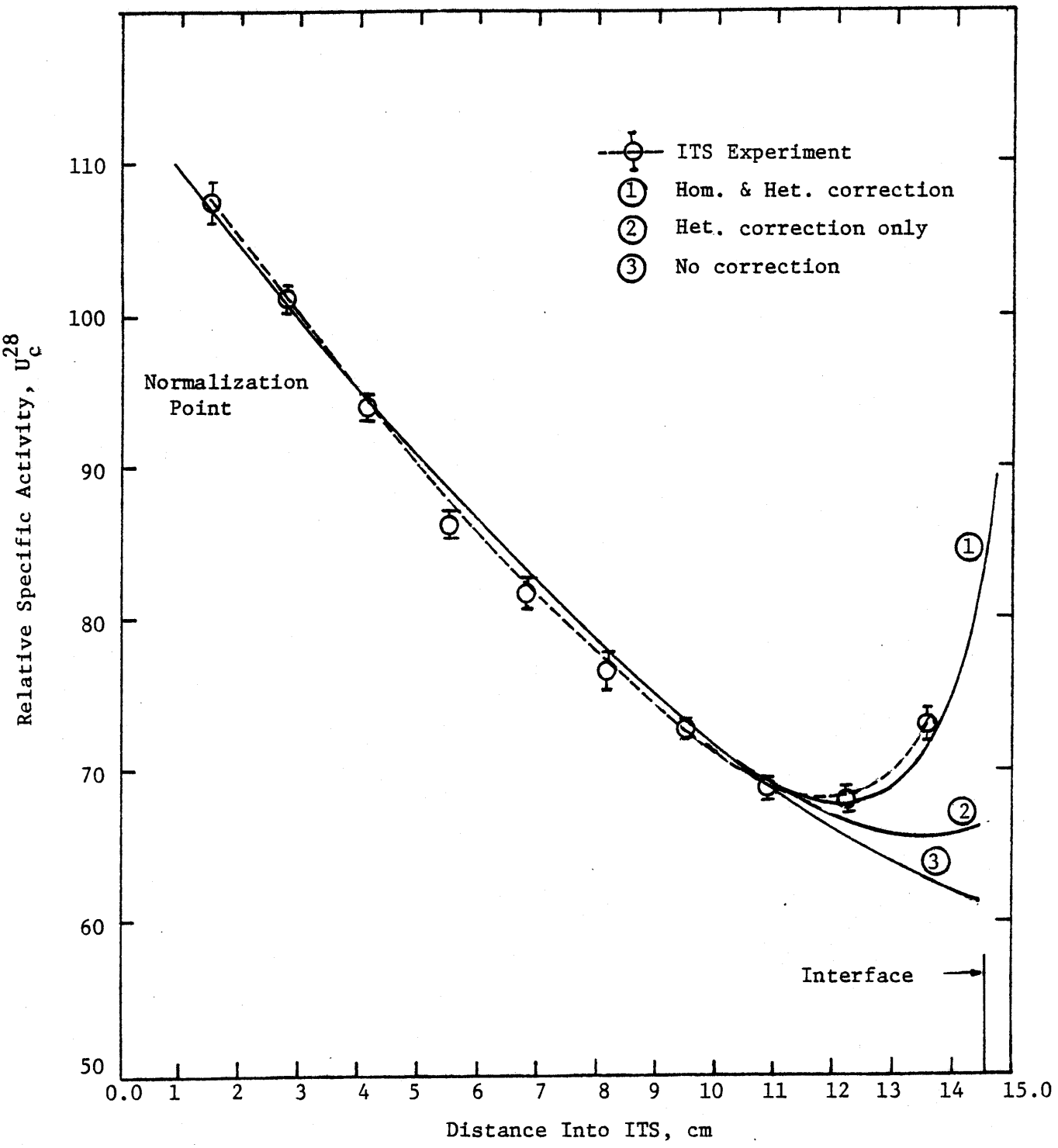

Figure 5.2 Normalized U_c^{28} Distributions in the ITS: Experimental Value and ANISN S8-50G Calculations

TABLE 5.3

VALUES OF σ_{og}^{ITS}, THE f-FACTOR AND σ_c^{28} at g = 45

AT THE ITS-R INTERFACE AND AVERAGED OVER THE

FOUR ADJACENT ZONES (ITS-SIDE)

	Zone #4 Δx = 1.25 cm	Zone #3 Δx = 1.0 cm	Zone #2 Δx = 0.5 cm	Zone #1 Δx = 0.25 cm	ITS-R Interface
only heterogeneous correction					
σ_o	31.7	33.6	35.7	39.4	45.2
f	0.0518	0.0528	0.0541	0.056	0.061
σ_c^{28}	13.57	13.83	14.17	14.66	16.00
both homogeneous and heterogeneous correction					
σ_o	57.2	94.1	164.7	262.2	344.9
f	0.0653	0.0825	0.1094	0.1391	0.1597
σ_c^{28}	17.21	21.61	28.66	36.43	41.84

g = 45 encompasses the energy range 5.04 to 8.32 ev

σ_o and σ_c^{28} are in barns

the values in g = 45, where the largest variation is found. It is seen that the values of $\sigma_{og}(x)$, f and σ_c^{28} at the interface are increased 503%. 145% and 145%, respectively, relative to the corresponding values in Zone (4). Note that the change in σ_c^{28} is about four times smaller than the change in $\sigma_{og}(x)$, and consequently errors introduced in the calculation of $\sigma_{og}(x)$ induce a quite smaller error in σ_c^{28}. This validates the point that the errors introduced due to approximations that were made in calculation of the normalized transient neutron flux induce a negligible error in σ_c^{28}. Moreover the spectrum-integrated rise in U_c^{28} (44% at the interface) is smaller than the change in σ_c^{28}. Therefore, since we are only concerned with the accuracy in U_c^{28} values, this confirms that even crude approximations in the transient neutron flux calculation are permitted. Table 5.1 shows that the parameter $A^g_{x_i x_j}$ varies slightly with g (considering mainly the resolved resonance region), and compared with the variation in the neutron mean free path with energy (see Table C.3; $N_{1g} = \lambda_{1g}/4$) the $A^g_{x_i x_j}$ variation is smaller. On the other hand, $A^g_{x_i x_j}$ is proportional to the transient neutron flux. All this suggests that one may calculate the transient neutron flux for the neutrons using an average mean free path (averaged over the resolved resonance energy range) and apply it for all energy groups. This simplifies the application of the method considerably, while still keeping the error introduced in U_c^{28} negligible.

In Figure 4.8 of Chapter 4 the normalized value of U_c^{28} determined in the (K2) experiments at the interface is "187". If we normalize curve (1) in Figure 5.2 to the same point as Figure 4.8 we get an interfacial value of U_c^{28} equal to 130. The discrepancy undoubtedly arises because the

interface in the (K2) experiment is between the blanket subassembly exterior and the reflector, while in our calculation we chose the surface between the ITS and its interior wall as an interface. The U_c^{28} value in the last 0.4 cm inside the ITS rises 13%. The distance between these two interfaces (inner wall and outer wall surfaces) is 0.4 cm,and by extrapolation U_c^{28} rises in this interval by at least 13% (because $\sigma_{og}(x)$ increases, and also the neutron flux in the energy range encompassing the resolved resonances increases more due to the proximity of scattering material), therefore the calculated value of U_c^{28} corresponding to the experimental value of U_c^{28} at the outer interface would be at least 147. Considering the experimental error and the fact that the blanket subassemblies adjacent to the reflector for these two comparative cases were not the same (the ITS in our work versus a standard blanket in Kadiroglu's) and also considering the well known difficulty in calculating the low energy tail of the neutron spectrum (which is important at the interface) noted in prior BTF work, it may be concluded that the experimental and calculational results are in good agreement. Figure 5.3 shows the results of ANISN calculations for the Th-U case. Curve No. (2) is when only the homogeneous correction is made, and curve No. (1) is when both homogeneous and heterogeneous corrections are made. The results confirm the point that correction of homogeneous self shielding is more significant than correction of heterogeneous self shielding. Curves (1) and (2) show calculated rises of 50% and 40% in U_c^{28} and 36% and 24% in U_c^{02} at the interface compared with the 70% (U_c^{28}) and 40%(Th_c^{02}) rise that the experiment shows. The 12% difference between the experimental and calculated values of U_c^{28} at the

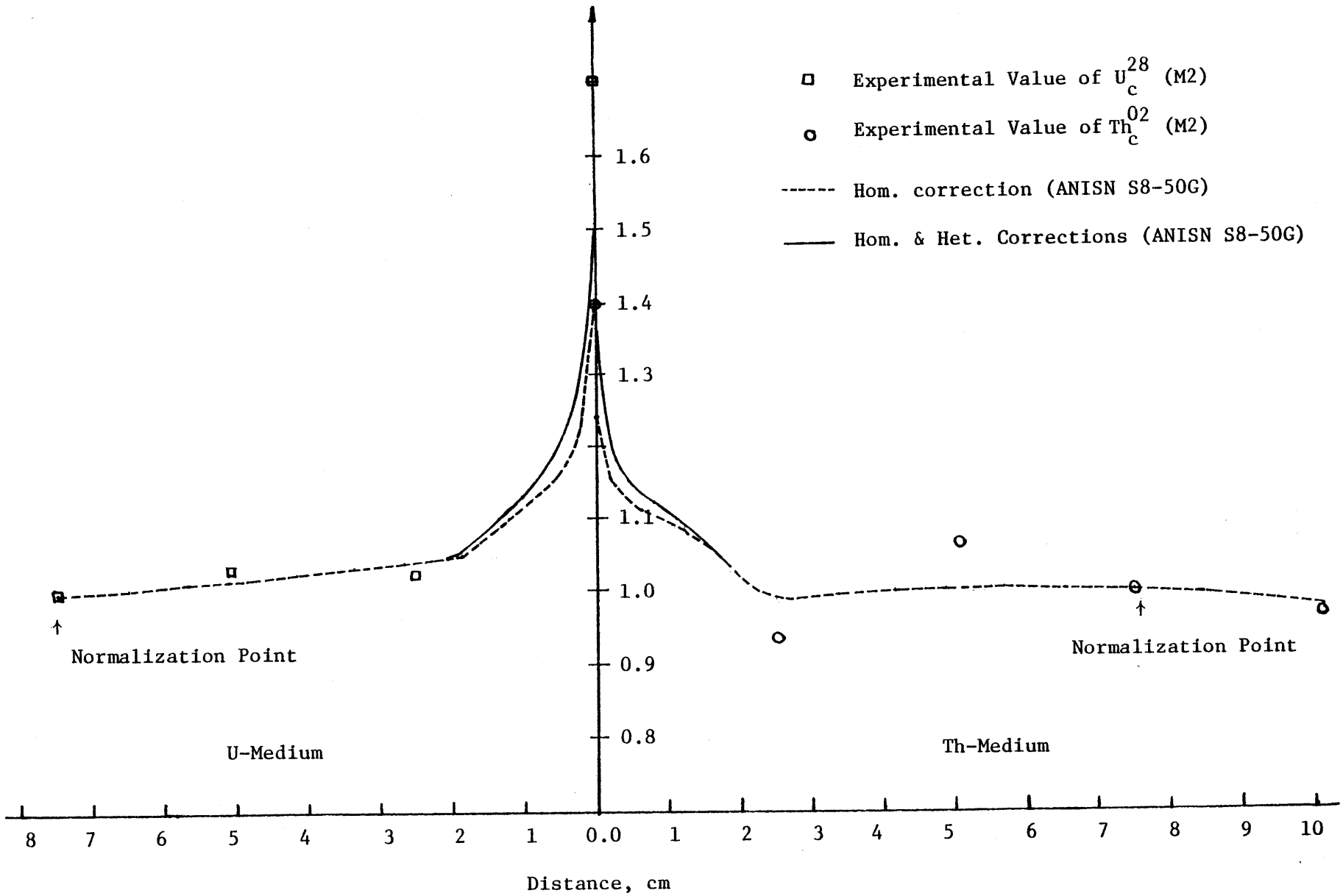

Figure 5.3 Normalized U_c^{28} and Th_c^{02} Distributions in the Th-U System: Experimental and Calculated Values

interface (1.7 and 1.5, respectively) could be due to experimental error and due to the fact that a one-dimensional simulation of the Th-U system, especially in the interface region is erroneous. The $\sigma_{og}(x)$, f, σ_c^{28}, σ_c^{02} values for both the U-medium and the Th-medium are tabulated in Appendix C. Values of these variables are listed in Tables 5.4 and 5.5. A review of Tables 5.4 and 5.5 confirms the conclusions drawn previously regarding approximating the transient neutron flux. Tables 5.4 and 5.5 also confirm the conclusion derived that the homogeneous correction is more significant than the heterogeneous correction.

In short, it is concluded that the method presented for treatment of self-shielding near an interface reproduces the experimental results within the errors involved, and the approximations made in transient neutron flux calculations induce negligible error in the resonant capture rate; similarly using a spectrum-averaged mean free path for resonance region neutrons (which simplifies the application of the method) was also concluded to be allowable.

5.7 SUMMARY

Having introduced the homogeneous and heterogeneous self-shielding factors for infinite media, a new effective, spatially variable, background cross section was derived to calculate the homogeneous and heterogeneous self shielding factors near an interface. By modifying the SPHINX code to take these modifications into account, space-dependent cross sections averaged over zones near the interfaces of the ITS-R and Th-U cases were generated. The cross section sets were used in an ANISN simulation of the two cases. The ANISN results showed good agreement considering the

TABLE 5.4

VALUES OF σ_{og}^{U}, THE f-FACTOR AND σ_c^{28} AT g = 45

AT THE Th-U INTERFACE AND AVERAGED OVER THE

FOUR ADJACENT ZONES (U-side)

	Zone #4 Δx = 1.25 cm	Zone #3 Δx = 1.0 cm	Zone #2 Δx = 0.5 cm	Zone #1 Δx = 0.25 cm	U-Th Interface
only homogeneous correction					
σ_o	43.3	76.4	139.2	226.5	299.8
f	0.0581	0.0746	0.1004	0.1289	0.1490
σ_c^{28}	15.22	19.53	26.29	33.77	39.01
both homogeneous and heterogeneous corrections					
σ_o	45.2	81.0	149.0	243.6	323.1
f	0.0591	0.0767	0.1039	0.1339	0.1547
σ_c^{28}	15.49	20.09	27.22	35.07	40.47

g = 45 encompasses the energy range 5.04 to 8.32 ev

σ_o and σ_c^{28} are in barns

TABLE 5.5

VALUES OF σ^{U}_{og}, f-FACTOR AND σ^{28}_{c} AT g = 42

AT THE Th-U INTERFACE AND AVERAGED OVER THE

FOUR ADJACENT ZONES (Th-side)

	Zone #4 Δx = 1.25 cm	Zone #3 Δx = 1.0 cm	Zone #2 Δx = 0.5 cm	Zone #1 Δx = 0.25 cm	Th-U Interface
only homogeneous corrections					
σ_o	54.5	67.2	85.5	116.7	129.9
f	0.0718	0.0819	0.0957	0.1189	0.1285
σ^{02}_{c}	3.51	4.00	4.68	5.82	6.28
both homogeneous and heterogeneous corrections					
σ_o	58.3	74.7	98.3	138.4	155.5
f	0.0749	0.0876	0.1046	0.1344	0.1457
σ^{02}_{c}	3.664	4.286	5.117	6.571	7.119

g = 42 encompasses the energy range 22.6 to 37.3 ev

σ_o and σ^{02}_{c} are in barns

experimental errors involved. It was also shown that the correction to homogeneous self shielding due to the interfacial effect is more significant than the correction to heterogeneous self shielding

CHAPTER 6

SUMMARY, CONCLUSIONS AND RECOMMENDATIONS

6.1 SUMMARY

6.1.1 Introduction

Many state-of-the-art neutronic computations for fast reactor core and blanket designs are based upon the Bondarenko or self-shielding-factor-method of cross section generation (B1, K1). This method relies upon the use of self-shielding factors developed from an infinite medium treatment of resonance absorption (and scattering). As such it is not appropriate for the treatment of cross sections near interfaces between dissimilar media, such as occur between the core and blanket or blanket and reflector.

To resolve this problem, use of appropriately weighted space-dependent broad group constants has been recommended for accurate prediction of neutron transport in the blanket region (G1, S1); but this approach has not been satisfactory near large heterogeneities. One of the main causes of discrepancy can be attributed to the mismatch in cross section energy structure due to the dissimilitude in compositions near the zone interfaces. Systematic methods for handling the mismatch remain to be worked out.

The recent interest in heterogeneous core designs, in which blanket assemblies are interspersed throughout the core, has intensified the interest in resolving this difficulty. Mixed progeny designs, in which thorium internal blankets are used in uranium-plutonium cores are particularly susceptible to interface problems of the type under examination here. Finally, fuel test facilities such as the FTR and PEC

reactors, in which a variety of assemblies of dissimilar designs and compositions must co-exist, have a special need for attention to detail in this area (R1). Accordingly it is the objective of this work to develop and evaluate the means for accounting for interfacial effects in LMFBR calculations.

Limited work has been done on the study of the interfacial effect. A review of the current literature on this area shows that the problem has been attacked either by using fine group cross section sets in the resonance region (K4, R1) or by weighting broad group cross sections by a neutron flux from the integral Boltzmann-equation for a system of two homogeneous half spaces, within a resonance. There is a need for a method that corrects for the effect of an interface on both homogeneous and heterogeneous self shielded cross sections (D1, H1) and in a systematic way that can be easily applied and readily extended.

6.1.2 Design and Construction of the Blanket Interface Test Subassembly (ITS)

To conduct experimental investigations of typical LMFBR breeding blankets, the Blanket Test Facility (see Figure 6.1) has been used at MIT (F1). The facility consists of a converter, blanket and reflector. The converter is used to convert thermal neutrons, provided by the reactor, into fast neutrons to drive the blanket mockup. Blanket neutronics are studied experimentally by measuring the reaction rates of specific foils inserted in fuel rods in blanket subassemblies. The information provided by a typical subassembly used in prior research at MIT would be one data point every 3 inches. For studying interfacial effects,

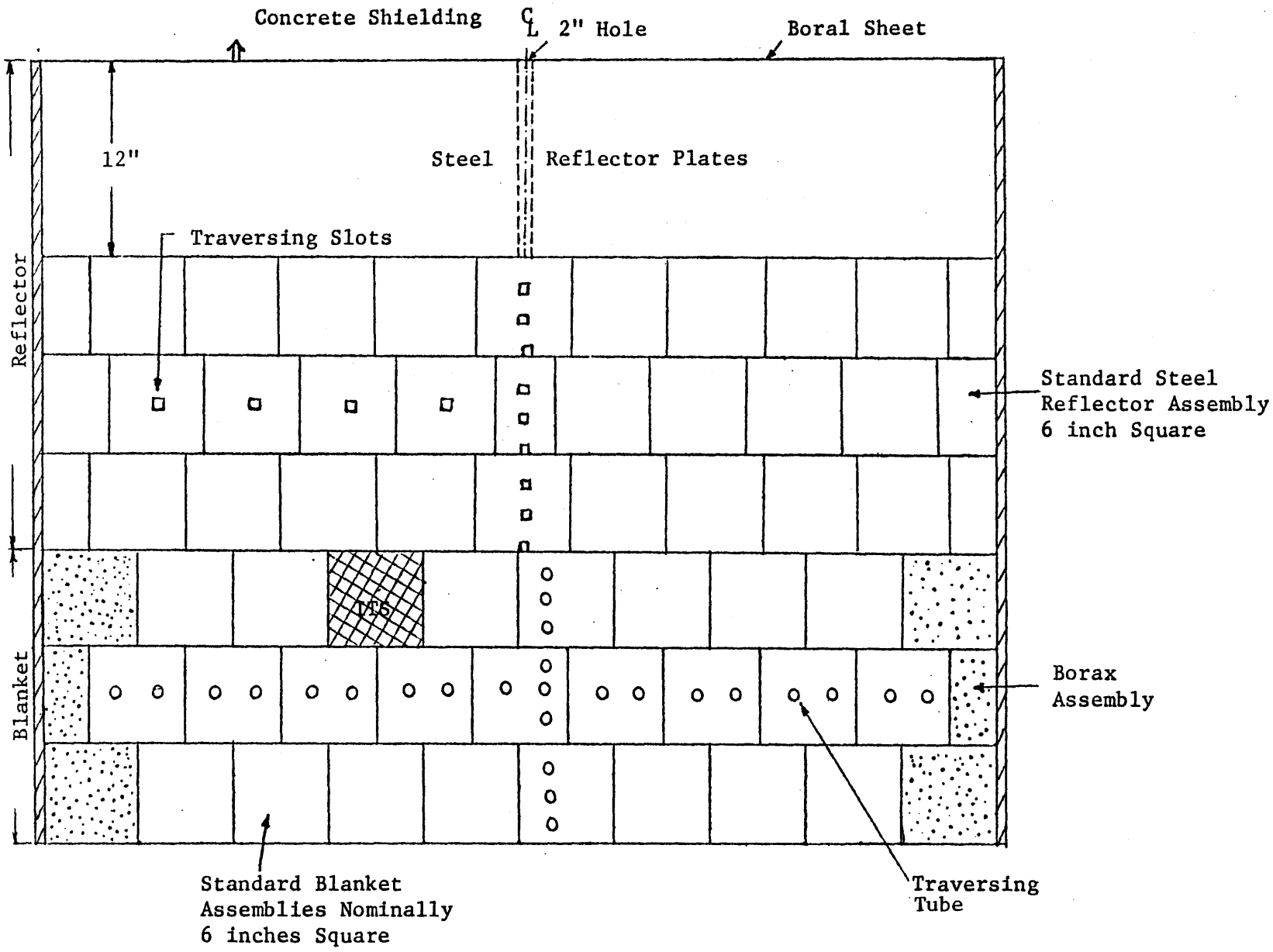

Figure 6.1 TOP VIEW OF BLANKET MOCKUP NO. 6

one needs to have more detailed information near the interface. Also, it would be useful to have a special subassembly that can provide the capability of studying interfacial effects at all of its boundaries. Therefore a decision was made to design a new blanket subassembly having the utmost capability in providing data, that is to say, any or all of its fuel rods can be transformed into experimental fuel rods. It was decided that aluminum-clad UO_2 fuel rods would be used in a hexagonal lattice, rather than the carbon-steel-clad uranium metal fuel rods used in the conventional MIT blanket mockup subassemblies. This provided greater similarity to an actual LMFBR blanket.

The design optimization was accomplished using one- and two-dimensional state-of-the-art analyses of BTF No. 6. One dimensional calculations were performed with the ANISN (A1) multigroup transport code using a 26-group self-shielded cross section set generated by self shielding the 50-group LIB-IV cross section set (K1, M1) and collapsing it into a 26-group set. Two dimensional calculations were performed with the 2DB (L1) few group diffusion theory code using a 4-group cross-section set generated by collapsing the 26-group cross-sections into 4-groups using the ANISN code. The criteria for optimization were two-fold, namely satisfaction of practical engineering constraints and provision of neutronic similitude (total neutron flux, U-238 capture rate and U-235 fission rate spatial distributions, and neutron energy spectrum at the middle of the blanket). Figure (6.2) shows the unit cell of the as-built ITS and, Figure (6.3) shows a top view. As shown, the subassembly consists of 85 removable Al-clad UO_2 fuel rods which slide into stainless steel tubes, in a hexagonal lattice having

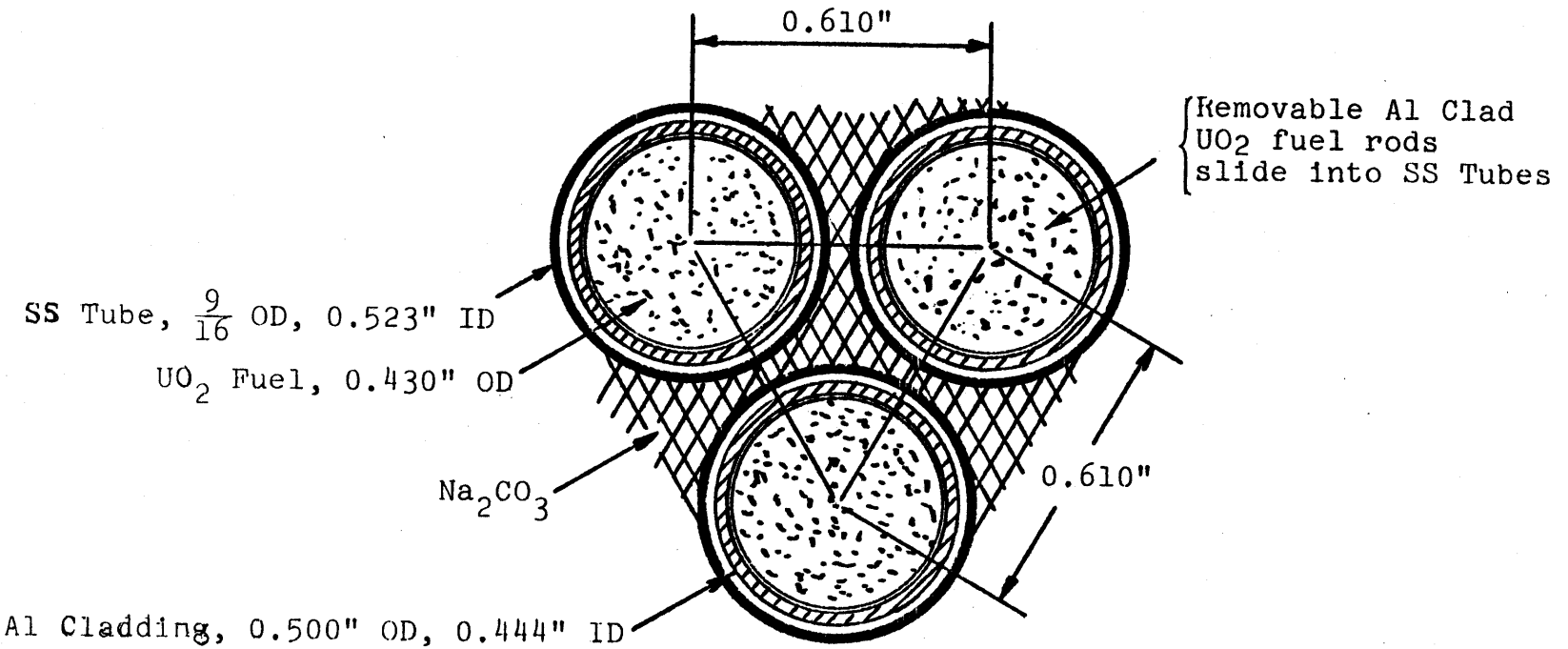

FIG. 6.2 Unit Cell of Special Interface-Traversing Subassembly

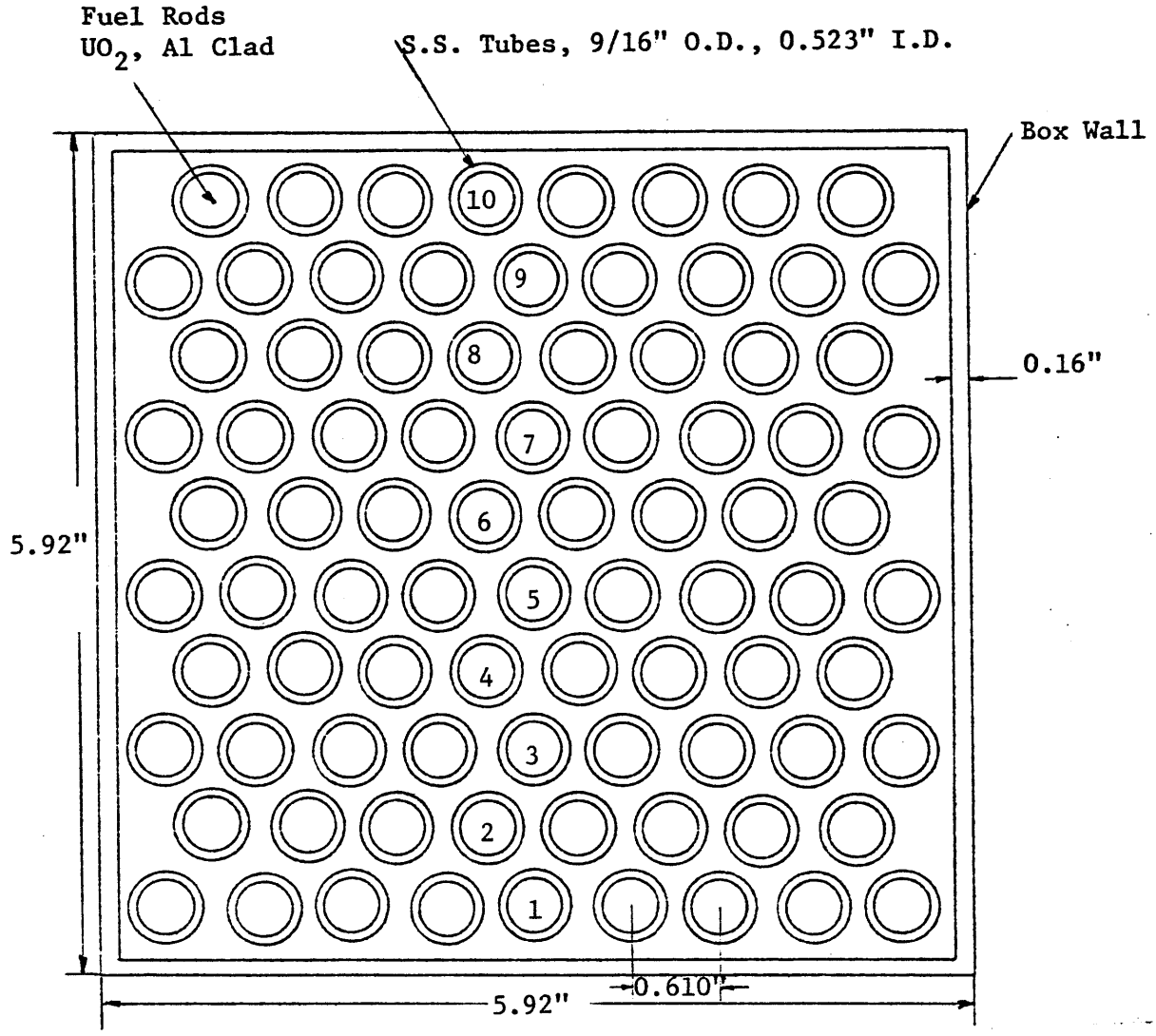

Fig. 6.3 TOP VIEW OF ITS SHOWING EXPERIMENTAL FUEL ROD POSITIONS

a 0.61 inch-pitch; the space in between the stainless steel tubes is filled with anhydrous Na_2CO_3 powder. Table (6.1) lists the atomic number densities of blanket no. 6, the as-designed ITS and the as-constructed ITS. In the ITS, the experimental fuel rods are essentially identical to the other ITS fuel rods, except that their pellets can be slid out to permit insertion of the desired foils.

6.1.3 ITS Experiments, and Analysis of the Results

To measure the Au^{198}, U_f^{25} and U_c^{28} distribution through the ITS, gold foils and uranium foils (diluted and depleted) were used (0.431 in. diameter) and for measuring the U_c^{28} distribution inside a fuel pin, "mini foils" and "ring foils" were used. The "mini foils" are small (0.056 in. diameter) foils cut out of a highly depleted uranium metal foil (18 ppm U^{25}, 0.431 in diameter). Each "ring foil" consists of six concentric segments numbered 1 through 6 from the innermost through the outermost. The position of the ITS in BTF mockup no. 6 and of the experimental fuel rods (identified by numbers 1 to 10) in the ITS during the experiments is shown in Figures (6.1) and (6.3). In Figure (6.3) the top side of the ITS faces the reflector.

Two sets of experiments were performed and the U_c^{28}, U_f^{25} and Au^{198} activity distributions along the line normal to the interface was measured. The average of the two experimental results for the U_c^{28} distribution along with ANISN S8-50G and 2DB-4G calculations (simulating the same geometric arrangement and regional composition) are plotted in Figure (6.4). The results show a buildup in U_c^{28} near the interface, a trend that was expected. In contrast with the U_c^{28} reactivity, U_f^{25} and Au^{198} activities follow the same trend as with state-of-the-art calculations

TABLE 6.1

ATOMIC NUMBER DENSITIES USED FOR ASSEMBLY INTERCOMPARISON

Isotope or Element	Atomic Number Densities (nuclei/cc)		
	Blanket No. 6 Subassembly	As-Designed ITS*	As-Constructed ITS*
U^{238}	8.872 E19	9.002 E19	9.002 E19
U^{235}	8.020 E21	7.990 E21	7.990 E22
O	1.629 E22	2.049 E22	2.258 E22
Na	8.127 E21	4.164 E21	4.238 E21
Al	-----	6.089 E21	6.898 E21
C	9.513 E19	2.108 E21	2.108 E21
Fe	1.362 E22	1.023 E22	1.406 E22
Cr	4.063 E21	1.350 E21	1.348 E21
Ni	-----	5.310 E20	5.310 E20
H	7.313 E19	-----	-----

*differences are due primarily to such factors as the inability to predict in advance the exact packing density of Na_2CO_3 powder

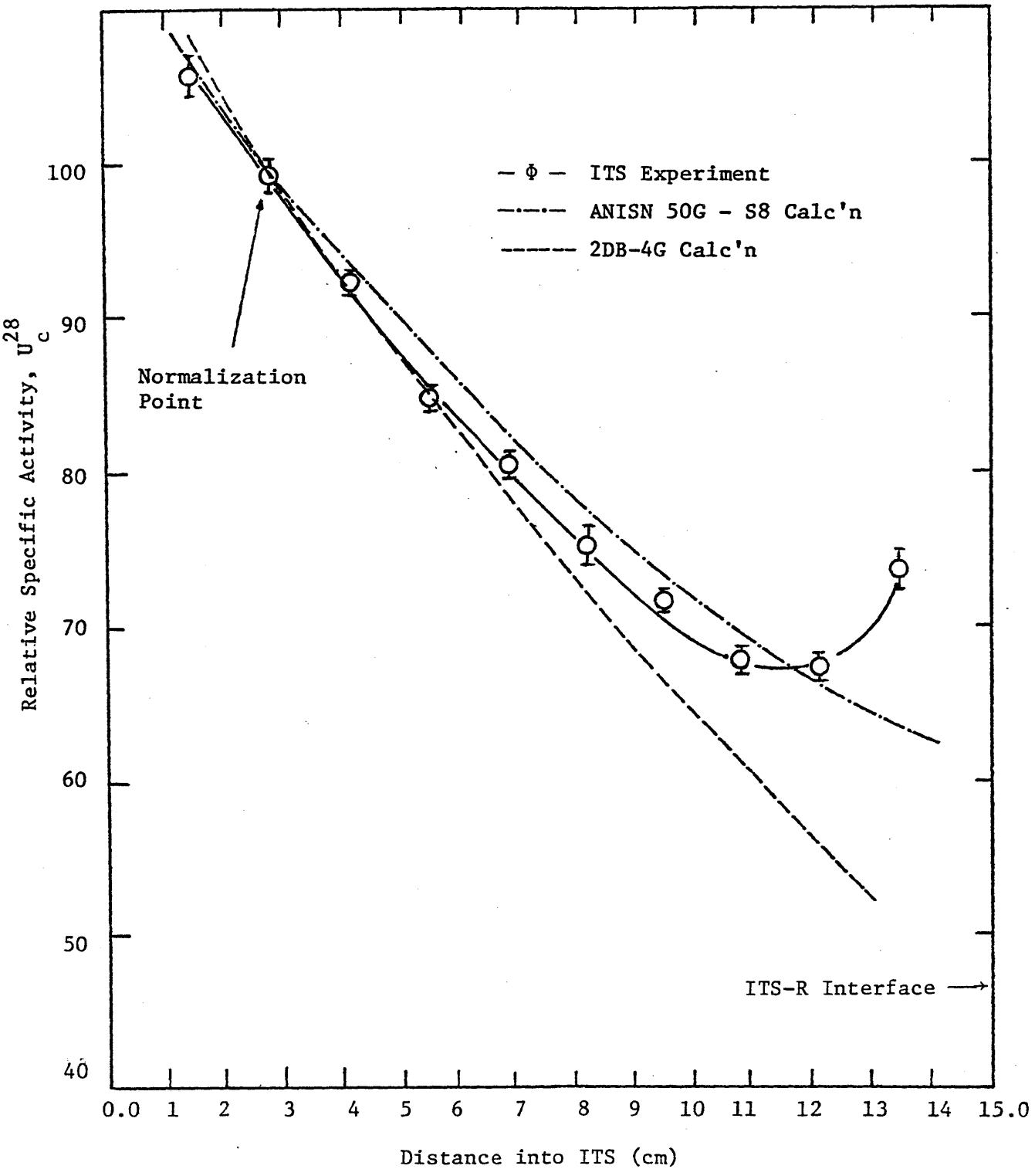

Fig. 6.4 NORMALIZED AVERAGE EXPERIMENTAL U_c^{28} TRAVERSE THROUGH THE ITS

near the interface. The buildup in U_c^{28} starts at foil #8 (4.14 cm from the interface), and U_c^{28} in foil #10 (1.46 cm from the interface) is elevated 8% relative to foil #9, however the U_c^{28} in foil #10 is elevated 16.7% relative to the extrapolated value of U_c^{28} at the same position when there is no interfacial effect. This is not as much as had been observed in previous experiments performed at MIT, and it shows that for this case, the interfacial effects do not have a significant effect on the fuel pin closest to the interface when averaged over the entire pin. The mini-foil and ring-foil U_c^{28} activities all confirm the presence of an interfacial effect, and the ring-foil results for the foil at the position closest to the interface (1.46 cm) shows that the U_c^{28} reaction rate averaged over the surface of this fuel pin is 17% higher than the average reaction rate of the U_c^{28} over the entire fuel rod. This raises the question as to whether, even though tolerable on a whole-rod basis, highly localized surface capture rates (hence plutonium production, and eventually fission) on the interface side of a pin may cause thermal/hydraulic or mechanical design problems.

The ITS experimental results were compared with state-of-the-art calculational results, and with other comparable experiments performed at MIT, to isolate the factors which are involved in the interfacial effect. It was found that the state-of-the-art calculations (using infinite medium shielding) did not show the interface effect, and changing group structure or quadrature order only shifts the curves up or down, and did not help. Examination of Leung's results (L3) showed that neither of the two limiting cross section sets, that is, unshielded and shielded, correctly predict the behavior near the interface, hence supporting the

view that an intermediate cross section set should be used near the interface, or in other words, that a space-dependent effect on self shielding should be introduced. Comparison with Kadiroglu's results (K2) showed that the interfacial effect in his assembly agreed with that measured with the ITS, and accounted for an augmentation of about 8% in the U_c^{28} rate of the blanket pin nearest the interface. This correspondence was shown to be compatible with theoretical expectations: even though the (K2) and ITS experiments had different unit cell structure and fuel slowing down sources, the effect of these factors on the self-shielding factor was studied and found to be negligible. Finally, comparison with Medeiros' results (M2) showed that the interface effect can be quite large at the boundary plane, but dies out quite rapidly with depth. Thus, pin-averaged capture rates are much less than surface foil rates.

6.1.4 Self Shielding Factor Correction Near an Interface

6.1.4.1 Homogeneous Self Shielding Factor Correction near an Interface

An adequate foundation has now been established to permit a more analytic examination of the self-shielding factor at and near an interface.

An essential step in most reactor physics calculations is the replacement of an energy-space dependent diffusion or transport equation by space-dependent few group equations. The few group method is rationalized by introducing few group constants such as the microscopic cross sections, σ_g, based on preserving reaction rates.

To procede, we begin with homogeneous systems. For an infinite medium homogeneous system the group-averaged cross sections are defined as follows:

$$\sigma_{xg} = \frac{\int_{\Delta Eg} \Phi(\underline{r},E)\sigma_x(E)dE}{\int_{\Delta Eg} \Phi(\underline{r},E)dE} \tag{6.1}$$

If we assume that $\Phi(\underline{r},E) = \Phi(\underline{r})\psi(E)$, which is valid within the medium but not valid near the interfaces of two dissimilar materials, we get:

$$\sigma_{xg} = \frac{\int_{\Delta Eg} \psi(E)\sigma_x(E)dE}{\int_{\Delta Eg} \psi(E)dE} \tag{6.2}$$

For the infinite dilution case, the neutron energy spectrum, $\psi^{\infty}(E)$, is (to good and often used approximations) $\frac{1}{E}$ for the epithermal energy range, maxwellian for thermal energies and a fission spectrum for the fast energy range. But if there is an appreciable resonant isotope concentration in the system, the neutron flux is depressed for those energies in the neighborhood of the resonance. This effect is known as "energy self shielding" or "homogeneous self-shielding". When the resonant isotopes in the medium are not infinitely dilute, the energy spectrum $\psi^{\infty}(E)$ should be replaced by $\psi^{hom}(E)$(G2):

$$\psi^{hom}(E,T,\sigma_o) = \frac{\sigma_o + \lambda\sigma_{pr}}{\sigma_{ar}(E,T) + \lambda\sigma_{sr}(E,T) + \sigma_o}\frac{1}{E} \tag{6.3}$$

where

$$\sigma_o = \frac{\sum_{i\neq j} \Sigma_{ti}}{N_j}$$

Σ_{ti} = total macroscopic cross section of non-resonant isotope i

N_j = atomic volume (≡ nuclear number) density of resonant isotope j (eg. Nuclei/barn cm)

σ_{ar}, σ_{sr}, σ_{pr} = resonant absorption, resonant scattering and potential scattering cross sections of the resonant isotope j

The energy self-shielded cross section $\sigma_{xg}(T,\sigma_o)$ and unshielded cross section σ_{xg} are related by a factor called the "self shielding factor" (B3), $f_{xg}(T,\sigma_s)$:

$$\sigma_{xg}(T,\sigma_o) = f_{xg}(T,\sigma_o)\sigma^{\infty}_{xg} \tag{6.4}$$

The assumption $\Phi(x,E) = \Phi(x)\psi(E)$ which was made in the derivation of the homogeneous self shielded cross section is not valid near interfaces. In fact the neutron energy spectrum, $\psi(E)$, would also be space dependent that is $\Phi(x,E) = \Phi(x)\psi(x,E)$. If $\psi(E,x)$ is found, the appropriate space-dependent self shielded cross section can be generated using Eq. (6.2) for regions near interfaces.

To procede, first the transient neutron flux near the interface, $\Phi_{tr}(E,x)$, was derived (using two methods: a first flight method and a kernel method). The normalized transient flux, $\phi_{tr}(E,x)$ was found to be

$$\phi_{tr}(E,x) = \frac{2}{a+2}\left[E_2(\Sigma_t x) + aE_3(\Sigma_t x)\right];\ \phi_{tr}(E,0) = 1.0 \tag{6.5}$$

where "a" is a smooth function of energy which varies between 0 (for $\Sigma_a = 0$) and $\sqrt{3}$ (for large Σ_a). It was found that setting a = 1.0 for all energies would introduce an error in $\phi_{tr}(E,x)$ of not more than 10% and the ultimate

error in the generated cross section would be negligible. Having $\phi_{tr}(E,x)$ it was found that:

$$\psi^{(1)}(E,x) = \psi^{hom}(1 - \phi_{tr}^{(1)}) + 1/2(\psi^{\infty} + \psi^{hom})\phi_{tr}^{(1)} \qquad x \leq 0$$

$$\psi^{(2)}(E,x) = \psi^{\infty}(1 - \phi_{tr}^{(2)}) + 1/2(\psi^{\infty} + \psi^{hom})\phi_{tr}^{(2)} \qquad x \geq 0 \tag{6.6}$$

where the half space No. (1) ($x \leq 0$) represents the medium containing the resonant isotope. It is clear that Eq. (6.6) for points well within the region No. (1) and No. (2) reduces to $\psi^{(1)} = \psi^{hom}$ and $\psi^{(2)} = \psi^{\infty}$, as expected. Inserting $\psi^{(1)}$ and $\psi^{(2)}$ into Eq. (6.2) gives the appropriate homogeneous self shielded cross sections. If we define an "equivalent background" cross section in region (i), $\sigma_o^{(i)}$, so that

$$\psi^{(i)}(E,x) = \frac{1}{E} \frac{\sigma_o^{(i)} + \lambda\sigma_{pr}}{\sigma_o^{(i)} + \sigma_{ar} + \lambda\sigma_{sr}}$$

the same as for $\psi^{hom}(E,x)$, but with σ_o replaced by $\sigma_o^{(i)}$, and insert $\psi^{(i)}(E,x)$ into Eq. (6.6) we get:

$$\sigma_o^{(1)} = \frac{\sigma_o + 1/2(\sigma_{ar} + \lambda\sigma_{rr})\phi_{tr}^{(1)}}{1 - 1/2\ \phi_{tr}^{(1)}} \quad ;$$

$$\sigma_o^{(2)} = \frac{\sigma_o + (\sigma_{ar} + \lambda\sigma_{rr})(1 - 1/2\ \phi_{tr}^{(2)})}{1/2\ \phi_{tr}^{(2)}} \tag{6.7}$$

It is clear that $\sigma_o^{(1)}$ and $\sigma_o^{(2)}$ tend to σ_o and infinity as we move away from the interface, as expected. Equation (6.7) represents the new equivalence relation for transforming the energy self shielding treatment near the interface areas into the energy self shielding treatment of an infinite homogeneous medium.

6.1.4.2 Heterogeneous Self Shielding Factor Correction near an Interface

So far we have been discussing the self shielding of homogeneous systems. But in essentially all reactor designs, lumped fuels are used rather than a homogeneous mixture of fuel material and moderator. This causes the resonance escape probability to increase dramatically (D1, H1), and hence the resonance absorption decreases. This self shielding, which is called "spatial" or "heterogeneous" self shielding is in many ways analogous to the energy self shielding. Both effects tend to decrease resonance absorption.

The heterogeneous self shielding is very often treated by cell homogenization through application of so-called equivalence theorems, according to which a heterogeneous system will have the same resonance integral as a homogeneous system evaluated at σ_o', where

$$\sigma_o' = \frac{\bar{\Sigma}_{tnf}}{\bar{N}_f} + \frac{a(1 - C)}{1 + (a - 1)C} \frac{\bar{\Sigma}_{tm}}{\bar{N}_j} \tag{6.8}$$

and

$\bar{\Sigma}_{tnf}$ = total macroscopic cross section of non-resonance isotopes in the fuel region, homogenized over the fuel region

$\bar{N}_j$ = homogenized atomic density of resonant isotope j over the fuel region

$\bar{\Sigma}_{tm}$ = total macroscopic cross section of isotopes in the moderator, homogenized over the moderator region

a = Levine factor (L2)

C = Dancoff-Ginsberg factor (D6)

The Dancoff factor corrects for the shadowing effects of the fuel rods surrounding the fuel rod in question. But the Dancoff factor is derived for an infinite heterogeneous medium, a premise which is not valid near interfaces. Therefore a space dependent Dancoff factor near the interface should be derived, with an asymptotic value equal to the Dancoff factor for an infinite medium.

To procede, first the Dancoff factor at the interface of two half spaces, C_I, was derived using the basic definition of the Dancoff factor (A2, D6):

$$C_I = \frac{N_1}{N_1 + N_2} C_1 + \frac{N_2}{N_1 + N_2} C_2 \tag{6.9}$$

where N_1 and N_2 are the number of neutrons reaching the interface from regions (1) and (2), and C_1 (or C_2) is the Dancoff factor of region No. 1 (or No. 2) when it is infinitely extended. The calculations showed that

$$\frac{N_1}{N_1 + N_2} \quad \text{and} \quad \frac{N_1}{N_1 + N_2}$$

can be approximated with

$$\frac{\lambda_1}{\lambda_1 + \lambda_2} \text{ and } \frac{\lambda_2}{\lambda_1 + \lambda_2}$$

where λ_1 and λ_2 are the mean free path of neutrons with energy E in regions (1) and (2). The space dependent Dancoff factor in group g, $C_g(x)$, was found to be:

$$C_g(x) = C_{\infty g} - (C_{\infty g} - C_{Ig})\phi_{trg}(x) \tag{6.10}$$

where $C_{\infty g}$ is the Dancoff factor for an infinite medium and $\phi_{trg}(x)$ is $\phi_{tr}(x)$ (Eq. (6.5)) in group g. Therefore, considering only the correction for heterogeneous self-shielding, the "equivalent background" cross section σ'^{het}_{og} should be:

$$\sigma'^{het}_{og}(x) = \frac{\bar{\Sigma}_{tnfg}}{\bar{N}_j} + \frac{a(1 - C_g(x))}{1 + (a - 1)C_g(x)} \frac{\bar{\Sigma}_{tmg}}{\bar{N}_j} \tag{6.11}$$

The overall correction to the total self-shielding (homogeneous plus heterogeneous) is combined into the new "equivalent background" cross section $\sigma_{og}(x)$:

$$\sigma^{(1)}_{og}(x) = \left[\frac{\bar{\Sigma}_{tnfg}}{\bar{N}_j} + \frac{a(1 - C^{(1)}_g(x))}{1 + (a - 1)C^{(1)}_g(x)} \frac{\bar{\Sigma}_{tmg}}{\bar{N}_j} + 1/2(\sigma_{arg} + \lambda\sigma_{rrg})\phi^{(1)}_{trg}(x)\right](1 - 1/2\ \phi^{(1)}_{trg}(x))^{-1} \tag{6.12}$$

$$\sigma^{(2)}_{og}(x) = \left[\frac{\bar{\Sigma}_{tnfg}}{\bar{N}_j} + \frac{a(1 - C^{(2)}_g(x))}{1 + (a - 1)C^{(2)}_g(x)} \frac{\bar{\Sigma}_{tmg}}{\bar{N}_j} + (\sigma_{arg} + \lambda\sigma_{rrg})(1 - 1/2\ \phi^{(2)}_{trg})\right](1/2\ \phi^{(2)}_{trg})^{-1}$$

It is clear that as we move away from the interface, $\sigma_{og}^{(1)}$ and $\sigma_{og}^{(2)}$ tend to σ_o and infinity, as expected. Using the new background cross section to enter (and interpolate within) Bondarenko factor tables (B1) provides the corrected self shielding factor, $f_g(\sigma_{og}(x),T)$, and when multiplied by σ_{xg}^{∞}, the corrected cross section, $\sigma_{xg}(x)$, is obtained.

6.1.4.3 Generation of Self Shielded Cross Sections Near an Interface and ANISN Results

The self shielding corrections derived in the previous section were applied in two cases: to the ITS Reflector interface configuration and the thorium-uranium subassembly (a normal uranium-fueled blanket subassembly with a twelve inch thorium-fueled insert). Since $\sigma_{og}(x)$ is space dependent near the interface, the area in the vicinity of the interface was divided into zones; for each zone the average value of $\sigma_{og}(x)$ was calculated, and consequently for each zone a set of cross sections was generated.

Using the cross sections generated for the zones adjacent to the interface, ANISN S8-50G simulations of the ITS Reflector and the Th-U cases were performed. To maintain a closer simulation of the ITS-R problems, a set of cross section was generated for the rest of the ITS (asymptotic region), using the same geometry and composition as the ITS unit cell. In previous state-of-the-art simulations cross sections generated for a standard blanket had been used. In order to appreciate the significance of each of the corrections made on both homogeneous and heterogeneous self shielding, two ANISN runs were performed. In one run, the cross sections were corrected only for heterogeneous self-shielding, and in the other run both homogeneous and heterogeneous corrections were made. The results are plotted as U_c^{28} distributions in the ITS in Figure 6.5.

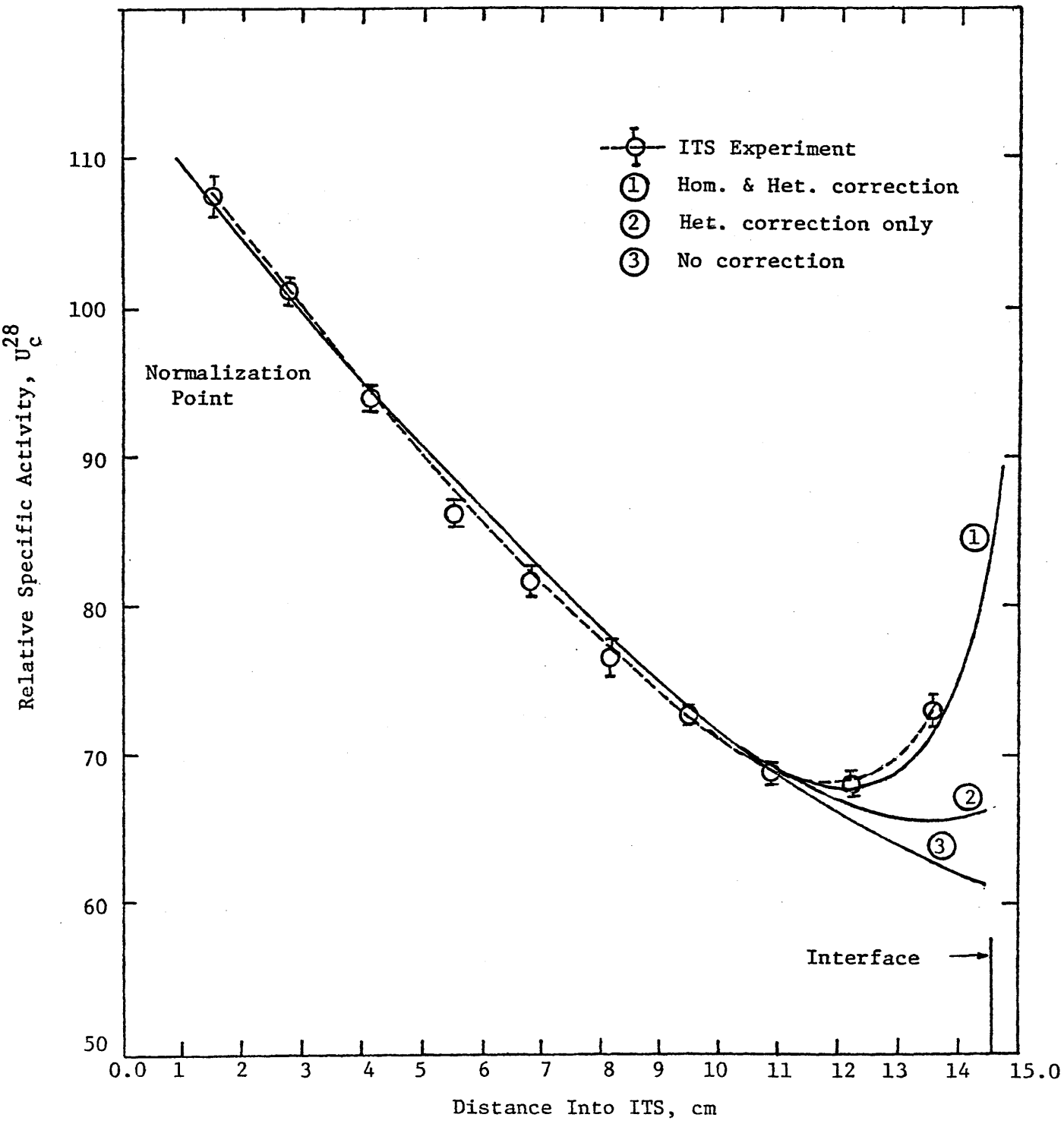

Figure 6.5 Normalized U_c^{28} Distributions in the ITS: Experimental Value and ANISN S8-50G Calculations

For comparison a case which no correction is made has also been plotted (curve No. 3). It is noticed that when only the heterogeneous correction is made (curve No. 2), a slight change occurs in the U_c^{28} distribution, but when both heterogeneous and homogeneous corrections are made (curve No. 1) the ANISN result reproduces the experimental results within the error involved. The U_c^{28} distribution rises at the interface by 44% and 7% in curves No. 1 and No. 2, respectively, relative to curve No. 3.

Figure 6.6 shows the results of ANISN calculations for the Th-U case. Curve No. 2 corresponds to when only the homogeneous correction is made, and curve No. 1 applies when both homogeneous and heterogeneous corrections are made. The results confirm the point that correction of homogeneous self shielding is more significant than correction of heterogeneous self shielding. Curves No. 1 and No. 2 show calculated overall rises of 50% in U_c^{28} and 36% in U_c^{02} at the interface, compared with the 70% (U_c^{28}) and 40% (U_c^{02}) rises that the experiment shows. The 12% difference between the experimental and calculated values of U_c^{28} at the interface can be attributed to experimental error and to the well-known difficulty in calculating the low energy tail of the neutron energy spectrum noted in prior BTF work, and also to the fact that a one-dimensional simulation of the Th-U system, especially in the interface region is not entirely adequate.

In short, it is concluded that the method presented for treatment of self shielding near an interface reproduces the experimental results adequately.

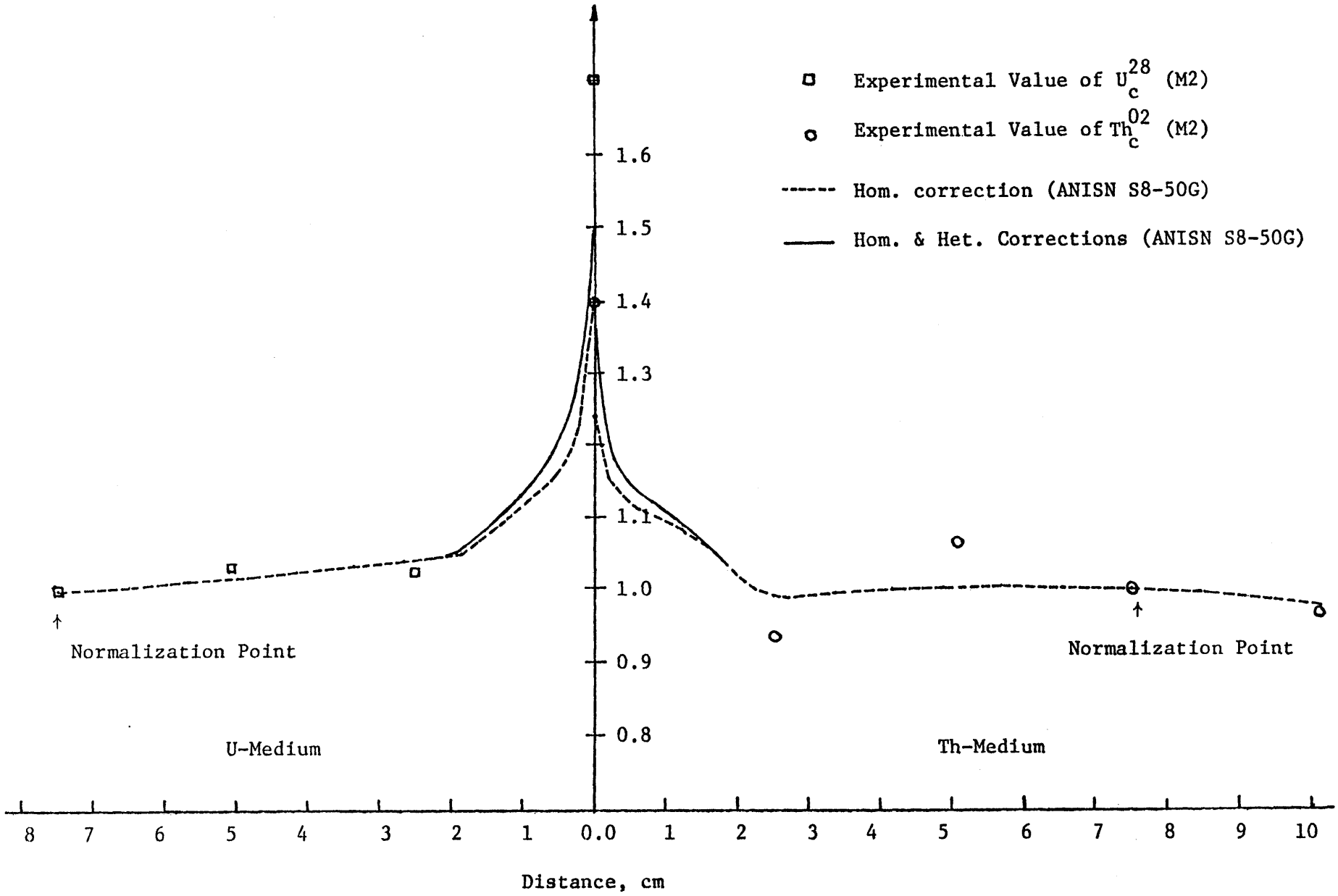

Figure 6.6 Normalized U_c^{28} and Th_c^{02} Distributions in the Th-U System: Experimental and Calculated Values

6.2 CONCLUSIONS

In brief, the work reported here supports the following observations and conclusions:

(1) An interface traversing subassembly (ITS) has been successfully designed, constructed and employed to examine perturbations in fertile capture rates immediately adjacent to interfaces between media of significantly different composition.

(2) The experimental results showed substantial (up to 50%) increases in local U-238 and Th-232 capture rates at interfaces of the type anticipated in commercial or experimental fast breeder reactor designs.

(3) Methods have been developed for generation of space dependent background cross sections, σ_o, near an interface; (modified to account for both the dominant homogeneous and less important heterogeneous effects); for their use in preparation of the corresponding space-dependent fertile capture cross sections in multigroup format; and for their use in narrow multizone calculations of capture rates near interfaces.

(4) When the method was applied to the MIT experiments, the calculated and experimental results were in good agreement (considering both experimental errors and shortcomings in other aspects of state-of-the-art calculational methods and cross section sets).

6.3 RECOMMENDATIONS

While, as a result of the work reported and referenced herein, it is felt that an adequate and straightforward method now is in place to treat interface effects in FBR environments, improvements in a number of areas are possible. On the most fundamental level, simplification can be sought: instead of modifying the background cross section, σ_o, it would be worthwhile to seek theoretically sound ways to interpolate among the region capture cross sections themselves (thereby eliminating one entire step in the correction process), or , even more optimistically, to attempt development of a way to take the results of conventional calculations and then superimpose an interface perturbation after-the-fact.

Since interface effects are highly localized it is recommended that an analysis of the thermal, hydraulic and mechanical consequences of high local fissile buildup and fission rates be carried out to determine the appropriate level of concern for this phenomenon, and to establish target accuracies for computations and measurements.

It is also recommended that a limited number of carefully-designed experiments be carried out using rod-surface foils to obtain data on interface effects which closely simulates circumstances encountered in actual reactor design situations.

More attention should be focused on accurate calculation of the low energy flux tail in FBRs because of its significance to interfacial self shielding effects.

Finally, consideration should be given to preparation of a production grade modification to codes such as SPHINX to facilitate implementation of interface corrections of the type discussed here.

APPENDIX A

DERIVATION OF TRANSIENT NEUTRON FLUX DISTRIBUTION NEAR AN INTERFACE

In this section we derive the transient neutron flux distribution for a two region system. We solve the problem with two different but closely related approaches: a first flight method and a kernel method.

First Flight Method

The solution of the transport equation consists of two terms (W1): the asymptotic flux and the transient flux

$$\Phi(x,E) = \Phi_{As}(X,E) + \Phi_{tr}(x,E) \qquad (A.1)$$

The transient flux dies out beyond a few mean free paths from the interface. The asymptotic flux is the solution of the diffusion equation for the system. In contrast to the asymptotic flux, the transient flux which is also called the single collision density, is due to the first collisions of neutrons coming directly from a source. After the first collision, these neutrons diffuse out and contribute to the asymptotic solution. Therefore having a neutron source in region R (we denote the two regions by L and R as left and right regions), produces transient flux in the L region and vice versa (for more details consult Ref. W2)

Suppose we want to derive $\phi^{L}_{tr}(x,Eg)$ in region L (neutrons with energy within energy band ΔEg). The neutron source in region R (which extends throughout the region) which contributes to ϕ^{L}_{tr} can be represented by an equivalent neutron angular distribution, $f(\mu, Eg)$, at the interface (G2). For the case of the isotropic approximation we have: $f(\mu,Eg)d\mu = d\mu$,

where $\mu = \cos \theta$ and θ is the angle between the neutron direction and the normal to the interface, and varies between 0 and $\frac{\pi}{2}$. For the nonisotropic case and when the neutron distribution is more forward (toward region L), $f(\mu, Eg)$ can be approximated by Fermi's general formula (A1):

$$f(\mu,Eg)d\mu = \frac{2}{2 + a}(1 + a\mu)d\mu \quad 0 \leq \mu \leq 1 \quad \left(\int_0^1 f(\mu,Eg)d\mu = 1\right) \qquad (A.2)$$
$$a \geq 0$$

For the case of the diffusion of thermal neutrons into a free space $a = \sqrt{3}$. Parameter a is energy-dependent, and later we will discuss its behavior further. Having the function $f(\mu,Eg)$, the transient flux, $\phi^L_{tr}(E,Eg)$, is simply derived from the following integral:

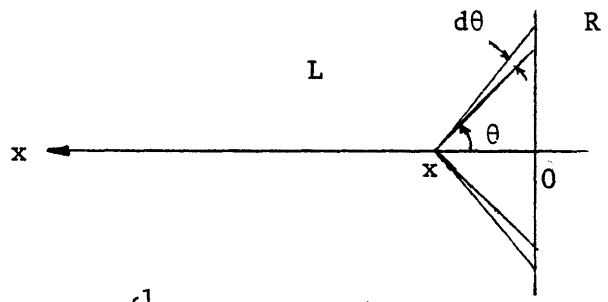

$$\phi^L_{tr}(x,Eg) = \int_0^1 A'_g f(\mu,Eg)e^{-s/\lambda g}d\mu$$

$$\phi^L_{tr}(x,Eg) = \int_0^1 Ag(1 + a_g\mu)e^{-x/\mu\lambda g}d\mu; \; A_g = \frac{2}{2 + a_g}A'_g \qquad (A.3)$$

where A'_g is the neutron source strength. By setting $y = \frac{1}{\mu}$ and introducing the definition of the exponential integral functions E_n we get:

$$\phi^L_{tr}(x,Eg) = A_g\int_1^\infty (\frac{1}{y^2} + \frac{a_g}{y^3})e^{-x/\lambda g\ y}{}_{dy}$$

or

$$\phi^L_{tr}(x,Eg) = A_g[E_2(\Sigma^L_{tg}x) + a_g E_3(\Sigma^L_{tg}x)] \tag{A.4}$$

The $\phi^R_{tr}(a,Eg)$ is the same as $\phi^L_{tr}(x,Eg)$ except that Σ^L_{tg} is replaced by Σ^R_{tg} and A_g occurs with opposite sign.

Thus for this case we have:

$$\begin{aligned}\phi^L(x,Eg) &= \phi^L_{As}(x,Eg) + A_g[E_2(-\Sigma_{tg}x) + a_g E_e(-\Sigma^L_{tg}x)] \quad x \le 0\\ \phi^R(x,Eg) &= \phi^R_{As}(x,Eg) - A_g[E_2(\Sigma^R_{tg}x) + a_g E_3(\Sigma^R_{tg}x)] \quad x \ge 0\end{aligned} \tag{A.5}$$

The Kernel Method

In a paper published by Forbes et. al., the monoenergetic transport equation for a two region system has been solved using the kernel method (F3). The procedure can be easily extended to the fine group multigroup case. The result is:

$$\begin{aligned}\phi^L(x,Eg) &= \phi^L_{As}(x,Eg) + B_g[E_2(-\Sigma^L_{tg}x)] + C_g[E_3(-\Sigma^L_{tg}x)] \quad x \le 0\\ \phi^R(x,Eg) &= \phi^R_{As}(x,Eg) - B_g[E_2(\Sigma^R_{tg}x)] - C_g[E_3(\Sigma^R_{tg}x)] \quad x \ge 0\end{aligned} \tag{A.6}$$

where

$$B_g = 1/2\ (C_{Rg} - C_{Lg})\phi_{As}(0) + 1/2\ [\frac{S_{Rg}(0)}{\Sigma^R_{tg}} - \frac{S_{Lg}(0)}{\Sigma^L_{tg}}] \tag{A.7}$$

$$C_g = 1/2(C_{Lg} - C_{Rg})J_{As}(0) + 1/2\ [\frac{S'_{Lg}(0)}{(\Sigma^L_{tg})^2} - \frac{S'_{Rg}(0)}{(\Sigma^R_{tg})^2}] \tag{A.8}$$

C_{ig} = number of secondaries per collision in group g in region: $\frac{\Sigma^i_{gg}}{\Sigma^i_{tg}}$

$S_{ig}(x)$ = neutron source distribution in group g in region i

$$S'_{ig}(x) = \frac{d}{dx} S_{ig}(x)$$

Notice that both Equations (A.1) and (A.2) have the same form. In order to be able to calculate constants Bg and Cg, one requires the functions $S_{Rg}(x)$ and $S_{Lg}(x)$. Even with approximations tedious calculations are involved. However, for present purposes only the normalized transient flux is needed, therefore only the ratio Cg/Bg is required. Also we notice that since the $E_2(x)$ and $E_3(x)$ functions behave similarly, the normalized function $\phi_{tr}(z) = \frac{2}{a+2} (E_2(z) + aE_3(z))$ is not sensitive to the value of a. Hence we don't need a highly precise calculation of the a_g (or Bg/Cg), parameters and, indeed, a crude approximation for a_g will suffice.

Calculation of Parameter a_g

For the case of an isotropic neutron distribution the value of a is zero, and for diffusion of thermal neutrons (from region R) into free space (region L) "a" is $\sqrt{3}$. Physical intuition suggests that these two limiting values of "a", 0 and$\sqrt{3}$, would correspond to Σ^L_a (Σ_a in region L) equal to 0 and ∞, respectively. In order to evaluate the sensitivity of a_g to the macroscopic cross section of the absorber medium, Σ^L_a, and to check whether, for the absorbing media that we are involved with (ITS-reflector and U-Th system) a_g stays within this range (0 and $\sqrt{3}$), a one group

ANISN simulation was performed for a two region system. Three cases were considered, with Σ_s in region R taken to be the macroscopic unshielded scattering cross section of the reflector in g = 45 for all three cases, and Σ_a in the L region was set equal to 1/2 Σ'_a, Σ'_a and $2\Sigma'_a$ (Σ'_a is the macroscopic unshielded absorption cross section of the ITS in g = 45, the group in which Σ'_a is maximum). We then have:

	Case 1	Case 2	Case 3
Σ_a^L	1.086	2.132	4.223
Σ_t^L	1.526	2.572	4.663
Σ_s^R	0.893	0.893	0.893
Σ_t^R	0.966	0.966	0.966

It was found that $f(\mu)$ fits the equation $f(\mu) = (1 + 0.8\mu)$ fairly well for all three cases. Therefore a_g would be within the range 0 and $\sqrt{3}$ and also its variation as Σ'_a changes (or equivalently changing group energy) is small. Thus for all groups a single value for the "a" parameter can be used. To confirm this conclusion, $\phi_{tr}(z) = \frac{2}{2 + a} (E_2(z) + aE_3(z))$ was calculated in the range $0.0 \leq z \leq 1.5$ for a = 0.0, a = 0.5, a = 1 and a = $\sqrt{3}$. It was found that the maximum difference in $\phi_{tr}(z)$ relative to the case a = 1.0 in this range (beyond z = 1.5, $\phi_{tr}(z)$ would be very small) was 10% (see Table A.1). As the numerical results in Chapter 5 show, the error which is introduced in the

TABLE A.1

NORMALIZED TRANSIENT FLUX VARIATION WITH PARAMETER "a"

x	a = 0.0	a = 0.5	a = 1.0	a = $\sqrt{3}$
0.0	1.00	1.00	1.00	1.00
0.1	0.72	0.74	0.76	0.77
0.3	0.47	0.50	0.51	0.53
0.5	0.33	0.35	0.37	0.38
0.7	0.24	0.25	0.27	0.28
0.9	0.17	0.19	0.20	0.21
1.1	0.13	0.14	0.15	0.16
1.3	0.10	0.11	0.11	0.12
1.5	0.07	0.08	0.09	0.09

self-shielding factor calculations due to an error in the a_g evaluation is much less. Based on all the considerations mentioned, a_g was set equal to 1.0 for all groups for both systems (ITS-reflector and Th-U systems).

APPENDIX B

AN IMPROVED DANCOFF FACTOR PRESCRIPTION FOR FBR APPLICATIONS

The convenience of the so-called Dancoff correction to allow for the effects of pin-to-pin shadowing on the effective cross sections for resonance absorbers has made it a well-established procedure in reactor physics calculations. While developed primarily for thermal reactor applications, its use has been carried over in an essentially unmodified form for FBR applications in cross section processing codes such as SPHINX (D3). In thermal reactors essentially all of the neutron slowing down source is concentrated in the moderator region of the unit cell; in fast reactors, on the other hand, an appreciable fraction of the slowing down can take place in the fuel. This reduces the self-shielding of resonant fuel isotopes, a phenomenon which can be allowed for by modifying the Dancoff factor.

The effective group absorption cross section for a resonance absorber in the fuel of a 2-region unit cell can be written in the form:

$$\sigma_a^{het} = \frac{\int_{\Delta E} \frac{\left[\lambda\Sigma_{pf} + \kappa\Sigma_{sfn} + \mu\Sigma_m\right]}{\left[\Sigma_{af}(E) + \lambda\Sigma_{rf}(E) + \kappa\Sigma_{sfn} + \mu\Sigma_m R(E)\right]} \sigma_{af}(E)\frac{dE}{E}}{\int_{\Delta E} \frac{\left[\lambda\Sigma_{pf} + \kappa\Sigma_{sfn} + \mu\Sigma_m\right]\left[V_f/V_c + (V_m/V_c)R(E)\right]}{\left[\Sigma_{af}(E) + \lambda\Sigma_{rf}(E) + \kappa\Sigma_{sfn} + \mu\Sigma_m R(E)\right]} \frac{dE}{E}} \qquad (B.1)$$

where

λ, κ, μ are the intermediate resonance parameters (1, 1, 1) for the narrow resonance approximation, and(0, 1, 1) for the wide resonance approximation -- calculated for each resonance using, for example, the prescriptions in Ref. S2.

Σ - volume-homogenized macroscopic cross section

pf - potential scattering by resonance absorber

rf - resonance scattering by resonance absorber

af - absorption by resonance absorber

sfn - scattering by non-resonance material in fuel

m - scattering by moderator (clad + coolant)

R(E) - ratio of mean flux in moderator region to that in fuel region

The key to practical exploitation of this approach is, of course, development of a simple prescription for R(E). We have generalized previous results reported by Kadiroglu and Salehi for this purpose (K2, S2), through which it is possible to calculate R(E) as an explicit function of the parameters defined above plus the fraction of the slowing-down source originating in each region, and the mean Dirac chord for each region ($\ell = 4V/S$).

The functional form of the relation for R(E) was developed using collision probability theory and the numerical accuracy has been verified using S_N and Monte Carlo calculations. Linearization of the expression for R(E), by using group-averaged values for the optical thicknesses

involved ($\tau = \Sigma \cdot \ell$), permits one to cast Equation (B.1) into the form of an equivalence relationship, such that the corresponding Bondarenko f-factor for the heterogeneous cell can be expressed as the f-factor for a homogeneous cell at a modified value of the background scattering cross section, σ_o. In this linearization we take advantage of the fact that the dominant contribution to the integrals of Equation (B.1) is in the wings of the resonances, and thus a weak absorption limit can be employed. It should also be noted that linearization of R(E) appears to be a mathematically necessary and sufficient condition to permit definition of equivalence relationships.

Furthermore, examination of the expression derived in this manner for σ_o permits identification of one of the terms as the Dancoff factor, (1 - C). If there is no slowing down source, in the moderator the expression for (1 - C) takes on the form of Bell's approximation with a near-optimum value of the Levine correction factor (L2). The derivation up to this point has been documented in Ref. (S2). We can, however, generalize upon the preceding results, since R(E) and expressions derived from it are a function of the fraction of the slowing down source in the fuel region, Q_f.

Recall the conventional equivalence theorem for heterogeneous media and the corresponding Dancoff factor (with Bell's approximation).

i. Heterogeneous systems with the same "background" cross section, σ_o', have equal resonance integrals.

ii. A heterogeneous system will have the same resonance integral as a homogeneous system evaluated at σ_o', where

$$\sigma_o' = \frac{\bar{\Sigma}_{tnf}}{\bar{N}_f} + \frac{1}{1 + \frac{1}{a}\tau_{tm}} \frac{\bar{\Sigma}_{tm}}{\bar{N}_f}$$, is the modified constant "background" cross section per target nucleus f

$\bar{\Sigma}_{tnf}$ = volume-homogenized total cross section of the non-resonance elements admixed with the fuel.

$\bar{\Sigma}_{tm}$ = volume-homogenized total cross section of the nuclides in the moderator/coolant region

$\bar{N}_f$ = volume-homogenized number density of the resonance absorber nuclei

a = is the Levine correction factor (L2)

τ_{tm} = total optical thickness of the moderator

The Dancoff factor in Bell's approximation is

$$1 - C = \frac{\tau_{tm}}{1 + \frac{1}{a}\tau_{tm}} \tag{B.2}$$

The improved equivalence theorem derived by Salehi (S2) for an infinite medium of heterogeneous unit cells can be written (but retaining the Q_f dependence):

$$\sigma_o' = \frac{\bar{\Sigma}_{tnf}}{\bar{N}_j} + \frac{1}{1 + \alpha_f \beta\rho\delta_m Q_C + \alpha_m \beta\rho\delta_m Q_f} \frac{\bar{\Sigma}_{tm}}{\bar{N}_j} \tag{B.3}$$

where

$$\alpha_m = \frac{1/3\left[1 + \frac{\omega\delta_m^n}{1 + \omega\delta_m^n}\right] + \omega\delta_f^{n'}}{1 + \omega\delta_f^{n'}}$$

$$\beta = 1 + \omega'[(1 - \lambda)\tau_{sf} + (1 - \nu)\tau_{snf}]; \quad \rho = 1 + \omega'(1 - \bar{\mu})\tau_{sm}$$

$$\alpha_f = \alpha_m\left(\begin{smallmatrix} f \to m \\ m \to f \end{smallmatrix}\right)$$

$$Q_C = 1 - Q_f; \quad Q_f = \frac{\xi_f \tau_f}{\xi_f \tau_f + \xi_m \tau_m}$$

and

δ_{rf} = removal optical thickness of the resonance material in the fuel

τ_{sf} = scattering (elastic) optical thickness of the resonance material in the fuel

τ_{tnf} = total optical thickness of the non-resonance material in the fuel

τ_{tm} = total optical thickness of the moderator

n, n', ω, ω' are constants which depend on unit cell structure. For a cylindrical unit cell we have n = 1, n' = 1/2, ω = 0.24; ω' = 0.06; and λ, ν, $\bar{\mu}$ are constants which are 1 for the Narrow Resonance (NR) approximation, and 0 for the Wide Resonance (WR) approximation . By analogy to Equations (B.1) and (B.2) we conclude from Equation (B.3) that

$$1 - C' = \frac{\delta_m}{1 + \alpha_f \beta \rho \delta_m Q_C + \alpha_m \beta \rho \delta_m Q_f} \tag{B.4}$$

or

$$\frac{1}{1 - C'} = \frac{1}{1 - C} + (\alpha_m - \alpha_f)\beta \rho Q_f; \quad 1 - C = \left(\frac{1 + \alpha_f \beta \rho \delta_m}{\delta_m}\right)^{-1}$$

where C is the Dancoff factor for the case when $Q_f = 0$

$$(1 - C') = [1 + (1 - C)(\alpha_m - \alpha_f)\beta \rho Q_f]^{-1}(1 - C) \tag{B.5}$$

Assuming that the resonance material of interest occurs only in the fuel region, and noting that in typical cases $\omega'\tau_{sf} << 1$, we get $\beta \tilde{=} 1, \rho = 1, \delta_m = \tau_m, \delta_f = \tau_{tnf} + \delta_{rf}$

$$(1 - C') = [1 + (1 - C)(\alpha_n - \alpha_f)Q_f]^{-1}(1 - C) \tag{B.6}$$

For a cylindrical unit cell, the value of $(\alpha_m - \alpha_f)$ for two limiting cases, namely the NR and WR cases is:

$$\alpha_{NR} = (\alpha_m - \alpha_f)_{WR} = \frac{a_m + 0.24\sqrt{\tau_{tnf} + \tau_{tf}}}{1 + 0.24\sqrt{\tau_{tnf} + \tau_{tf}}} - \frac{b_m + 0.24\sqrt{\tau_{fm}}}{1 + 0.24\sqrt{\tau_{tm}}} \tag{B.7}$$

$$\alpha_{WR} = \frac{a_m + 0.24\sqrt{\tau_{tnf} + \tau_{af}}}{1 + 0.24\sqrt{\tau_{tnf} + \tau_{af}}} - \frac{c_m + 0.24\sqrt{\tau_{tm}}}{1 + 0.24\sqrt{\tau_{tm}}} \tag{B.8}$$

where

$$a_m = 1/3[1 + \frac{0.24\ \tau_{tm}}{1 + 0.24\ \tau_{tm}}]\ ;\ b_m = 1/3[1 + \frac{0.24(\tau_{tnf} + \tau_{tf})}{1 + 0.24(\tau_{tnf} + \tau_{tf})}],$$

$$c_m = 1/3[1 + \frac{0.24(\tau_{tnf} + \tau_{af})}{1 + 0.24(\tau_{tnf} + \tau_{af})}]$$

τ_{tf} = total optical thickness of the resonance material in the fuel

τ_{af} = absorption optical thickness of the resonance material in the fuel

As a sample example, C and C' are calculated for the ITS unit cell and the results are listed in Table B.1. The results show that C and C' are almost equal in each energy group, and the maximum difference is only 0.4% in group 45. This was to be expected. If we look at Equation B.5 we note that in the term $(1 - C)(\alpha_n - \alpha_f)Q_f$, all factors are smaller than 1.0, and so the product would be a much smaller number than unity. Also note that α_m and α_f are close in value and $(\alpha_m - \alpha_f)$ is a maximum for the two limiting cases, NR and WR. Therefore for this sample problem the discrepancy bewteen C and C' evaluated using the IR approximation would be even smaller. The conclusion is that the dependence of C on Q_f is so weak, that one can simply calculate C using the thermal reactor convention: $Q_f = 0$.

TABLE B.1

IMPROVED DANCOFF FACTOR AND RELATED PARAMETERS

FOR SOME REPRESENTATIVE ENERGY GROUPS

Group Number g	Q_f	α_m^{NR}	α_f^{NR}	α_m^{WR}	α_f^{WR}	C_{NR}	C'_{NR}	C_{WR}	C'_{WR}
21	0.213	0.402	0.420	0.373	0.406	0.840	0.840	0.840	0.840
23	0.179	0.409	0.430	0.382	0.417	0.775	0.775	0.774	0.774
25	0.153	0.418	0.446	0.388	0.432	0.673	0.673	0.671	0.671
27	0.121	0.428	0.455	0.395	0.440	0.612	0.612	0.609	0.609
29	0.109	0.436	0.462	0.401	0.447	0.568	0.568	0.565	0.565
31	0.115	0.418	0.440	0.387	0.426	0.723	0.723	0.722	0.722
33	0.201	0.421	0.443	0.390	0.428	0.720	0.720	0.718	0.718
35	0.195	0.418	0.442	0.393	0.431	0.707	0.707	0.706	0.706
37	0.204	0.427	0.447	0.397	0.433	0.699	0.699	0.698	0.698
39	0.321	0.471	0.448	0.427	0.434	0.693	0.694	0.692	0.692
41	0.179	0.420	0.469	0.393	0.449	0.677	0.676	0.675	0.674
43	0.509	0.508	0.484	0.491	0.476	0.695	0.696	0.695	0.696
45	0.703	0.536	0.497	0.531	0.494	0.696	0.699	0.695	0.697

APPENDIX C

TABLES AND SIGNRC SUBROUTINE LISTING

TABLE C.1

RELATIVE SPECIFIC ACTIVITIES OF U_c^{28} MEASURED IN ITS FUEL PINS

ring #* / set #	1	2	3	4	5	6
1	104.8	105.0	104.0	105.7	109.4	124.6
2	93.8	95.6	95.9	97.9	100.6	105.1
9	62.5	63.0	64.2	64.6	67.2	75.4
10	64.6	65.7	65.6	65.2	67.1	83.1

MINIFOILS

Minifoil #	1	2	3	4	5
U_c^{28}	104.0	100.0	100.0	100.0	109.0

See Section 3.2 and Figures 3.1, 3.2 and 3.4 for positions

Representative $\sigma = \pm 1.5\%$

TABLE C.2

RELATIVE SPECIFIC ACTIVITIES OF URANIUM AND GOLD FOILS MEASURED IN THE ITS*

Foil Position #	Distance Into ITS (cm)	U_f^{25} Expt. #1	U_f^{25} Expt. #2	U_c^{28} Expt. #1	U_c^{28} Expt. #2	Au^{198}
1	1.5	107.6	101.5	108.6	104.4	104.8
2	2.8	100.	100.	100.0	100.0	100.0
3	4.2	93.8	93.1	93.9	92.2	105.0
4	5.5	86.2	87.9	86.0	84.8	96.4
5	6.8	83.9	82.7	81.7	80.5	96.0
6	8.2	80.6	77.3	76.8	74.7	91.0
7	9.5	79.9	77.7	72.6	71.7	95.3
8	10.9	77.1	76.7	68.7	67.8	94.0
9	12.2	76.7	77.1	67.7	68.2	113.0
10	13.6	73.3	74.6	70.8	73.7	129.0

*see Section (3.2)

see Figure (3.4)

Representative $\pm \sigma$ values: for U_f^{25} $\pm$ 2%

U_c^{28} $\pm$ 1.5%

Au $\pm$ 3%

TABLE C.3

VALUES OF N_{1g} (cm) AND $\frac{N_{1g}}{N_{1g} + N_{2g}}$ PARAMETERS FOR THE ITS-REFLECTOR (ITS SIDE) AND Th-U (U-SIDE) CASES

g	$\frac{\text{ITS-R}}{N_{1g}}$	$\frac{\text{ITS-R}}{\frac{N_{1g}}{N_{1g} + N_{2g}}}$	$\frac{\text{U-Th}}{N_{1g}}$	$\frac{\text{U-Th}}{\frac{N_{1g}}{N_{1g} + N_{2g}}}$
20	1.10	0.24	1.48	0.45
25	0.63	0.63	0.64	0.47
30	0.71	0.67	0.76	0.48
35	0.72	0.72	0.85	0.48
40	0.71	0.73	0.83	0.48
41	0.64	0.71	0.85	0.45
42	0.69	0.73	0.81	0.48
43	0.33	0.72	0.84	0.47
45	0.61	0.70	0.80	0.45

TABLE C.4

VALUES OF $\langle\phi_{trg}\rangle$ AT THE INTERFACE AND OVER THE FOUR ADJACENT ZONES

g	Interface	Zone #1 $\Delta x = 0.25$	Zone #2 $\Delta x = 0.5$	Zone #3 $\Delta x = 1.0$	Zone #4 $\Delta x = 1.25$
		$\langle\phi_{trg}\rangle$ in ITS medium (or U-medium)			
20	1.0	0.89	0.71	0.51	0.32
25	1.0	0.85	0.61	0.35	0.18
30	1.0	0.86	0.62	0.39	0.20
35	1.0	0.88	0.62	0.39	0.21
40	1.0	0.87	0.62	0.39	0.20
42	1.0	0.86	0.62	0.37	0.20
43	1.0	0.86	0.62	0.38	0.19
45	1.0	0.85	0.60	0.34	0.16
		$\langle\phi_{trg}\rangle$in Th-medium			
20	1.0	0.88	0.81	0.58	0.40
25	1.0	0.87	0.59	0.36	0.18
30	1.0	0.85	0.68	0.42	0.21
35	1.0	0.86	0.71	0.46	0.27
40	1.0	0.89	0.68	0.45	0.26
41	1.0	0.86	0.71	0.45	0.27
42	1.0	0.92	0.67	0.46	0.27
43	1.0	0.90	0.70	0.47	0.28

See Table 4.2 for group structure and section 5.5 for definition of $\langle\phi_{trg}\rangle$.

Table C.5 - Values of σ_{og}^{ITS}, f-factor and σ_c^{28} at g=45 at the interface and averaged over the four adjacent zones (ITS-side)

g	Zone #4 ΔN=1.25cm	Zone #3 ΔN=1.0cm	Zone #2 ΔN=0.5cm	Zone #1 ΔN=0.25cm	ITS-R Interface
			σ_o (barns)		
20	32.8	47.7	67.9	95.1	113.7
25	35.9	42.2	56.4	73.1	89.6
30	34.2	41.4	52.8	69.7	84.1
35	34.7	41.4	52.2	71.7	82.3
40	37.8	48.1	63.8	87.7	105.7
42	44.9	60.7	9.12	132.4	166.1
43	48.4	71.5	109.1	163.3	206.3
45	57.2	94.1	164.7	262.2	344.9
			f-factor		
20	0.9534	0.9638	0.9826	0.9801	0.9826
25	0.8332	0.8556	0.8673	0.8860	0.8999
30	0.5150	0.5366	0.5650	0.5983	0.6211
35	0.3225	0.3426	0.3705	0.4098	0.4296
40	0.0843	0.0928	0.1047	0.1210	0.1327
42	0.0353	0.4000	0.0483	0.0584	0.0660
43	0.0461	0.0558	0.0697	0.0872	0.0995
45	0.0653	0.0825	0.1094	0.1391	0.1597
			σ_c^{28} (barns)		
20	0.4837	0.4890	0.4935	0.4973	0.4987
25	0.7319	0.7427	0.7618	0.7782	0.7904
30	0.9244	0.9630	1.014	1.074	1.115
35	1.105	1.174	1.269	1.404	1.472
40	2.161	2.378	2.683	3.103	3.402
42	3.003	7.399	4.106	4.968	5.611
43	5.764	6.971	8.712	10.89	12.44
45	17.12	21.61	28.66	36.43	41.84

Table C.6 - Values of σ^{U}_{og}, f-factor and σ^{28}_{c} at g=45 at the interface and averaged over the four adjacent zones (U-side)

g	Zone #4 ΔN=1.25cm	Zone #3 ΔN=1.0cm	Zone #2 ΔN=0.5cm	Zone #1 ΔN=0.25	Interface
			σ_o (barns)		
20	17.7	24.1	32.6	44.3	51.4
25	26.0	30.5	40.8	53.1	65.0
30	23.6	29.3	38.5	51.6	62.7
35	23.1	28.7	38.0	53.5	63.3
40	26.1	34.9	48.9	70.7	86.5
42	33.2	47.8	76.2	115.3	146.8
43	36.5	58.2	94.2	145.4	186.7
45	45.2	81.0	149.0	243.6	323.1
			f-factor		
20	0.9337	0.9426	0.9532	0.9618	0.9675
25	0.3083	0.8160	0.8429	0.9629	0.8776
30	0.4728	0.4955	0.5284	0.5624	0.5854
35	0.2799	0.3021	0.3327	0.3735	0.3947
40	0.0753	0.0818	0.0934	0.1096	0.1202
42	0.0317	0.0362	0.0443	0.0544	0.0617
43	0.0408	0.0503	0.0644	0.0817	0.0940
45	0.0591	0.0767	0.1039	0.1339	0.1545
			σ^{28}_{c} (barns)		
20	0.4739	0.4784	0.4837	0.4881	0.4901
25	0.7100	0.7168	0.7404	0.7579	0.7708
30	0.8486	0.8892	0.9484	1.009	1.051
35	0.9587	1.035	1.140	1.279	1.352
40	1.931	2.097	2.394	2.810	3.082
42	2.697	3.077	3.767	4.622	5.248
43	5.096	6.290	8.042	10.21	11.74
45	15.49	20.09	27.22	35.07	40.47

Table C.7 - Values of σ_{og}^{Th}, f-factor and σ_c^{02} at g=42 at the Th-U interface and averaged over the four adjacent zones (Th-side)

g	Zone #4 ΔN=1.25cm	Zone #3 ΔN=1.0cm	Zone #2 ΔN=0.5cm	Zone #1 ΔN=0.25cm	Interface
			σ_o (barns)		
20	53.5	64.1	81.3	88.5	103.4
25	58.2	66.1	80.1	104.4	119.6
30	59.9	70.2	87.4	103.1	121.0
35	51.2	61.3	78.7	93.5	110.7
40	54.4	67.5	88.6	115.6	134.2
41	52.0	61.8	81.2	96.3	114.7
42	58.3	74.7	98.3	138.4	155.5
43	56.5	70.6	93.5	121.1	139.1
			f-factor		
20	0.9733	0.9769	0.9812	0.9825	0.9849
25	0.8892	0.8972	0.9088	0.9232	0.9293
30	0.6515	0.6715	0.6986	0.7189	0.7387
35	0.3324	0.3541	0.3861	0.4091	0.4352
40	0.0570	0.0633	0.0729	0.0842	0.0914
41	0.1571	0.1719	0.1981	0.3166	0.2416
42	0.0749	0.0876	0.1046	0.1344	0.1457
43	0.1024	0.1229	0.1437	0.1699	0.1861
			σ_c^{02} (barns)		
20	0.5339	0.5359	0.5302	0.5383	0.5403
25	0.8140	0.8213	0.8319	0.8451	0.8705
30	1.363	1.404	1.461	1.504	1.545
35	1.428	1.521	1.658	1.757	1.869
40	1.577	0.1751	2.015	2.327	2.528
41	1.279	1.400	1.619	1.763	1.967
42	3.664	4.286	5.117	6.571	7.119
43	3.325	3.990	4.665	5.516	6.043

```
      SUBROUTINE SIGNRC(ISSOPT,RF,RM,RML,A ,ISIN,ISOUT,ISFM,DENIS,DENLIS SIGNRC  PGM10001
     1,N1,N2,NMAX,MNUM,IGM,SIGP,SIGT)                                   SIGNRC  PGM10002
      DIMENSION SIGT(NMAX,1),SIGP(IGM,1), DENIS(1),DENLIS(1),ISFM(1),   SIGNRC  PGM10003
     1 ISOUT(1),ISIN(1),D(3),A0(50),A1(50),A2(50),A3(50),A4(50),         SIGNRC PGM10004
     1 B0(50),B1(50),B2(50),B3(50),B4(50)                               SIGNRC PGM10005
C     THIS SUBROUTINE CALCULATES THE MICRO.NONRES.XS. FOR THE F-FACTORS SIGNRC  PGM10006
C     AVERAGED OVER SUBZONES NEAR AN INTERFACE                          SIGNRC PGM10007
C     ISSOPT=0  HOMOGENEOUS OPTION                                      SIGNRC  PGM10008
C     ISSOPT=1  XS. OVER ZONE  4  (CORRESPONDING PARAM.: A4(K),B4(K) )   SIGNRC PGM10009
C     ISSOPT=2  XS. OVER ZONE  3  (CORRESPONDING PARAM.: A3(K),B3(K) )   SIGNRC PGM10010
C     ISSOPT=3  XS. OVER ZONE  2  (CORRESPONDING PARAM.: A2(K),B2(K) )   SIGNRC PGM10011
C     ISSOPT=4  ASYMMETRIC SLAB CELL                                    SIGNRC  PGM10012
C     ISSOPT=5  ISOLATED ROD                                            SIGNRC  PGM10013
C     ISSOPT=6  XS. OVER ZONE  1  (CORRESPONDING PARAM.: A1(K),B1(K) )   SIGNRC PGM10014
C     ISSOPT=7  XS. AT INTERFACE  (CORRESPONDING PARAM.: A0(K),B0(K) )   SIGNRC PGM10015
C     FOR ISSOPT=1,2,3,6,7 OPTIONS SAUERS APPROX.IN.CYL. IS USED         SIGNRC PGM10016
      IF (ISSOPT.EQ.0) GOTO 25                                          SIGNRC  PGM10017
C     CALCULATE VOLUME FRACTIONS AND MEAN CHORD LENGTHS                 SIGNRC  PGM10018
      GOTO( 5, 5, 5, 15, 20, 5, 5),ISSOPT                                       PGM10019
    5 CONTINUE                                                                  PGM10020
      VF=RF*RF/(RM*RM)                                                          PGM10021
      VM=1.0-VF                                                         SIGNRC  PGM10022
      VR=VM/VF                                                          SIGNRC  PGM10023
      VML=0.0                                                           SIGNRC  PGM10024
      BARL=2.0*RF                                                       SIGNRC  PGM10025
      GOTO 25                                                           SIGNRC  PGM10026
   15 CONTINUE                                                                  PGM10027
      DEM=1.0/(RM+RML)                                                          PGM10028
      VF=RF*DEM*2.0                                                     SIGNRC  PGM10029
      VM=(RM-RF)*DEM                                                    SIGNRC  PGM10030
      VML=(RML-RF)*DEM                                                  SIGNRC  PGM10031
      VR=(RM-RF)/RF                                                     SIGNRC  PGM10032
      VRL=(RML-RF)/RF                                                   SIGNRC  PGM10033
      BARL=4.0*RF                                                       SIGNRC  PGM10034
      GOTO 25                                                           SIGNRC  PGM10035
   20 CONTINUE                                                                  PGM10036
```

```
      BARL=2.*RF                                                                    PGM10037
   25 CONTINUE                                                          SIGNRC   PGM10038
      XS=0.0                                                            SIGNRC   PGM10039
C     THE PARAMETERS A0(K,K=1,50),...,A4(K,K=1,50) AND B0(K,K=1,50),...,  SIGNRC PGM10040
C     B4(K,K=1,50) SHOULD BE ENTERED HERE                                       PGM10041
      IF (ISSOPT.EQ.4) XS=1.0                                           SIGNRC   PGM10042
C     LOOP ON ENERGY GROUPS                                             SIGNRC   PGM10043
      DO 155 IIG=1,IGM                                                  SIGNRC   PGM10044
      AG=0.                                                             SIGNRC   PGM10045
      AGL=0.                                                            SIGNRC   PGM10046
C     LOOP ON ISOTOPES                                                  SIGNRC   PGM10047
      DO 75 J=N1,N2                                                     SIGNRC   PGM10048
      I=J-N1+1                                                          SIGNRC   PGM10049
      IF (ISOUT(J).LT.0) GOTO 30                                        SIGNRC   PGM10050
C     TEST FOR INFINITE DILUTION                                        SIGNRC   PGM10051
      IF (DENIS(J).GT.0.0) GOTO 35                                      SIGNRC   PGM10052
      IF (DENLIS(J).GT.0.0.AND.ISSOPT.EQ.4) GOTO 35                     SIGNRC   PGM10053
   30 CONTINUE                                                                  PGM10054
      SIGP(IIG,I)=1.E+7                                                         PGM10055
      GOTO 75                                                           SIGNRC   PGM10056
   35 CONTINUE                                                                  PGM10057
      SIGP(IIG,I)=0.                                                            PGM10058
      IF (ISSOPT.EQ.0) GOTO 65                                          SIGNRC   PGM10059
      IF (ISSOPT.EQ.5) GOTO 65                                          SIGNRC   PGM10060
C     TEST IF ISOTOPE J IS BOTH IN FUEL AND MODERATOR                   SIGNRC   PGM10061
      D(1)=0.0                                                          SIGNRC   PGM10062
      DO 40 JJ=N1,N2                                                    SIGNRC   PGM10063
      IF (ISIN(J).NE.ISIN(JJ)) GOTO 40                                  SIGNRC   PGM10064
      IF (DENIS(JJ)*(1.-XS).EQ.0.0.AND.(DENIS(JJ)+DENLIS(JJ))*XS.EQ.0.0) SIGNRC PGM10065
     1  GOTO 40                                                          SIGNRC   PGM10066
      D(1)=D(1)+FLOAT(ISFM(JJ))                                         SIGNRC   PGM10067
   40 CONTINUE                                                          SIGNRC   PGM10068
      IF (D(1).NE.0.0) GOTO 55                                          SIGNRC   PGM10069
C     CALCULATE NON.RES.MACRO.XS FOR ISOTOPE ONLY IN FUEL               SIGNRC   PGM10070
   45 CONTINUE                                                          SIGNRC   PGM10071
      DO 50 JJ=N1,N2                                                    SIGNRC   PGM10072
```

```
      IF (ISIN(JJ).EQ.ISIN(J).OR.ISFM(JJ).EQ.1) GOTO 50                  SIGNRC  PGM10073
      SIGP(IIG,I)=SIGP(IIG,I)+DENIS(JJ)*SIGT(JJ,IIG)                     SIGNRC  PGM10074
   50 CONTINUE                                                           SIGNRC  PGM10075
      GOTO 75                                                            SIGNRC  PGM10076
C     CALCULATE TOTAL MACRO.XS FOR DANCOF CORRECTION                     SIGNRC  PGM10077
   55 CONTINUE                                                                    PGM10078
      AG=AG+DENIS(J)*SIGT(J,IIG)*FLOAT(ISFM(J))                                   PGM10079
      AGL=AGL+DENLIS(J)*SIGT(J,IIG)*FLOAT(ISFM(J ))                      SIGNRC  PGM10080
C     CALCULATE NON.RES.MACRO.XS IN MOD AND FUEL-MOD                     SIGNRC  PGM10081
      DO 60 JJ=N1,N2                                                     SIGNRC  PGM10082
      IF (ISIN(JJ).EQ.ISIN(J)) GOTO 60                                   SIGNRC  PGM10083
      V=(VM-VF)* FLOAT(ISFM(JJ)) +VF                                     SIGNRC  PGM10084
      SIGP(IIG,I)=SIGP(IIG,I)+(DENIS(JJ)*V+DENLIS(JJ)*VML)*SIGT(JJ,IIG) SIGNRC  PGM10085
   60 CONTINUE                                                           SIGNRC  PGM10086
      GOTO 75                                                            SIGNRC  PGM10087
C     CALCULATE NON.RES.MACRO.XS-HOMOG.OPTION                            SIGNRC  PGM10088
   65 CONTINUE                                                                    PGM10089
      DO 70 JJ=N1,N2                                                              PGM10090
      IF (ISIN(JJ).EQ.ISIN(J))GOTO 70                                    SIGNRC  PGM10091
      SIGP(IIG,I)=SIGP(IIG,I)+DENIS(JJ)*SIGT(JJ,IIG)                     SIGNRC  PGM10092
   70 CONTINUE                                                           SIGNRC  PGM10093
      IF (ISSOPT.EQ.0) SIGP(IIG,I)=SIGP(IIG,I)/DENIS(J)                  SIGNRC  PGM10094
   75 CONTINUE                                                           SIGNRC  PGM10095
      IF(ISSOPT.EQ.0  ) GOTO 155                                         SIGNRC  PGM10096
C     CALCULATE DANCOF CORRECTION FACTOR C FOR GROUP IIG                 SIGNRC  PGM10097
C     WITH THE CORRECTION MADE ON DANCOF FACTOR                           SIGNRC PGM10098
      GOTO  ( 80, 85, 90, 95, 100, 105, 110),ISSOPT                      SIGNRC  PGM10099
   80 CONTINUE                                                                    PGM10100
      CALL DANCOF(2,AG,BARL,VR,C)                                                 PGM10101
      C=C*A4(IIG)                                                         SIGNRC PGM10102
      GOTO 115                                                           SIGNRC  PGM10103
   85 CONTINUE                                                                    PGM10104
      CALL DANCOF(2,AG,BARL,VR,C)                                                 PGM10105
      C=C*A3(IIG)                                                         SIGNRC PGM10106
      GOTO 115                                                           SIGNRC  PGM10107
   90 CONTINUE                                                                    PGM10108
```

```
      CALL DANCOF(2,AG,BARL,VR,C)                                          PGM10109
      C=C*A2(IIG)                                                 SIGNRC   PGM10110
      GOTO 115                                                    SIGNRC   PGM10111
   95 CONTINUE                                                             PGM10112
      CALL DANCOF(3,AG,BARL,VR,C1)                                         PGM10113
      CALL DANCOF(3,AGL,BARL,VRL,C2)                              SIGNRC   PGM10114
      C=(C1+C2)*0.5                                               SIGNRC   PGM10115
      GOTO 115                                                    SIGNRC   PGM10116
  100 CONTINUE                                                             PGM10117
      C=0                                                                  PGM10118
      GOTO 115                                                    SIGNRC   PGM10119
  105 CONTINUE                                                             PGM10120
C     THE INDEX IN DANCOF SUBROUTINE REFERS TO OLD ISSOPT OPTIONS  SIGNRC   PGM10121
      CALL DANCOF(2,AG,BARL,VR,C)                                          PGM10122
      C=C*A1(IIG)                                                 SIGNRC   PGM10123
      GOTO 115                                                    SIGNRC   PGM10124
  110 CONTINUE                                                             PGM10125
      CALL DANCOF(2,AG,BARL,VR,C)                                          PGM10126
      C=C*A0(IIG)                                                 SIGNRC   PGM10127
  115 CONTINUE                                                    SIGNRC   PGM10128
      SIGH=(1.-C)*A/(BARL*(1.+(A-1.)*C))                          SIGNRC   PGM10129
  120 CONTINUE                                                             PGM10130
      DO 150 J=N1,N2                                                       PGM10131
      IF (ISOUT(J).LT.0) GO TO 150                                RQW12-75 PGM10132
      IF (DENIS(J).EQ.0.0.AND.ISSOPT.NE.4) GOTO 150               SIGNRC   PGM10133
      IF (DENLIS(J)+DENIS(J).EQ.0.0.AND.ISSOPT.EQ.4) GOTO 150     SIGNRC   PGM10134
      I=J-N1+1                                                    SIGNRC   PGM10135
      IF (ISSOPT.EQ.5) GOTO 135                                   SIGNRC   PGM10136
C     CALCULATE SMEARED NUMBER DENSITY FOR ISOTOPE J IN FUEL AND MOD.SIGNRC   PGM10137
      DO 125 K=1,3                                                SIGNRC   PGM10138
      D(K)=0.                                                              PGM10139
  125 CONTINUE                                                             PGM10140
      DO 130 JJ=N1,N2                                             SIGNRC   PGM10141
      IF (ISIN(J).NE.ISIN(JJ))GOTO 130                            SIGNRC   PGM10142
      D(1)=D(1)+FLOAT(ISFM(JJ))*DENLIS(JJ)                        SIGNRC   PGM10143
      D(2)=D(2)+FLOAT(1-ISFM(JJ))*DENIS(JJ)                       SIGNRC   PGM10144
```

```
      D(3)=D(3)+FLOAT(ISFM(JJ))*DENIS(JJ)                                SIGNRC  PGM10145
  130 CONTINUE                                                           SIGNRC  PGM10146
      IF (ISSOPT.NE.4)  D(1)=0.                                          SIGNRC  PGM10147
      DX=D(1)+D(3)                                                       SIGNRC  PGM10148
      DEN=D(1)*VML+D(2)*VF+D(3)*VM                                       SIGNRC  PGM10149
C     CALC.DANCOF CORRECTED MICRO.NONRES.XS                              SIGNRC  PGM10150
      IF (DX.NE.0.0) GOTO 141                                                    PGM10151
  135 CONTINUE                                                                   PGM10152
      SIGP(IIG,I)=SIGP(IIG,I)+SIGH                                               PGM10153
  140 CONTINUE                                                                   PGM10154
      DEN=DENIS(J)                                                               PGM10155
  141 CONTINUE                                                                   PGM10156
      SIGP(IIG,I)=SIGP(IIG,I)/DEN                                                PGM10157
C     CALCULATE THE BACKGROUD XS. WITH HOM. SELF SHIELDING CORRECTION     SIGNRC PGM10158
      GOTO(145,146,147,150,150,148,149),ISSOPT                                   PGM10159
  145 CONTINUE                                                                   PGM10160
      SIGP(IIG,I)=(B0(IIG)*(SIGP(IIG,I)+B4(IIG)))/(B0(IIG)-.5*B4(IIG))   SIGNRC PGM10161
      GOTO 150                                                                   PGM10162
  146 CONTINUE                                                                   PGM10163
      SIGP(IIG,I)=(B0(IIG)*(SIGP(IIG,I)+B3(IIG)))/(B0(IIG)-.5*B3(IIG))   SIGNRC PGM10164
      GOTO 150                                                                   PGM10165
  147 CONTINUE                                                                   PGM10166
      SIGP(IIG,I)=(B0(IIG)*(SIGP(IIG,I)+B2(IIG)))/(B0(IIG)-.5*B2(IIG))   SIGNRC PGM10167
      GOTO 150                                                                   PGM10168
  148 CONTINUE                                                                   PGM10169
      SIGP(IIG,I)=(B0(IIG)*(SIGP(IIG,I)+B1(IIG)))/(B0(IIG)-.5*B1(IIG))   SIGNRC PGM10170
      GOTO 150                                                                   PGM10171
  149 CONTINUE                                                                   PGM10172
      SIGP(IIG,I)=(B0(IIG)*(SIGP(IIG,I)+B0(IIG)))/(B0(IIG)-.5*B0(IIG))   SIGNRC PGM10173
      GOTO 150                                                                   PGM10174
  150 CONTINUE                                                           SIGNRC  PGM10175
  155 CONTINUE                                                           SIGNRC  PGM10176
      RETURN                                                             SIGNRC  PGM10177
      END                                                                SIGNRC  PGM10178
```

APPENDIX D

REFERENCES

A1 "ANISN - A One Dimensional Discrete Ordinates Transport Code", RSIG Computer Code Collection, Oak Ridge National Laboratory, CCC-82

A2 ANL-5800, Reactor Physics Constants, Argonne National Laboratory, July 1963

A3 Amaldi, E., "The Production and Slowing Down of Neutrons", in the Encyclopedia of Physics, S. Flugge, ed., Vol. XXXVIII/2, Springer, Berlin, 1959

B1 Bondarenko, I. I., (Ed.), Group Constants for Nuclear Reactor Calculations, Consultants Bureau, New York (1964)

B2 Bell, G. I., "A Simple Treatment for Effective Resonance Integrals in Dense Lattices", Nucl. Sci. Eng., 5:138 (1959)

C1 Carmichael, B. M., Standard Interface Files and Procedures for Reactor Physics Code, Version III, LA-5486-MS (February, 1974)

D1 Duderstadt, J. J. and L. J. Hamilton, Nuclear Reactor Analysis, John Wiley & Sons, Inc., 1976

D2 Driscoll, M. J., (Ed.), "LMFBR Blanket Physics Project Progress Report No. 2", COO-3060-9, MITNE-131, June, 1971

D3 Driscoll, M. J., et. al., "LMFBR Blanket Physics Project Progress Report No. 4", COO-2250-3, MITNE-149 (1973)

D4 Davis, M. J., et. al., "SPHINX-- A One Dimensional Diffusion and Transport Nuclear Cross-Section Processing Code", WARD-XS-3045-17, August, 1977

D5 Dresner, L., Resonance Absorption in Nuclear Reactors, Pergamon Press (1960)

D6 Dancoff, S. M. and M. Ginsberg, "Surface Resonance Absorption in a Closed Packed Lattice", CP-2157 (October, 1944).

F1 Forbes, I. A., et. al., "Design, Construction and Evaluation of a Facility for the Simulation of Fast Reactor Blankets", MITNE-110, MIT-4105-2 (February, 1970)

F2 Ferziger, J. H. and P. F. Zweifel, The Theory of Neutron Slowing Down in Nuclear Reactors, MIT Press (1966)

F3 Forbes, I. A., L. E. Beghian and V. C. Rogers, "A Simple Analytic Transient Flux Expression for Use with Asymptotic Diffusion Theory", Nuc. Sci. Eng., Vol. 51, No. 1, 78 (May, 1973)

G1 Gibbs, D. C., et. al., "Analysis of Fast-Neutron Transport in Two Regions", Trans. Am. Nucl. Soc., 17,470 (1973)

G2 Goldstein, R. and R. Cohen, "Theory of Resonance Absorptions of Neutrons", Nucl. Sci. Eng., 13, 132 (1962)

H1 Henry, A. F., Nuclear Reactor Physics, MIT Press (1975)

K1 Kidman, R. B. and R. E. MacFarlane, LIB-IV: A Library of Group Constants for Nuclear Reactor Calculations, LA-6260-MS, March, 1976

K2 Kadiroglu, O. K., "Uranium Self-Shielding in Fast Reactor Blankets", COO-2250-17, MITNE-178 (1976)

K3 Kusters, H., (ed.) "Progress in Fast Reactor Physics in the Federal Republic of Germany", EURFNR-1120, Aug. 1973: Section 3.4.4

K4 Kappler, F., "Measurement and Calculation of Neutron Spectra at a Sodium-Iron Interface", Nuclear Technology, V. 27,224 (October, 1975)

K5 Kidman, K. B., et. al., "The Shielding Factor Method of Generating Multigroup Cross-Sections for Fast Reactor Analysis", Nucl. Sci. Eng., 48,189 (1972)

L1 Little, W. W., Jr. and R. W. Hardie, "2DB User's Manual, Revision 1", BNWL-831, Rev. 1 (August, 1969)

L2 Levine, M. M., "Resonance Integral Calculations for U-238 Lattices", Nucl. Sci. Eng., 16, 271 (1963)

L3 Leung, T. C., "Neutronics of an LMFBR Blanket Mockup", COO-3060-1, MITNE-127, (January, 1972).

L4 Lamarsh, J. R., Introduction to Nuclear Engineering, Addison-Wesley Reading (1977)

M1 Macher, M. S., "Fast Reactor Blanket Benchmark Calculations", S.M. Thesis, MIT Nuclear Engineering Department, September, 1977.

M2 Medeiros, D. W., "Experimental Comparison of Thorium and Uranium Breeding Potential in a Fast Reactor Blanket", S.B. Thesis, MIT Nuclear Engineering Department, June, 1978, also see "Comparative Breeding Potential of ^{232}Th and ^{238}U in LMFBR Blankets", Trans. Am. Nucl. Soc., Vol. 30, 719 (November, 1978)

M3 Meghreblian, R.,and D. Holmes, Reactor Analysis, McGraw-Hill, New York (1960)

P1 Palmedo, P. F., (ed.), "Compilation of Fast Reactor Experiments, Volume 1" Brookhaven National Laboratory, BNL-15746 (June, 1971)

P2 Paik, N. C., et. al., "Physics Evaluation and Application Quarterly Progress Report for Period Ending July 31, 1974", WARD-XS-3045-7, (November, 1974)

R1 Rothrock, R. B.,"Calculation of Resonant Reaction Rates near Region Interfaces in the FTR", Trans. Am. Nucl. Soc., 28, 774 (June, 1978) (Full paper was provided by the author)

S1 Stacey, W. M., et. al., "A New Space-Dependent Fast-Neutron Multi-region Cross Section Preparation Capability", Trans. Am. Nucl. Soc., 15, 292 (1972)

S2 Salehi, A. A., M. J. Driscoll and O. L. Deutsch, "Resonance Region Neutronics of Unit Cells in Fast and Thermal Reactors", COO-2250-26, MITNE-200, May 1977

S3 Sauer, A., "Approximate Escape Probabilities", Nuc. Sci. Eng. 18,329 (1963)

T1 Thompson, A. M., "Activation Profiles in Reactor Fuel Elements", S.B. Thesis, MIT Physics Dept., June, 1972

W1 Weisbin, C. R., et. al., MINX: A Multigroup Interpretation of Nuclear X-Sections from ENDF/B, LA-5324-MS (1973)

W2 Weinberg, A. M. and E. P. Wigner, The Physical Theory of Neutron Chain Reactors, The University of Chicago Press, 1958